HOKKAIDO UNIVERSITY

Title	CFD assisted quantitative flow measurement of Newtonian and non-Newtonian fluid flows
Author(s)	Tiwari, Neetu
Degree Grantor	北海道大学
Degree Name	博士(工学)
Dissertation Number	甲第14232号
Issue Date	2020-09-25
DOI	https://doi.org/10.14943/doctoral.k14232
Doc URL	https://hdl.handle.net/2115/86933
Type	doctoral thesis
File Information	Tiwari_Neetu.pdf

CFD assisted quantitative flow measurement of Newtonian and Non-Newtonian fluid flows

A Thesis

Submitted by

Neetu Tiwari

For the award of degree

of

Doctor of Philosophy

In Engineering

Division of Energy and Environmental system

Hokkaido University

August 2020

Supervised by Prof. Yuichi Murai

Abstract

Distributions of velocity and pressure are important to understand the fluid flows of practical importance such as flow over bluff bodies, industrial flows and environmental flows. Velocity distribution can be measured in three dimensions by PIV (Particle image velocimetry) but direct measurement of pressure distribution is still impossible so several counter techniques have been proposed for pressure estimation from PIV in literature. These techniques allow simultaneous measurement of velocity and pressure non-intrusively, which also enables the measurement of forces on immersed structures. However, estimated pressure field often suffers from errors propagating from uncertainty of velocity measurement. Error in pressure estimation depends on spatial and temporal resolution of measurement, domain size, aspect ratio and boundary conditions. Through past efforts, pressure estimation had been well investigated for transparent Newtonian fluids. However, in industries, opaque and non-Newtonian fluids are commonly in usage and these are inseparable from our daily needs. Existing pressure estimation techniques based on PIV measurement are not valid for opaque fluids and Non-Newtonian fluids and no study is available in this area. Present study is the first attempt to introduce the pressure estimation techniques for opaque Newtonian, opaque non-Newtonian and transparent non-Newtonian fluids. A novel irrotational correction framework is also proposed to provide curl free pressure field.

In chapter 1, the background of research and basic theory are discussed followed by the objectives of this research work. In chapter 2, experimental arrangements and conditions are described. In chapter 3, a novel pressure estimation technique is discussed for opaque flows. PIV is substituted by UVP (Ultrasonic velocity profiler) for collecting velocity data due to its capability of measurement in opaque fluids. UVP can only give the velocity information in 1C-1D (one component- one dimensional) which added a new challenge of pressure estimation because 1C-1D data is insufficient to estimate pressure from Navier-Stokes or Pressure Poisson equations. Hence, a unique filtering technique is developed by combination of FFT (Fast

Fourier transform) and POD (Proper orthogonal decomposition) coupled with Taylor frozen hypothesis to determine unknown component of velocity from equation of continuity. This algorithm is demonstrated in milk flow.

In chapter 4, another pressure estimation algorithm is developed for transparent shear thinning fluids based on PIV measurements. Navier-Stokes and pressure Poisson equation cannot be used directly for pressure estimation in these flows so momentum equations modified with rheological model are used. Power law and Carreau-Yasuda models are compared. This algorithm was tested for cylinder flow in steady and unsteady cases. It was found that the shear thinning property works against the momentum diffusion. In unsteady cylinder flow, for slowly developing vortices, the present algorithm works, but for separated wake flow it is invalid. Generally, in Newtonian fluids, the pressure Poisson equation is very useful for unsteady flows but it is invalid for shear thinning fluid flow. Hence, a new pressure Poisson is derived for shear thinning fluids. However, this equation could not be utilized for pressure estimation because the spatial resolution of PIV is insufficient to solve new pressure Poisson equation which has four additional source terms consisting of viscosity and other higher order derivatives. This open problem is addressed in next chapter. Error propagation from uncertainty of velocity to pressure is analyzed by linear propagation analysis to understand the specific role of shear thinning in error propagation. It was found that the error propagation increases with error in viscosity, which indicates that the selection of rheological models and parameters are extremely important.

In chapter 5, PIV is substituted by UVP for velocity measurement which can provide a better spatial resolution of velocity data which makes it suitable for new pressure Poisson equation. This gives the advantage of its application in unsteady and opaque fluid flows so a novel pressure estimation algorithm is developed for shear thinning opaque fluids using UVP. The new pressure Poisson equation for shear thinning fluids is solved for separated wake with UVP data to obtain pressure field. The alternating pattern of low-pressure regions in wake is

successfully reconstructed which assures the good performance of algorithm. In parametric study, it was found that the Strouhal number decreases with Reynolds number increment which is opposite of Newtonian fluids.

In chapter 6, an irrotational correction method based on Helmholtz decomposition theorem is proposed for curl correction in estimated pressure gradient from velocity data. It utilizes the curl correction characteristic of Laplacian operator. It is applicable in pressure fields estimated from Navier-Stokes and pressure Poisson equation. Present method is tested in analytical field and experimental data of PIV. If Navier-Stokes is employed for pressure gradient estimation, present method can provide the error free pressure field without performing integration and saves the computational cost a lot. It also eliminates the necessity of velocity filtering techniques which often filter the information of true flow data.

In chapter 7, conclusions of this work and future directions are discussed.

Keywords: Particle image velocimetry, Ultrasonic velocity profiler, pressure estimation, flow over cylinder, non-Newtonian fluids, pressure curl correction

Thesis Supervisor: Yuichi Murai

Title: Professor

Acknowledgements

List of Abbreviations

PIV	Particle Image Velocimetry
UVP	Ultrasonic Velocity Profiler
2D	Two Dimensional
3D	Three Dimensional
2C	Two Components
POD	Proper Orthogonal Decomposition
FFT	Fast Fourier Transform
CMC	Carboxy Methyl cellulose

Nomenclature

f_D	Doppler shift frequency
f_0	Basic frequency of ultrasound
c	Speed of sound
t	Time
U	Free stream velocity/ towing speed
ρ	Density of water
μ	Viscosity
μ_0	Zero shear viscosity
η	Non-dimensional viscosity
u, v	Non-dimensional x and y component of velocity
U_s	Mean convection velocity of flow structure
X, Y	Dimensional space coordinates
x, y	Non-dimensional space coordinates
V	Dimensional y component of velocity
Cp	Coefficient of pressure
ω	Vorticity
Re	Reynolds number
p	Non-dimensional pressure
P	Dimensional pressure
Q	Q value
D	Diameter of cylinder
l	Length of towing tank

W	Width of towing tank
H	Height of towing tank
τ	Stress
γ	Strain rate
k	Consistency index
n	Power law index
μ_p	Power law viscosity
II_{2D}	Second invariant of strain rate
Re_p	Reynolds number for Power law model
Cc	Correlation coefficient
A, B	Arbitrary variables
N	Number of observations
ζ_a	Mean deviation corresponding to variable A
ζ_b	Mean deviation corresponding to variable B
σ_a	Standard deviation of variable A
σ_b	Standard deviation of variable B
ε	Precision error
u_{ex}	Exact velocity
μ_m	Mathematical expectation
σ_v	Variance
α	Random error component
P_{sol}	Solenoidal component of pressure
F	Scalar potential

List of content

List of Figures

List of Tables

Chapter 1

Introduction

1.1 Background

The understanding of fluid flow and its interaction with solid structures are important due to their practical application in designing machines, optimizing the industrial process and understanding various natural processes. For example: designing high speed trains, bridges and aircrafts, ocean risers and mooring lines which are at risk of failure due to fluctuating forces while bringing oil in platform from seabed and industrial production, maintenance and transportation. The impact of natural disaster such as typhoon, storms and Tsunami can be predicted through understanding of fluid flows. The information of primitive flow variables e.g. velocity, pressure and temperature along with their distributions and fluid properties like viscosity (distribution) in case of non-Newtonian fluids is crucial to understanding of fluid flows. Present thesis offers new hybrid experimental techniques to provide a complete understanding of primitive fluid flow variable in opaque fluids and Non-Newtonian fluids which has not yet been measured in detail. These techniques will have wide applications ranging from food engineering, marine engineering and safety engineering to environmental engineering.

Fluid flows are usually studied either by experimental techniques or computational fluid dynamics. In experimental technique, the quantitative information of fluid flows is obtained by measurement of velocity or pressure either at a point, along a line or in a plane. Hot wire anemometers, acoustic doppler velocimetry are limited to point measurement of velocity. Flow visualization techniques such as PIV (Particle image velocimetry) allows non-intrusive measurement of velocity (Willert and Gharib 1991) (Adrian 1991) (Adrian 2005). With continuous improvement of PIV in last few decades, velocity measurements have improved a lot. A dual PIV system (Liu and Katz 2006) can be employed for two-dimensional measurement

whereas multiple PIV systems can be combined for three-dimensional velocity measurements (Elsinga et al. 2006). PIV can provide the velocity information in 2D and even in 3D by Tomo-PIV.

Pressure measurement can be done using piezoelectric transducers or microphones which can measure pressure at a point. Pitot tube is intrusive in nature and is limited to give mean pressure information due to its poor time resolution. Microscopic air bubble as static pressure sensor was used in some studies but their applicability is limited to some flows and it cannot provide pressure field simultaneous to velocity. Pressure sensitive paints (PSP) can provide 2D pressure information at a solid surface over which fluid flows but can-not be applied to fluid volume. Instantaneous static pressure field is known to be most difficult to measure and none of these techniques appears to be suitable for direct measurement of pressure distribution. On the other hand, CFD (Computational fluid dynamics) method allows us to get the complete information of these variable in 2D or 3D, nevertheless, it is based on modeling a natural phenomenon and needs to be validated with comparative experiments. In CFD method, flow governing equations are solved which follows mass and momentum conservation laws. Generally, RANS (Reynolds averaged Navier-Stokes), LES (Large Eddy simulations) or DNS (Direct numerical simulations) are performed to simulate the fluid flows of practical importance. The solution of RANS and LES are affected by applied model's characteristics, on the other hand DNS is most efficient due to least modeling assumptions but is excessively costly and mostly impractical for high Re flows.

To obtain the information of pressure distribution in the flow, data assimilation technique, which combines the theory of modelling with experimental observations can be utilized which has been applied to many practical problems (van Oudheusden 2013). The forces on immersed objects can be determined by momentum and impulse formulations of control volume principles by utilizing this pressure distribution information. The pressure estimation from flow visualization was first reported by (Schwabe 1935). A cinematographic camera was used to

capture images of flow embedded with tracer particles at various times. Velocity distribution from these images were obtained from length of streak lines formed by the tracer particles. For pressure estimation, velocity data were substituted in Bernoulli equation.

$$p + \frac{1}{2}\rho u^2 = p_\infty + \frac{1}{2}\rho u_\infty^2 \tag{1.1}$$

(Imaichi and Ohmi 1983) estimated the pressure in cylinder flow by using Navier-Stokes equation. Later (Willert and Gharib 1991b) used digital PIV for pressure estimation. Instantaneous pressure determination for unsteady flows can be done by substituting measured PIV data into Navier -Stokes equation shown below:

$$\nabla p = -\rho \frac{D\mathbf{u}}{Dt} + \nu \nabla^2 \mathbf{u} \tag{1.2}$$

Here $\frac{D\mathbf{u}}{Dt}$ is material acceleration. In Eulerian perspective this term is decomposed in local and convective accelerations.

$$\frac{D\mathbf{u}}{Dt} = \frac{\partial \mathbf{u}}{\partial t} + (\mathbf{u} \cdot \nabla)\mathbf{u} \tag{1.3}$$

Usually second order central differencing scheme is used to discretize all the terms. Here, calculation of the local acceleration term is very sensitive because it depends on the recording frame rate as well as flow velocity. It is difficult to optimize this factor because it depends on the time resolution features of camera. For example, to resolve the flow structures in supersonic flows the available high-speed cameras are insufficient. Also, the error in local acceleration is inversely proportional to time separation between two images. $\varepsilon_{\frac{\partial \mathbf{u}}{\partial t}} = \frac{\varepsilon_u}{2\Delta t^2}$ here time separation has opposite effect on truncation error. (Jensen and Pederson 2004) proposed the optimal time separation to minimize the total error

In Lagrangian formulation, material acceleration can be defined as:

$$\frac{D\mathbf{u}}{Dt} = \frac{d\mathbf{u}_p(t)}{dt} = \frac{d\mathbf{u}_p(\mathbf{x}_p(t),t)}{dt} \tag{1.4}$$

In this approach positions of all individual particles are tracked. Any discrepancy in true and estimated particle position could raise serious issues in estimated velocity. But this error could be reduced by more accurate trajectory reconstruction method (Murai et al. 2007).

In Eq. (1.4) $\mathbf{x}_p$ and $\mathbf{u}_p$ are particle position and velocity and ν is kinematic viscosity respectively. Once distribution of pressure gradients is determined from Navier-Stokes equation, direct integration needs to be performed to evaluate the pressure field.

$$p(s) = p(s_{ref}) + \int_{s_{ref}}^{s} \nabla p.ds \tag{1.5}$$

Here s_{ref} is pressure at a reference location, usually given by appropriate boundary conditions. In past, several integration approaches have been reported e.g. space marching integration (Baur T 1999), pseudo tracking (Jensen et al. 2003), omni directional integration approach (Liu and Katz 2006), least square approach (Jeon et al. 2018a) and direct spatial integration (Schneiders and Scarano 2016).

Several merits and demerits of Lagrangian (Liu and Katz 2006) and Eulerian (Charonko et al. 2010) approaches are reported in previous studies. Such as Lagrangian approach is less prone to measurement noise than the Eulerian approach (Violato et al. 2011). However, (Jakobsen et al. 1997) found that for waves impinging on a vertical wall, Lagrangian approach showed bias effects and performed worse than Eulerian approach. Because of these contradictory findings, (de Kat and van Oudheusden 2012) performed direct comparison of both the methods in a synthetic flow field. They found out that both the methods work well if interrogation window is at least five times smaller than the flow structure.

Pressure Poisson equation

Pressure Poisson is derived by taking divergence of Navier-Stokes equation

$$\nabla^2 p = -\rho \nabla \cdot (\mathbf{u} \cdot \nabla) \mathbf{u} \quad \rightarrow -2\rho \left(\frac{\partial u}{\partial x} \frac{\partial v}{\partial y} - \frac{\partial u}{\partial y} \frac{\partial v}{\partial x} \right)_{if\,2D} \tag{1.6}$$

This equation does not contain the time derivative term. So, it is very useful for pressure estimation in unsteady flows (Pan et al. 2016). However, pressure Poisson equation is very sensitive to boundary conditions which are practically unknown in most of the cases. Generally, Dirichlet and Newmann condition are needed. Dirichlet condition is usually determined by modified Bernoulli equation (Van der Kindere et al. 2019) and Neuman boundary conditions are given by momentum conservation equations (Gresho and Sani 1987). Among them Neumann boundary condition is physically more accurate (Gurka et al. 1999).

Despite of several advantages of PIV and its applicability in providing pressure distribution by combining with CFD, it is not applicable in opaque fluids. Also, the pressure estimation for non-Newtonian fluids has never been reported in literature even when plenty of research has been already performed in last two decades for the improvement of pressure estimation in Newtonian fluid by PIV. The pressure estimation in opaque and non- Newtonian fluids is the real demand of industries.

1.2 Objective

Motivated by above unresolved problems, the present thesis has four major objectives

1.1 To develop a novel pressure estimation technique which can be used in opaque Newtonian fluids

2.1 To develop a unique pressure profiler for transparent non-Newtonian fluids based on PIV measurements

3.1 To develop an algorithm for pressure profile in spatio- temporal domain for opaque non-Newtonian fluids

4.1 A framework of error analysis and correction for instantaneous pressure estimation

1.3 Organization of thesis

In this thesis, introduction described the existing pressure estimation techniques using experimental data and addresses the motivation of present study, experimental arrangements are described in chapter 2. In chapter 3, a pressure estimation algorithm for opaque Newtonian fluids is discussed. In chapter 4, the pressure estimation is extended to shear thinning fluid flows. For shear thinning fluids pressure estimation algorithm is developed using momentum equation and rheology together. The algorithm is applied in steady and unsteady flows and its capability is assessed. In chapter 5, for unsteady separated vortex flows, another algorithm is proposed which is also applicable in opaque fluid flows. In chapter 6, to correct the estimated pressure field from experimental data, a novel irrotational correction method is developed. Analytical fields with random or correlated random errors are tested. In last section the present method is tested in real experimental PIV data. In chapter 7, conclusions and future directions of present study are discussed.

Chapter 2

Experimental method

This chapter describes the experimental setup for measurement of vortex shedding behind circular cylinder. Measurements were conducted in Newtonian and non-Newtonian fluids by UVP (Ultrasonic Velocity Profiler) and PIV techniques in towing tank facility for several experimental conditions.

2.1 Experimental arrangement for measurement by UVP

UVP is a well-established fluid measurement technique in experimental fluid mechanics (Takeda 2012). UVP transducer emits the ultrasound pulse in fluid containing tracer particles and receives echo. From time lapse between emission and echo reception the position of the particle can be obtained by:

$$X = \frac{c\Delta t}{2} \tag{2.1}$$

Here c is velocity of sound and Δt is time lapse. Similarly, the instantaneous velocity at a point can be obtained by Doppler shift frequency (f_D) of the echo and basic frequency of ultrasound (f_0).

$$v = \frac{cf_D}{f_0} \tag{2.2}$$

As ultrasound signals can penetrate various fluids easily irrespective of whether they are transparent or not, UVP can also be used for pressure measurement in opaque fluids such as food materials, chemicals and blood flows for which traditional flow visualization techniques are unsuitable. UVP can provide the spatio-temporal information of flow at higher resolution than hot wire anemometer and laser Doppler anemometer, but it provides velocity information in one line only i.e. one dimensional one component (1D-1C) velocity information of flow. Even with this limitation, UVP is more suitable for longer duration measurement than PIV because the memory requirement is significantly less than that for 2D PIV or 3D PIV.

To study the vortex shedding in flow behind cylinder, a towing tank setup was used in which a moving carriage towed the cylinder at constant velocity in stationary fluid. The dimension of towing tank was 5.00 m length (*l*), 0.54 m width (*w*) and 0.45 m height (*h*). The cylinder dimension is 0.04 m diameter and 0.40 m length. The cylinder material was acrylic resin. The cylinder was fixed on carriage by fixtures and submerged at *h*/2 distance from bottom of tank. The position of cylinder ensured no additional effect of free surface and bottom boundary. The experimental setup is shown in Fig. 2.1. For measurement in Newtonian fluid, towing tank is filled with water and milk with concentration of 0.1 % and for non-Newtonian fluid flow measurement, aqueous solution of CMC of 0.1 weight % was used.
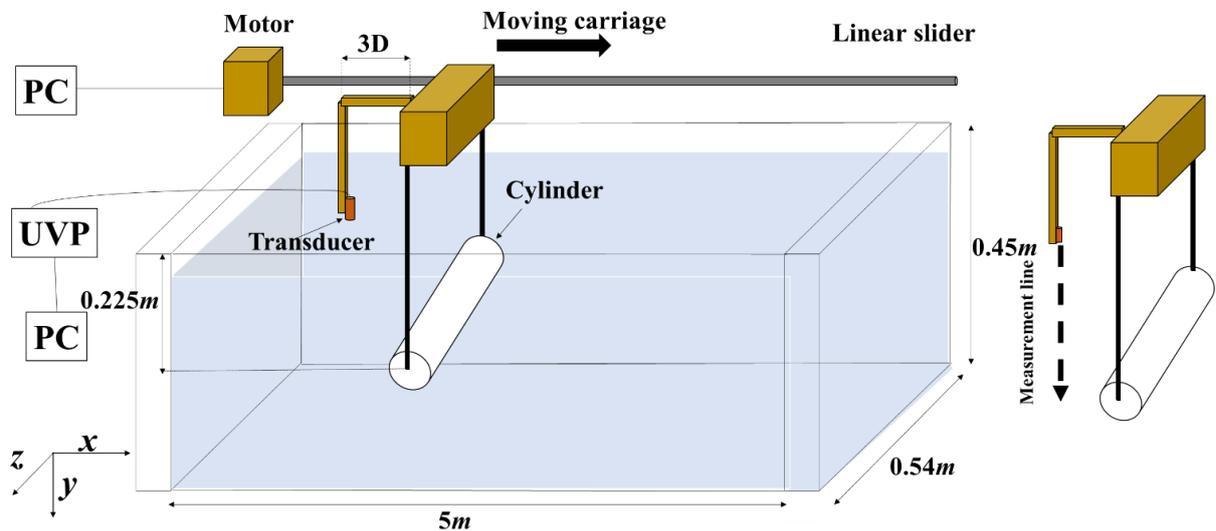
Fig. 2.1 Experimental setup for *y*-component of velocity measurement by UVP system

In both Newtonian and non-Newtonian fluid flow experiments, spherical tracer particles were mixed in working fluid. For all of the experimental cases, tracer particles which has high porous polymer with hydrophilic property to aqueous solution (HP20SS manufactured by Mitsubishi chemicals) was used. The diameter and density of particles are 50-120 µm and 990 kg/m^3.

For velocity measurement, a UVP transducer of 4 MHz basic frequency was used with UVP monitor model Duo (Met-flow S.A., Switzerland). The transducer was fixed at 3 times diameter downstream of cylinder and towed with cylinder along length of tank. The cylinder was fixed vertically in all of the test conditions, so, *y* component of velocity was measured in spatio-

temporal domain. In experiments with Newtonian fluids, the towing speed was $U = 39.2$ mm/s, $\mathrm{Re} = \rho U D / \mu = 1000$. In non-Newtonian fluid the towing speed was set to $U = 10$ to 40 corresponding $\mathrm{Re} = \rho U D / \mu_0 = 30$ to 100. Here μ_0 is zero shear viscosity.

2.2 Experimental arrangement for measurement by PIV

PIV (Particle image velocimetry) is an optical measurement approach which provides the velocity information of flow field in 2D/3D plane/volume quantitatively. For PIV experiments, fluids are seeded with tracer and these particles are illuminated in laser light in a plane. The images of these illuminated particles within a frame is captured with a high-speed camera. To evaluate the velocity distribution, cross correlation algorithms (Dabiri 2009), Fast Fourier Transform cross correlation (Pust 2006), minimum quadratic difference (Gui and Merzkirch 1996) and normalized cross correlation (Thomas et al. 2005) are generally opted. Recently machine learning based fast algorithm promises higher special resolutions (Rabault et al. 2017) (Cai et al. 2019).

Conventional two-dimensional PIV technique uses one camera to capture the motion of particles in a single plane and ignores out of plane velocity component which is a source of error in highly turbulent flows. Therefore, 3D (three-dimensional) PIV techniques were developed. 3D PIV measures three-dimensional velocity components in three dimensions (3D3C). Some of the 3D PIV techniques are stereoscopic PIV (Prasad 2000) and Tomo PIV (Lynch and Scarano 2014). The advancement of PIV also expanded the capability of pressure estimation algorithms based on CFD governing equations in three dimensions (Schneiders et al. 2016).

The PIV measurements in both Newtonian and non-Newtonian fluid flows are conducted in towing tank facility described in section 2.1. The dimensions of cylinder and position of cylinder is also same. For illuminating flow, tracer particles (HPSS20, Mitsubishi Chemical, Ltd) are used. The cylinder camera and laser are towed together by carriage for the tank length which enables the measurement up to 100 times diameter of cylinder.
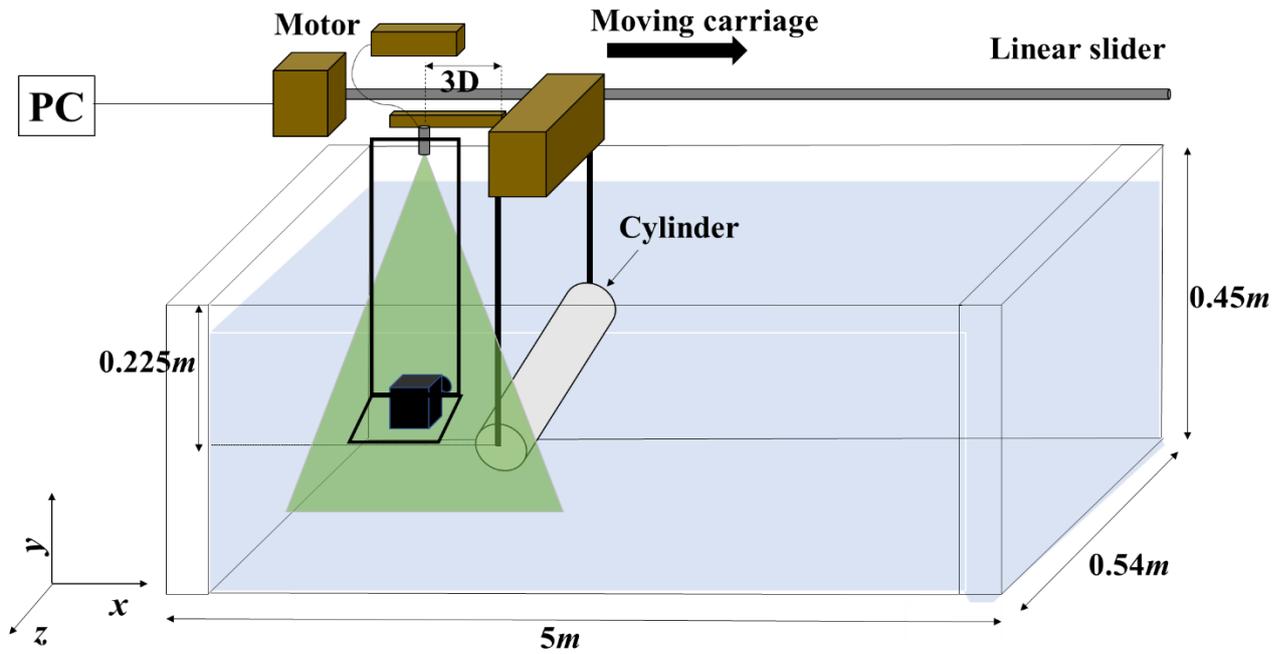
Fig. 2.2 Experimental setup for two-dimensional velocity components measurement by PIV

To capture fluid flow images, a high-speed camera with 300mm Nikkor lens was used. For illumination green laser was used. The laser beam is installed at 3D downstream of cylinder which expands the illumination up to 3D downstream of cylinder. The camera is set to capture the images in x-y plane. In all of the test cases the images are obtained at 50 fps (frames per second) with images of 1024×1024 pixels. Experimental arrangement for PIV measurement is shown in Fig. 2.2. The postprocessing of images was performed by PIVLAB (Thielicke and Stamhuis 2014) in MATLAB software. FFT based cross correlation recursive iterative multigrid approach (Scarano and Riethmuller 1999) with stepwise interrogation window area from 128×64, 64×32, and 32×16 was performed to obtain velocity data.

Chapter 3

Pressure field estimation in opaque flow by UVP

3.1 Introduction

Opaque fluids are commonly found in pharmaceutical, food and material industries. These fluids are inseparable from our daily life such as syrups, milk, coffee, juices, shampoo, toothpaste, ketch up, cornstarch, liquid metals etc. For quality control during manufacturing and maintenance operations in addition to material property, the information of flow variables such as velocity and pressure are also essential.

Pressure measurement can be done in opaque fluids by piezo electric transducer, manometers etc. These measurement devices are intrusive in nature and are limited to give information at a single point which is not sufficient to understand the entire flow field. On the other hand PIV based pressure estimation is now a well-established technique in experimental fluid mechanics community (van Oudheusden 2013) (Sciacchitano et al. 2012) (Suzuki and Yamamoto 2015). With consistent efforts of researchers for development of PIV (Willert and Gharib 1991) (Grant 1997) and pressure estimation methodologies (de Kat and van Oudheusden 2012) complete information of flow governing variable can be obtained from experiments (van Gent et al. 2017) (Schneiders and Scarano 2016). However, to measure opaque flows, optical flow measurement techniques such as LDA (Laser Doppler anemometry) and PIV cannot be used. The details of available velocity and pressure measurement devices are listed in Table 1.

UVP is now well accepted velocity measurement tool in fluid engineering (Takeda 2012) (Aritomi et al. 1996) (Ihara et al. 2013). It had been successfully applied in food (Yoshida et al. 2019), metallic flows (Ueki 2016) and even in environmental flows (Yokoyama et al. 2006). Due to capability of UVP, it is the best alternative for pressure estimation in opaque flows. UVP can provide one component of velocity vector in one dimension in spatio-temporal domain so the pressure estimation from governing equations 1.1 and 1.2 in general 3-D flow is impossible

by UVP due to large number of unknowns. Extension of UVP measurements in two and three dimensions is still a challenge (Obayashi et al. 2008) (Takeda 1995) (Jensen et al. 2016). Coupling of UVP data with additional flow governing equations could be a possible option to evaluate additional information of flow. This makes the pressure estimation from UVP measurements far more challenging than from PIV measurements.

Table 1 velocity and pressure measurement devices

Device	Pressure measurement Device			Velocity measurement device			
Device	Piezoelectric transducer	Pitot tube Manometer	PSP	LDV HWA ADV	UVP	PIV PTV MTV	3D-PTV Tomo-PIV Color PTV
Dimension	Point	Point	2D	Point	1D	2D	3D
Opaque fluid	Yes	Yes	No	No	Yes	No	No
Non-intrusive	No	No	Yes	Yes	Yes	Yes	Yes

Abbreviations: PSP: pressure-sensitive paint, HWA; hot-wire anemometer, ADV: acoustic Doppler velocimeter, UVP: ultrasound velocity profiler, PIV: particle image velocimetry, PTV: particle tracking velocimetry, MTV: molecular tagging velocimetry, 3D-PTV: 3D-stereoscopic particle tracking velocimetry, Tomo-PIV: tomographic particle image velocimetry, Color-PTV: color-coded volumetric particle tracking velocimetry.

3.2 Estimation of x component of velocity by equation of continuity

The velocity measurements were performed in the experimental setup (Fig. 2.1) in water. UVP measured the y component of data, $v(x, t)$ in spatio-temporal domain as shown in Fig. 3.1. Here the alternate positive and negative velocity regions show the von Karman vortex street.

The pixelized experimental noise appeared in the data due to electrical connections and model vibrations during measurement.
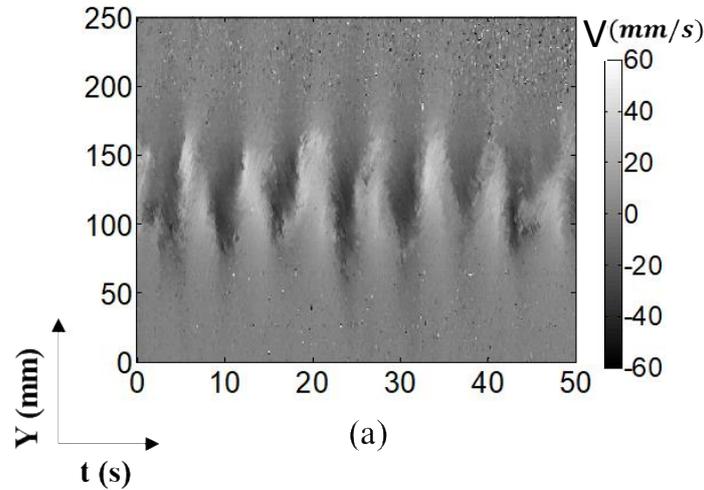
Fig. 3.1 UVP measured *y* component of velocity in spatio-temporal domain

The UVP data in $t-Y$ domain is then converted to X-Y domain by utilizing the concept of Taylor Frozen hypothesis i.e. $v(x, y) = v(x_0 - U_s.t, y)$, here U_s is the mean convection velocity of flow structure passing by $x = x_0$. The convection velocity is 60% of free stream velocity as measured by (Lin and Hsieh 2003). In convection dominated flows, Taylor Frozen hypothesis can improve the pressure evaluation (De Kat and Ganapathisubramani 2013) and overcome the difficulties encountered while solving the Navier-Stokes equation or pressure Poisson equation with Eulerian approach (De Kat and Van Oudheusden 2012).

Once first component of velocity is obtained in *x-y* domain, the equation of continuity can be utilized to obtain the other unknown component of velocity if we assume flow is two dimensional. The equation of continuity can then be written as:

$$\frac{\partial u}{\partial x} + \frac{\partial v}{\partial y} = 0 \tag{3.1}$$

Here *v* component of velocity is measured, so by substituting it in Eq.3.1, the other component *u* can be obtained by integration.

$$u(x, y) = -\int \frac{\partial v(x, y)}{\partial y} dx \qquad (3.2)$$

This equation is discretized by second order central difference method. The integration of above equation is performed in forward direction, backward direction and oblique direction as shown in Fig. 3.2. In forward and backward direction approach the space marching is performed in forward and backward direction. In the case of oblique direction approach, space marching is performed in all four directions as shown in Fig. 3.2(c) and average velocity of all four direction is considered as the final solution.
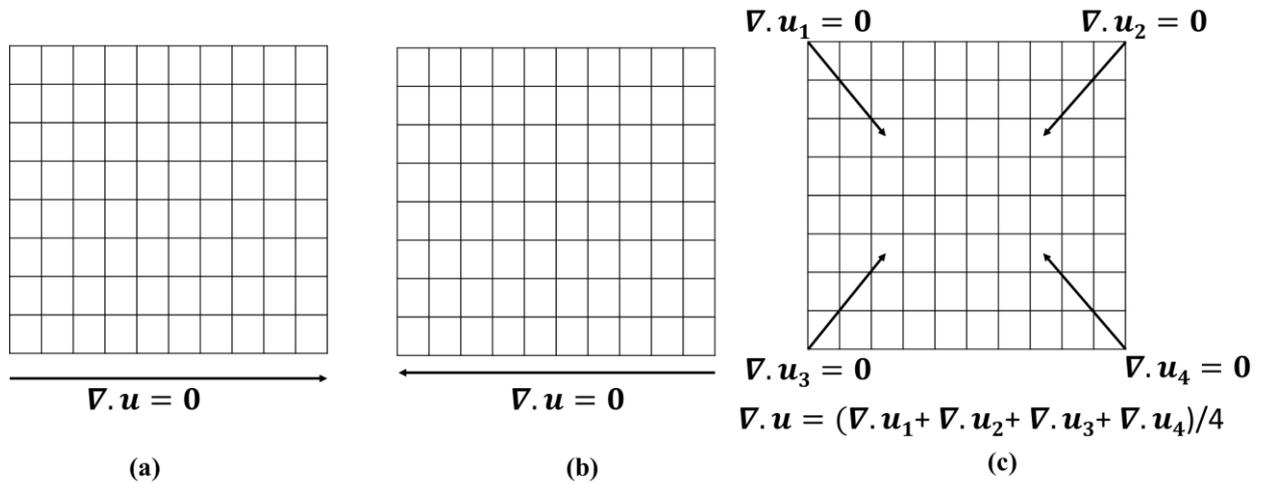
Fig. 3.2 Integration to evaluate x component of velocity by marching in (a) forward direction (b) backward direction (c) oblique direction

3.3 Filtering of UVP data

To filter the noises from velocity data measured by UVP, various filtering methods are used as follows:

3.3.1 Low pass Filtering

The direct substitution of noisy UVP data into governing equations could result in unrealistic pressure field so a very careful preprocessing method is required for this purpose. For UVP data, FFT (fast Fourier Transform) based low pass filtering was applied to remove high frequency noise. The power spectrum plotted in Fig. 3.3, for UVP data measured at time between t=0 to 50 seconds. The dominant frequency of flow structures was obtained around at

14

f=1.2 Hz which indicated that the periodic vortex shedding structures are present within *f*=0 to 2 Hz. Hence, the cutoff frequency is chosen as 3 Hz to remove the noise containing higher frequencies.
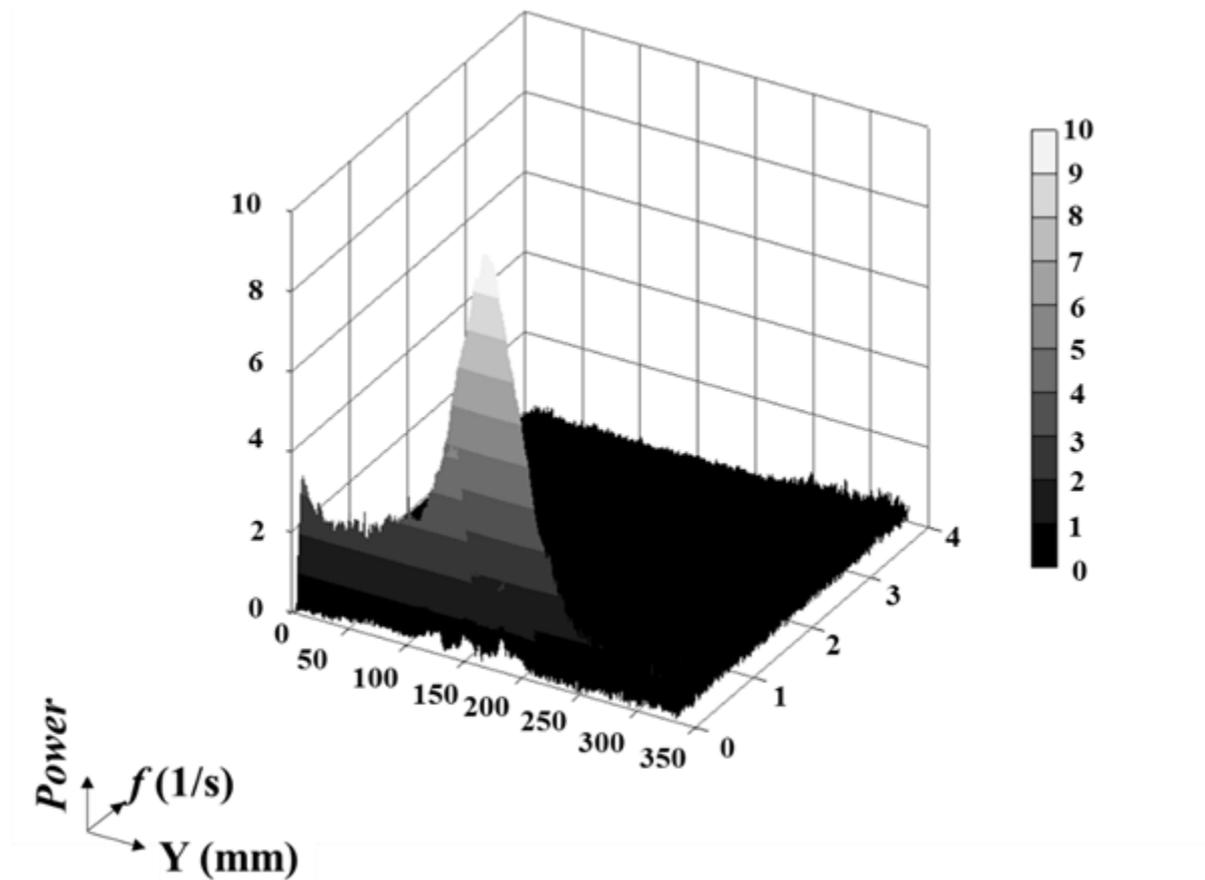
Fig. 3.3 Power spectrum of UVP measured data in flow behind the cylinder

The velocity data after FFT filtering is shown in Fig 3.4. The pixelized noise in the free stream region is removed and smoother velocity distribution is obtained which is why the FFT filtering is often known as FFT smoothing. These changes can be seen by comparing Fig. 3.4 to Fig. 3.1.
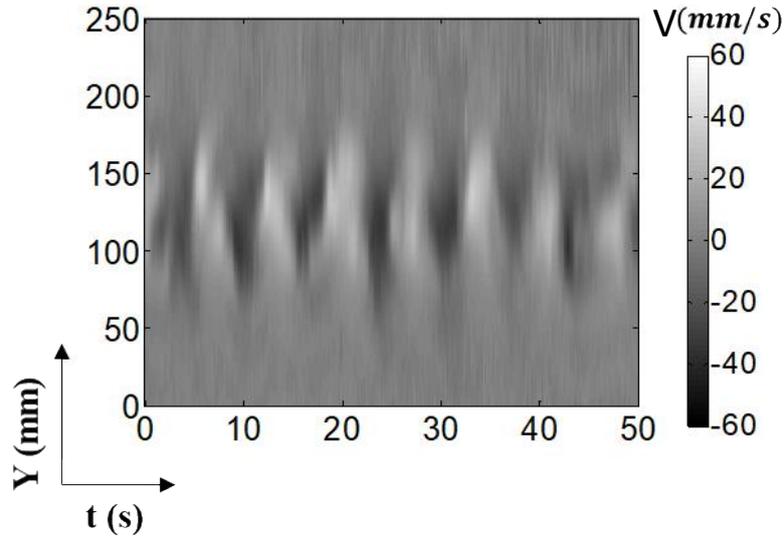
Fig. 3.4. Distribution of *y* component of velocity after applying FFT low pass filtering remove data corresponding to *f*>3.0Hz.

3.3.2 Proper orthogonal decomposition

POD (Wiklund et al. 2012) is often used as a post processing technique to analyze the large data (Meyer et al. 2007). In pressure estimation problems, POD filtering is the most efficient physics-based filtering (Charonko et al. 2010b). The experimental data can be decomposed in orthonormal basis functions. From which POD eigen values can be obtained which resolve the kinetic energy of flow. Generally, dominant flow structures are represented by first few POD modes. In this study the 'snapshot POD' (Sirovich 1987) is used for filtering UVP data. The first step involves the separation of fluctuating component from mean velocity data. When POD is performed with PIV data the velocity matrix containing N snapshots can be arranged as below:

$$\mathbf{u} = \begin{bmatrix} u^1 & u^2 & & u^N \end{bmatrix} = \begin{bmatrix} u_1^1 & u_1^2 & & u_1^N \\ & & & \\ u_m^1 & u_m^2 & & u_m^N \\ v_1^1 & v_1^2 & & v_1^N \\ & & & \\ v_m^1 & v_m^2 & & v_m^N \end{bmatrix} \tag{3.3}$$

In present study POD is performed in UVP data for that only y component of velocity in measurement line (shown in Fig. 3.1) from t=0 to 50 seconds with 511 profiles is available. Each profile can be treated as a snapshot and arranged as Eq.3.3. Then covariance matrix can be generated as:

$$R = \mathbf{u}^T \mathbf{u} \tag{3.4}$$

Corresponding eigen value problem can be written as

$$RC^i = \lambda^i C^i, \qquad i = 1, \ 2, \ldots \ldots 511 \tag{3.5}$$

After obtaining eigen values solution can be arranged as below:

$$\lambda^1 > \lambda^2 > \ldots \ldots \ldots \lambda^{511} = 0 \tag{3.6}$$

Then POD modes can be constructed from basis obtained from eigen vectors

$$\varphi^i = \frac{\displaystyle\sum_{n=1}^{n=N} C_n^i \boldsymbol{u}^N}{\left\| \displaystyle\sum_{n=1}^{n=N} C_n^i \boldsymbol{u}^N \right\|} \tag{3.7}$$

Then POD modes can be arranged as

$$\psi = \begin{bmatrix} \varphi^1 \ldots \ldots \ldots \varphi^{511} \end{bmatrix} \tag{3.8}$$

POD coefficients can be obtained by projecting fluctuating part of velocity onto POD modes and can be represented as below

$$a^n = \psi^T u^n \qquad (3.9)$$

Using this coefficient, the velocity can be reconstructed as

$$u^n = \psi \, a \qquad (3.10)$$

For measured UVP data, POD modes and corresponding energy content are shown in Fig. 3.5. Here first mode itself contains the 82.6% of total kinetic energy and subsequent reduction is observed from second mode onwards. However, in cylinder flow usually the first and second mode contains almost 40% and 40% of energy. The possible reason for this discrepancy is that the velocity is measured at a fixed line by UVP transducer fixed at 3D downstream to cylinder and the velocity is reconstructed in spatio-temporal domain but not space-space two dimensions. Since all the vortices in one plane are captured at same position relative to cylinder, about 82.6% of energy involves in first mode itself. In Fig. 3.6. y component of velocity is reconstructed by considering four cases, i.e. POD mode 1, POD mode 1 to 3, POD mode 1 to 5 and POD mode 1 to 10. Here data corresponding to POD mode 1 to 10 contains 99.9% of total kinetic energy. In velocity data reconstructed only by POD mode 1, the most dominant structures of the flow are obtained. As more higher modes are considered the energy content increases and smaller eddies also showed up in the data.
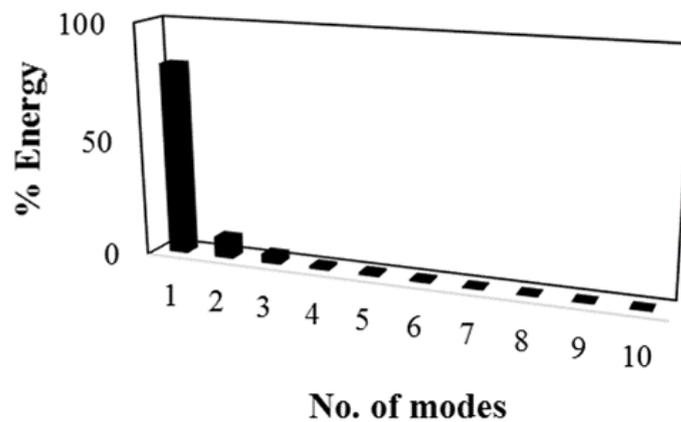
Fig. 3.5. Kinetic energy variation with POD modes in UVP data measured at cylinder downstream
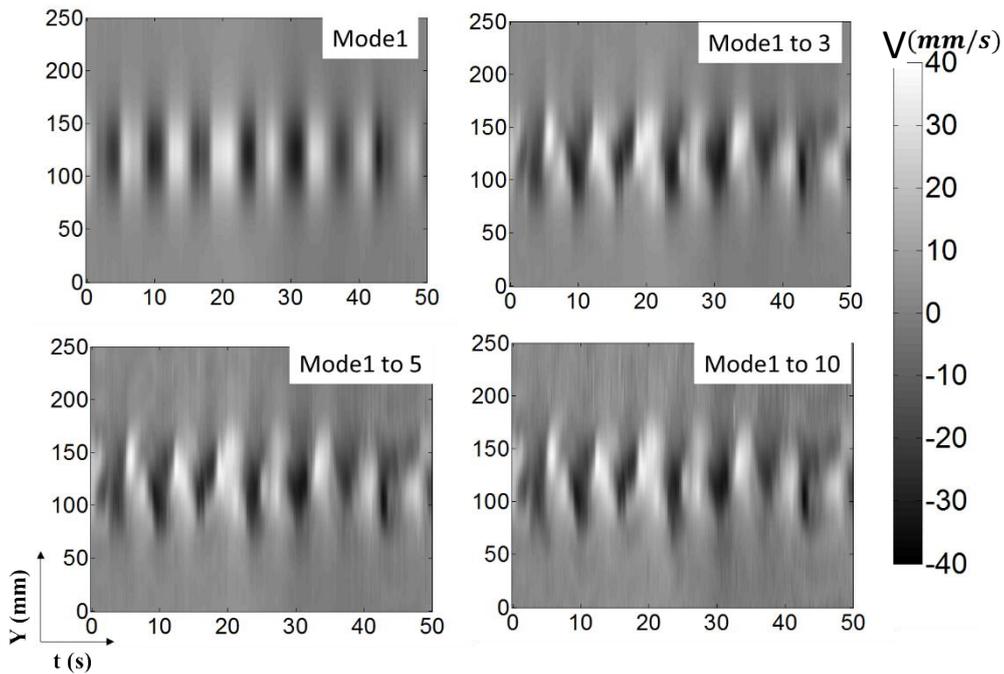
Fig. 3.6 *y* component of velocity (*v*) after applying POD for corresponding mode 1, 1 to 3, 1 to 5, 1 to 7

3.3.3 Optimize filtering to evaluate unknown velocity component

To reconstruct the two-dimensional flow structure in wake, the velocity data measured by UVP and velocity data evaluated from the equation of continuity both are required. FFT based low pass filtering and POD are applied in measured data. Then three type of approaches are used to integrate the velocity from equation of continuity i.e. forward, backward and oblique (Fig. 3.2). The performance of filtering techniques was judged by its capability to reconstruct two-dimensional vortex structures and vorticity. First FFT and POD filtering were applied on measured velocity data and *u* component of velocity was reconstructed as shown in Fig. 3.7. The results of forward and backward approaches were same so only results of forward approach are presented. Similarly, FFT and POD filtering were applied on measurement data and vorticity (ω) was reconstructed by forward and oblique approach.

Here the ω can be defined as.

$$\omega = \nabla \times \boldsymbol{u} \cdot (0,0,1)^T = \frac{\partial v}{\partial x} - \frac{\partial u}{\partial y} \qquad (3.11)$$

This equation is discretized with second order central difference scheme.

The reconstructed u and ω are shown in Figs. 3.7 and 3.8 respectively. Error in reconstructed field by applying oblique approach was more than with forward approach which can be seen in plots of both u and ω. However, FFT filtering with forward approach was not suitable to reconstruct the flow structures accurately. On the other hand, forward approach with POD filtering, u component is reconstructed in the wake but the ω distribution was not accurate due to error propagation from velocity uncertainty in curl of velocity data.
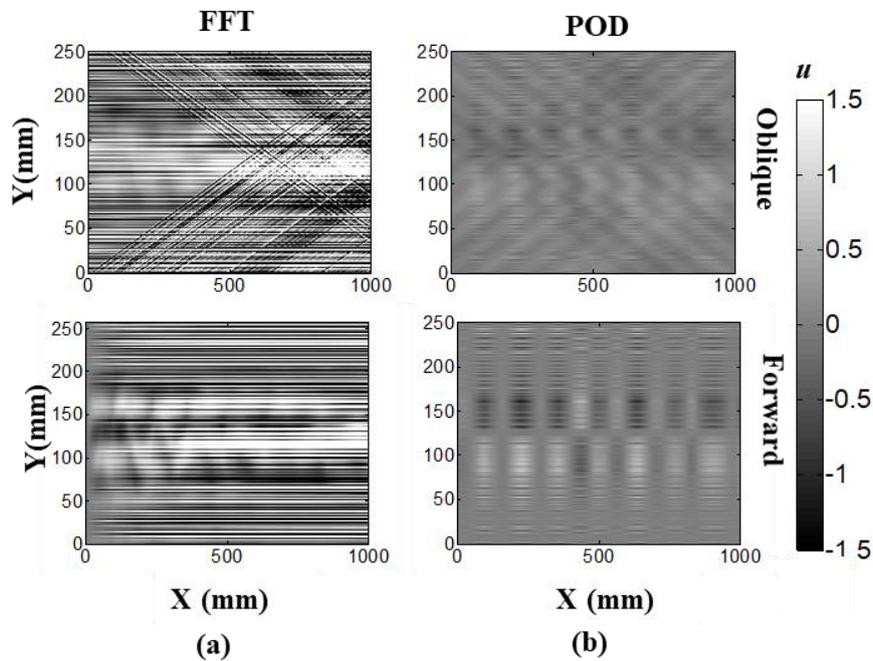
Fig. 3.7 *u* component of velocity obtained by equation of continuity by substituting (a) FFT filtered velocity data (b) POD filtered velocity data

Next, FFT and POD filtering both were applied together for global noise reduction in velocity data and similar to previous cases oblique and forward directional approaches were used to calculate u from equation of continuity. The reconstructed u and ω are shown in Fig. 3.9. The distributions of u and ω are more realistic with forward approach than oblique approach. An

alternate positive and negative pattern of velocity and ω are clearly visible in forward approach.

The order of filtering by FFT and POD does not make any difference in the result.
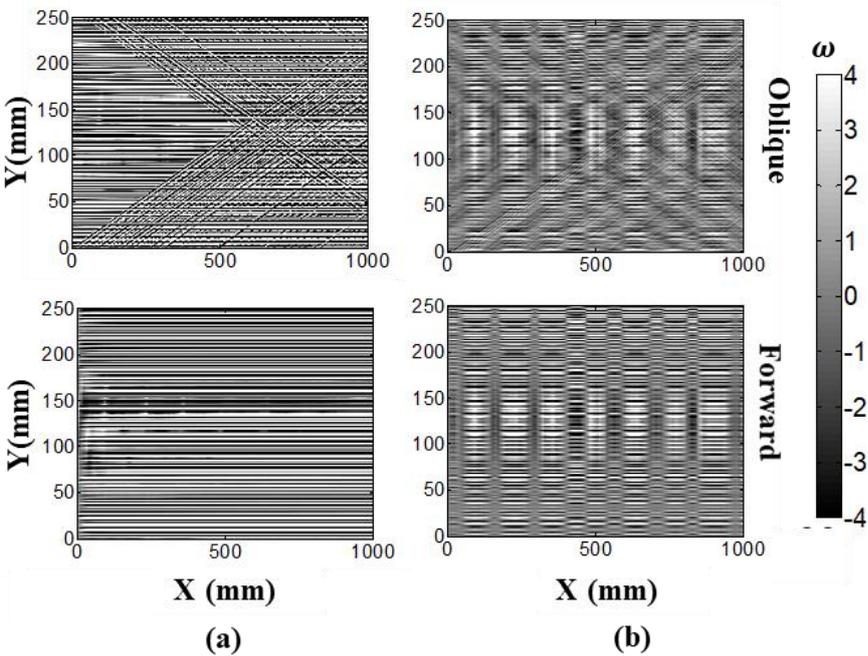
Fig. 3.8 u component of velocity obtained by equation of continuity by substituting (a) FFT filtered velocity data (b) POD filtered velocity data
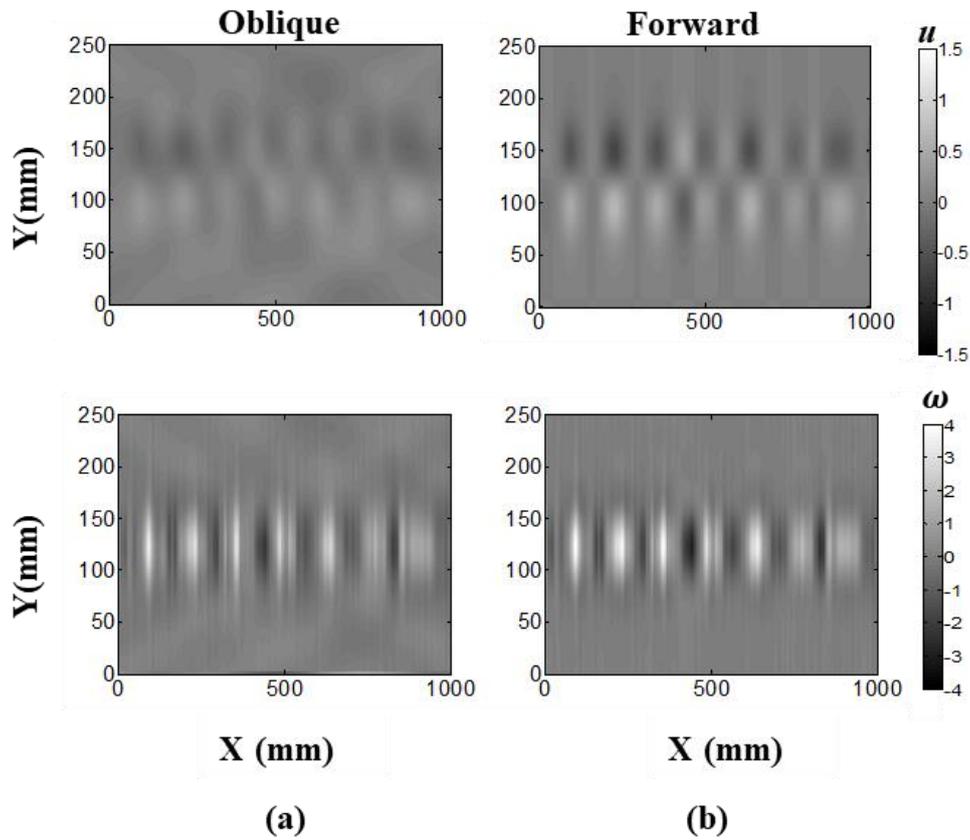
Fig. 3.9 FFT and POD filtered, *u* component of velocity and vorticity obtained by equation of continuity by (a) Oblique approach (b) Forward approach

3.4 2D velocity reconstruction

The 2D velocity vector field reconstructed by applying FFT and POD filtering with forward approach in UVP data, considering POD mode 1, POD mode 1 to 3, POD mode 1 to 5 and POD mode 1 to 10 as shown in Fig. 3.10. In Fig. 3.10 (a) only dominant structures were reconstructed but in Fig. 3.10 (b) the staggered pattern of vortices was successfully reconstructed (zoomed view is shown in Fig. 3.11). When higher modes are considered smaller vortices were reconstructed in the free stream region (Fig. 3.10 (c), (d)). The Strouhal number (*St*) of flow is 0.21, which is in agreement with the literature (Fey et al. 1998) (Azmi and Zhou 2018). Here

$$St = \frac{fd}{U} \, .$$
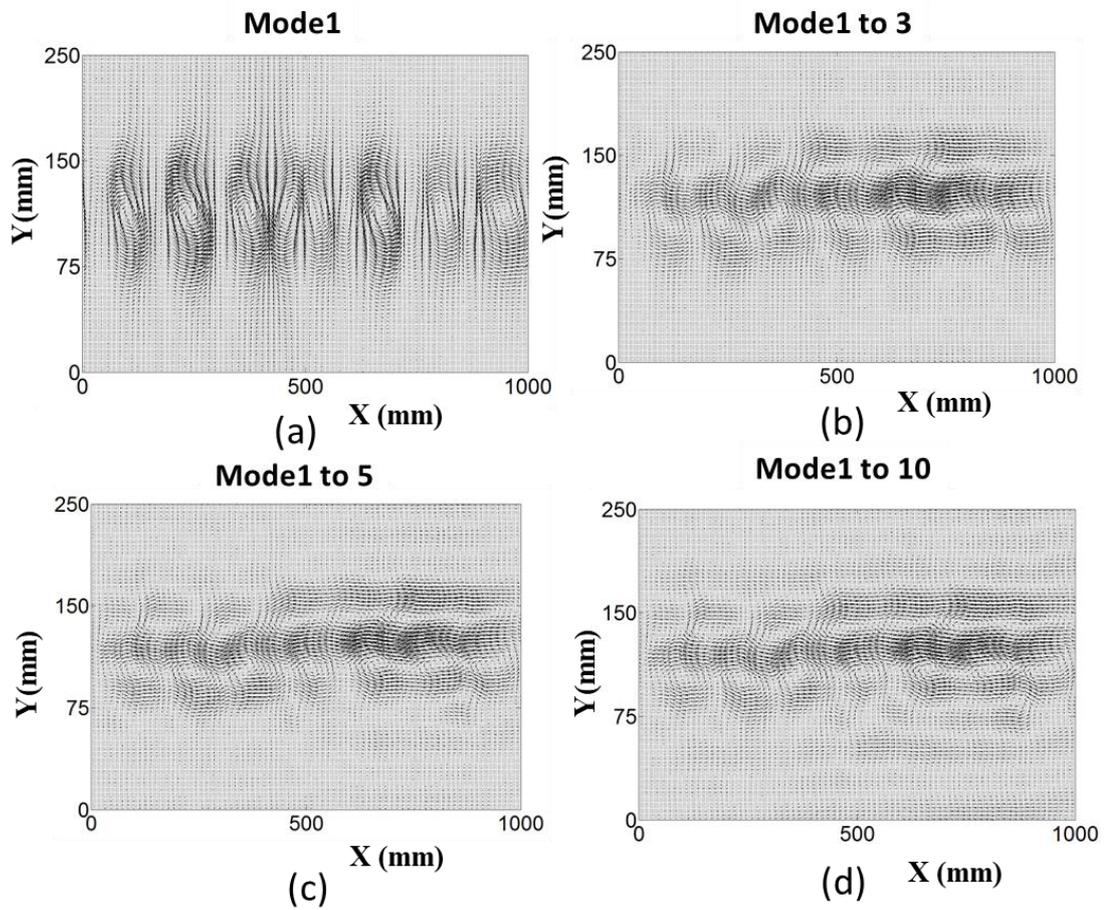
Figure 3.10 Velocity vector plot considering (a) POD mode 1 only (b) POD mode 1 to 3 (c) POD mode 1 to 5 (d) POD mode 1 to 10
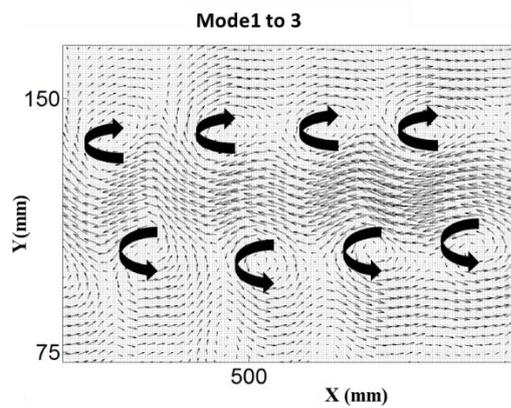
Fig. 3.11 Zoomed velocity vector field corresponding to POD mode 1 to 3. Here staggered arrangement of vortices is clearly observed.

3.5 Pressure field reconstruction

To reconstruct pressure field, the velocity data (section 3.4) was substituted in Navier-Stokes equation Eq.1.2. The local acceleration term can be neglected for convection dominated flows as long as Taylor Frozen hypothesis is valid (De Kat and Ganapathisubramani 2013). The Navier-Stokes equation was discretized with second order central difference scheme. The discretized form of Navier-Stokes equation can be written as:

$$\left(\frac{\partial p}{\partial x}\right)_{i,j} = -\left(u_{i,j}\frac{u_{i+1,j}-u_{i-1,j}}{2\Delta x}+v_{i,j}\frac{u_{i,j+1}-u_{i,j-1}}{2\Delta y}\right)+$$
$$\frac{1}{Re}\left(\frac{u_{i+1,j}+u_{i-1,j}-2u_{i,j}}{\Delta x^2}+\frac{u_{i,j+1}+u_{i,j-1}-2u_{i,j}}{\Delta y^2}\right)$$

(3.13)

$$\left(\frac{\partial p}{\partial y}\right)_{i,j} = -\left(u_{i,j}\frac{v_{i+1,j}-v_{i-1,j}}{2\Delta x}+v_{i,j}\frac{v_{i,j+1}-v_{i,j-1}}{2\Delta y}\right)$$
$$+\frac{1}{Re}\left(\frac{v_{i+1,j}+v_{i-1,j}-2v_{i,j}}{\Delta x^2}+\frac{v_{i,j+1}+v_{i,j-1}-2v_{i,j}}{\Delta y^2}\right)$$

(3.14)

Once the pressure gradient field is obtained the pressure field can be obtained by least square method (Jeon et al. 2018a).

$$p_{i,j} = p_{i\pm1,j} \mp \left(\frac{\partial p}{\partial x}\right)_{i\pm\frac{1}{2},j}\Delta x, \quad p_{i,j} = p_{i,j\pm1} \mp \left(\frac{\partial p}{\partial y}\right)_{i,j\pm\frac{1}{2}}\Delta y$$

(3.15)
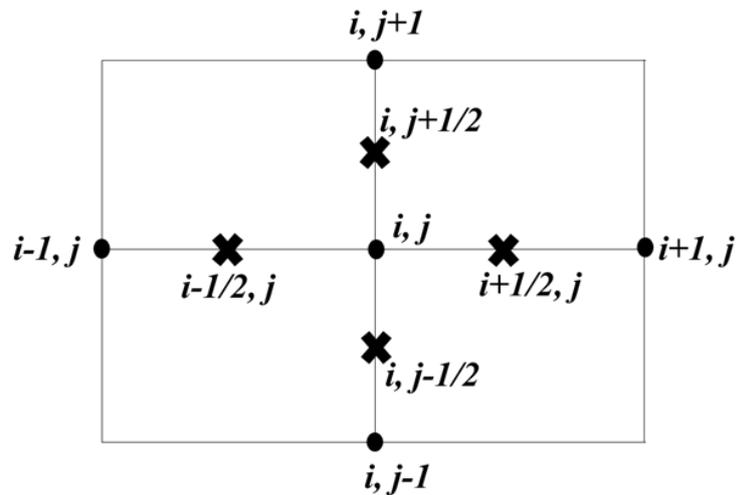
Fig. 3.12 Nodal grid system for calculation of pressure

To solve these equations (Eq.3.14), at least pressure at one corner should be given and at top, bottom, left and right boundaries Neumann boundary conditions were given. The grid points in the neighborhood of a point used for estimation of pressure at a point is shown in Fig. 3.12. The pressure was determined by several iterations and Least square error was monitored at each iteration. Least square error (LSE) can be defined as total sum of discrepancy squared of data. The iterations were performed until LSE reaches 0.0001. LSE will never go to zero because of presence of measurement and numerical errors so minimum value of LSE can provide the optimum solution of pressure.
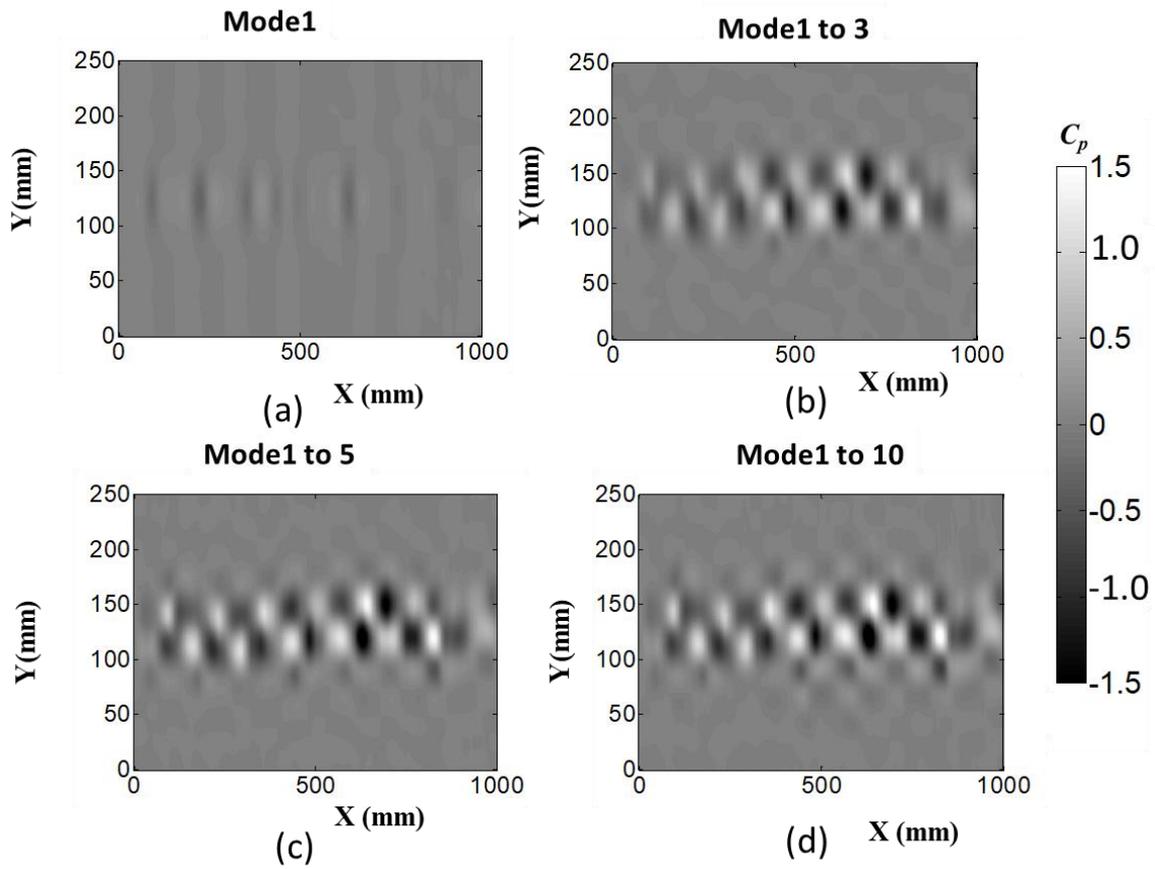
Fig 3.13 the pressure fields C_p are reconstructed by considering POD mode 1, mode 1 to 3 POD mode 1 to 5 and POD mode 1 to 10.

C_p is defined as:

$$C_p = p/\rho U^2 \tag{3.15}$$

Here alternate low and high-pressure regions were reconstructed when at least POD mode 1 to 3 are considered. As higher modes are considered in the data, the additional low-pressure regions appeared in free stream region due to presence of smaller vortices there. The position of minimum pressure coincided with center of vortices in Fig. 3.14. Here velocity vector and pressure field were plotted together for data corresponding to POD mode 1 to 3.
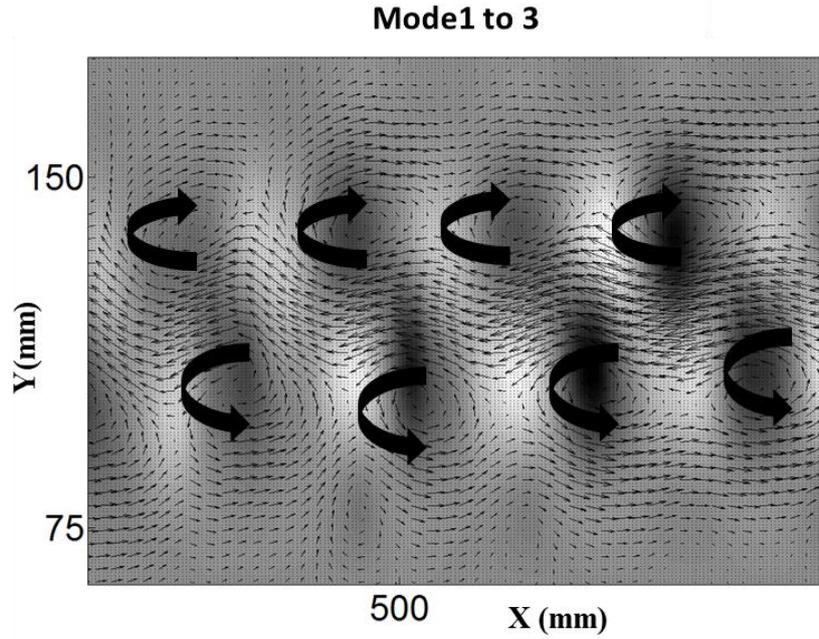
Fig. 3.14 Zoomed velocity vector and pressure field for POD mode 1 to 3

3.6 Correlation between velocity and pressure

Time averaged $\bar{u}$ and $\bar{C}_p$ are shown in Fig. 3.15. Here $Y/D = 0$ represents the center of cylinder.

The lowest pressure points in Fig. 3.15 (b) were obtained between $|Y/D| \sim 1$ which represents

the vortex cores. At $|Y/D|=1$ the increment of $\bar{u}$ is obtained due to convection of vortices. The

magnitude of pressure was maximum at centerline of cylinder and drops in shear layers. This

feature indicated the spatial coupling of pressure and counter-rotating alternating vortices in the

vortex street. Specially the passage of vortex cores reduces the pressure $\bar{C}_p$ in shear layer at

$|Y/D| \sim 1$ and pushes the fluid between vortices at $|Y/D| = 0$.

The correlations of pressure with kinetic energy, vorticity and Q value are shown in Fig. 3.16.

Q value is defined as:

$$Q = \left(\frac{\partial u}{\partial x} \frac{\partial v}{\partial y} - \frac{\partial u}{\partial y} \frac{\partial v}{\partial x} \right)_{if\ 2D} \tag{3.16}$$

27
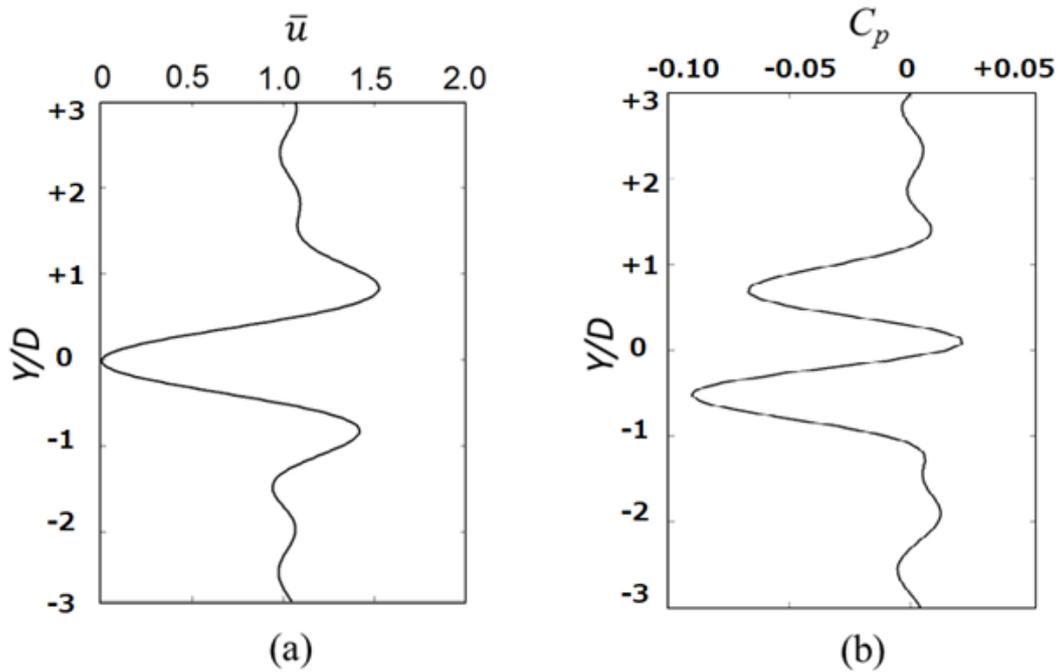
Fig. 3.15 Time averaged velocity and pressure profiles in wake of cylinder

In Fig 3.16 (a) the measured pressure is represented by circles and pressure calculated by Bernoulli's equation: $C_p = u^2/2$ is represented by solid dots. The deviation of Bernoulli's equation clearly showed its inability to estimate flow in rotational flow. The parabolic trend of pressure with vorticity represents the dominance of rotational motion in governing pressure as shown in Fig. 3.16 (b). In Fig. 3.16 (c) the inverse relation of pressure with Q value was confirmed.

3.7 Validation with PIV data

The PIV measurements were conducted to measure velocity in flow behind cylinder in water in the experimental set up shown in Fig. 2.2. The velocity data at $t=80$ s were substituted in Eq.3.12, 3.13 to obtain pressure gradients. Then pressure distribution was obtained by integrating pressure gradients as in Eq. 3.14. The measured velocity and estimated pressure distributions are shown in Fig. 3.17.
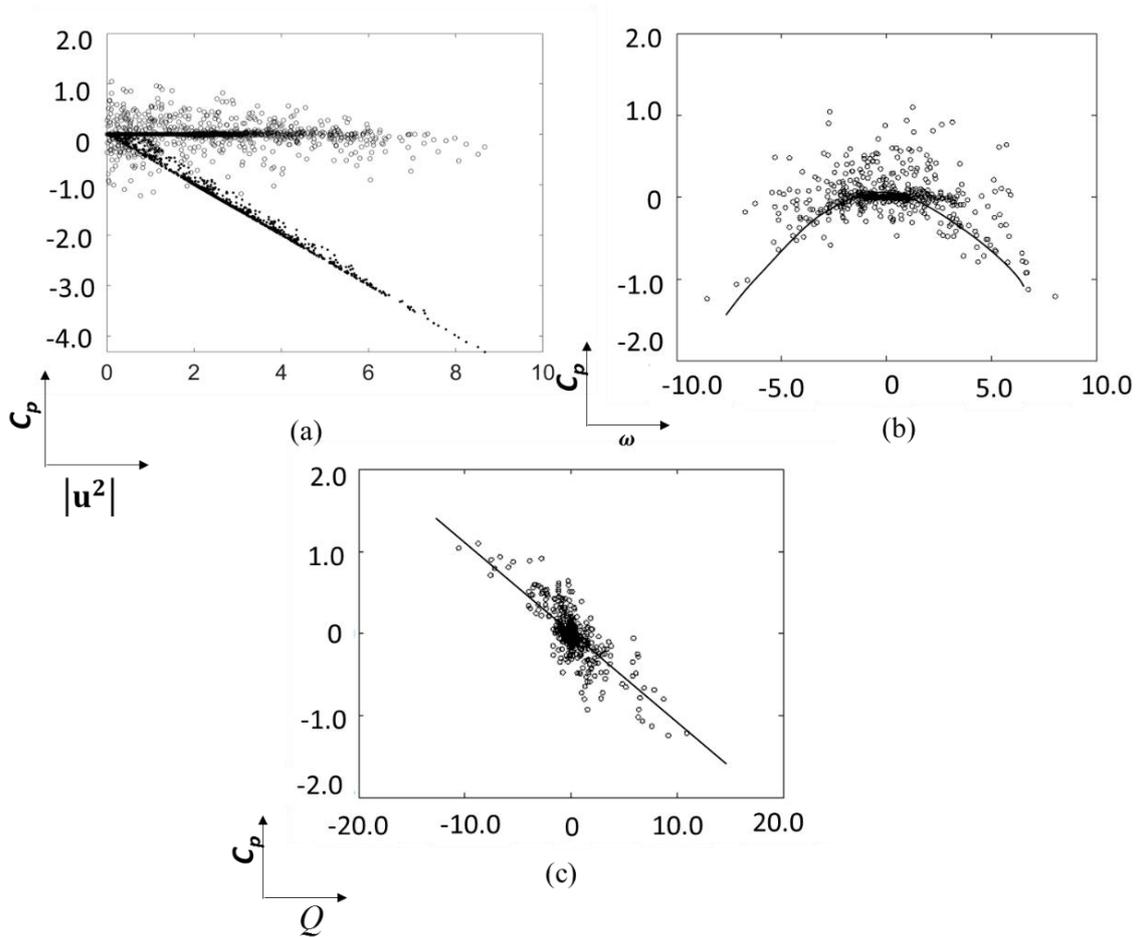
Fig. 3.16 (a) Scatter plot of pressure evaluated by present method and Bernoulli's equation (b) Scatter plot between pressure and vorticity (c) scatter plot between pressure and Q value
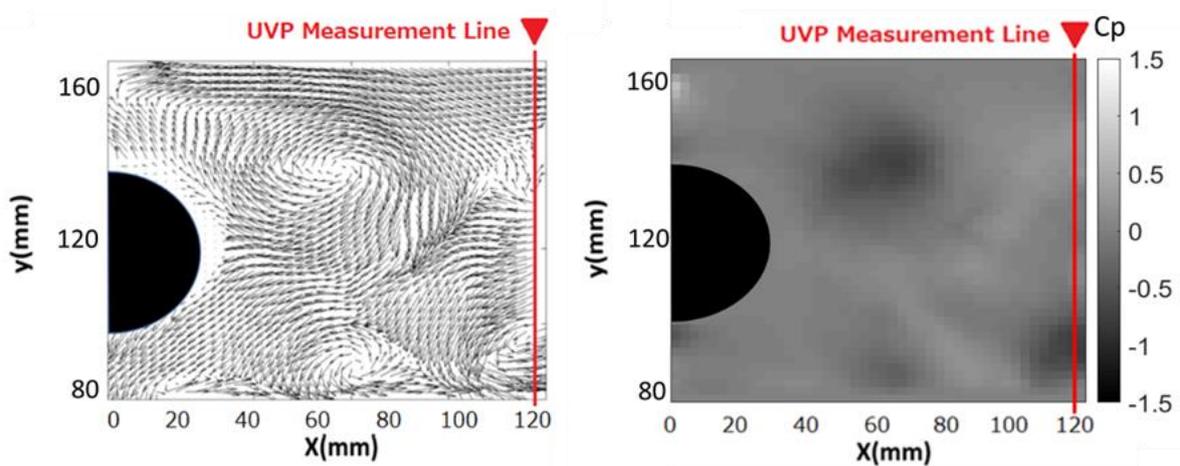
Fig. 3.17 Velocity distribution measured by PIV and pressure estimated from Navier-Stokes method Eq. 3.12, 3.13

Here vertical red lines show the measurement line of UVP. In this figure the staggered arrangement of vortices can be confirmed. This agrees with measurements by (Azmi and Zhou 2018) at Re = 1000 where the formation length is shorter than 3D hence the staggered arrangements can be observed after the formation length. This was useful in order to avoid three-dimensionality of flow. These vortices are passing by the UVP measurement line at x/D=3. The minimum value of pressure at x/D=3 is between -1 to -1.5, this agrees with estimated pressure magnitude by UVP, Fig. 3.13.

3.8 Algorithm UPP (Ultrasonic pressure profiler)

The overall algorithm of pressure estimation from UVP velocity data is shown in Fig. 3.18. The algorithm follows six steps:

1. A component of velocity measurement by UVP.

2. Filtering by FFT and POD

3. Apply Taylor frozen hypothesis and convert velocity from t-y plane to x-y plane

4. Estimate unknown component of velocity by using equation of continuity

5. Estimate pressure gradient from Navier-Stokes equation

6. Integrate pressure gradient and obtain pressure by iterative scheme by attaining least square error < 0.0001
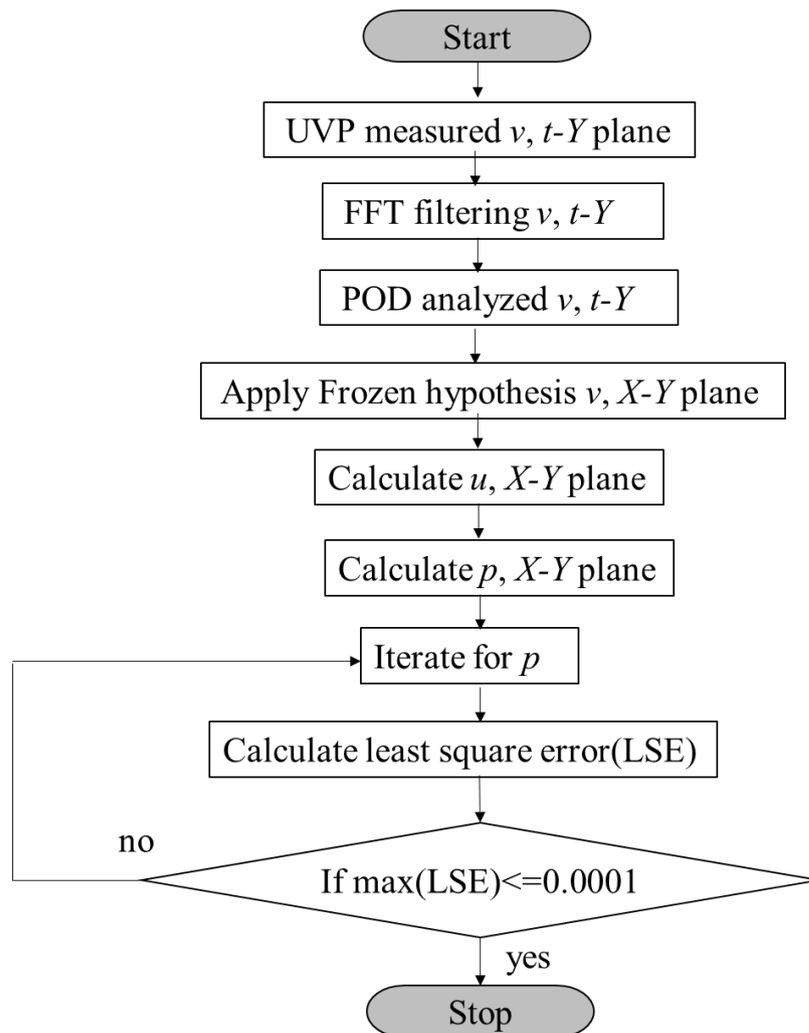
Fig. 3.18 Pressure estimation based on UVP measurement in opaque flows

3.9 Pressure estimation in milk

The pressure estimation algorithm (Fig. 3.19) was applied to study vortex shedding downstream of cylinder in milk of concentration 0.1wt % of milk powder in water. The skim milk powder was used to make the fluid opaque but still had Newtonian nature. The pressure estimation in milk was mainly performed to demonstrate the capability of present algorithm in opaque system. Experimental arrangements described in Fig. 2.2 was used for velocity measurement in milk. The vortex shedding behind the cylinder was measured by UVP transducer fixed at 3D (three times diameter) distance from cylinder. The y component of velocity was measured by UVP and after filtering by FFT and POD it is used in continuity and Navier-Stokes equations. The

velocity vector and pressure distribution plots are shown in Fig. 3.19 and Fig. 3.20. The Strouhal number of von Kármán vortex street is 0.18. which is lower than water due to higher viscosity and lowering of Re. The vortex pattern in velocity plot is very similar to previous results in water (as expected). In Fig. 3.19 (b) the staggered pattern was observed, and number of small eddies increases as higher POD mode also included in calculation. The alternate regions of pressure minima and maxima are observed in Fig. 3.20 (b). The result of vortex shedding in milk flow experiment was qualitatively very similar to experiment in water which proves its accuracy. The present study reveals that present pressure estimation algorithm can be utilized for pressure measurement in any kind of opaque fluid which has a Newtonian nature.
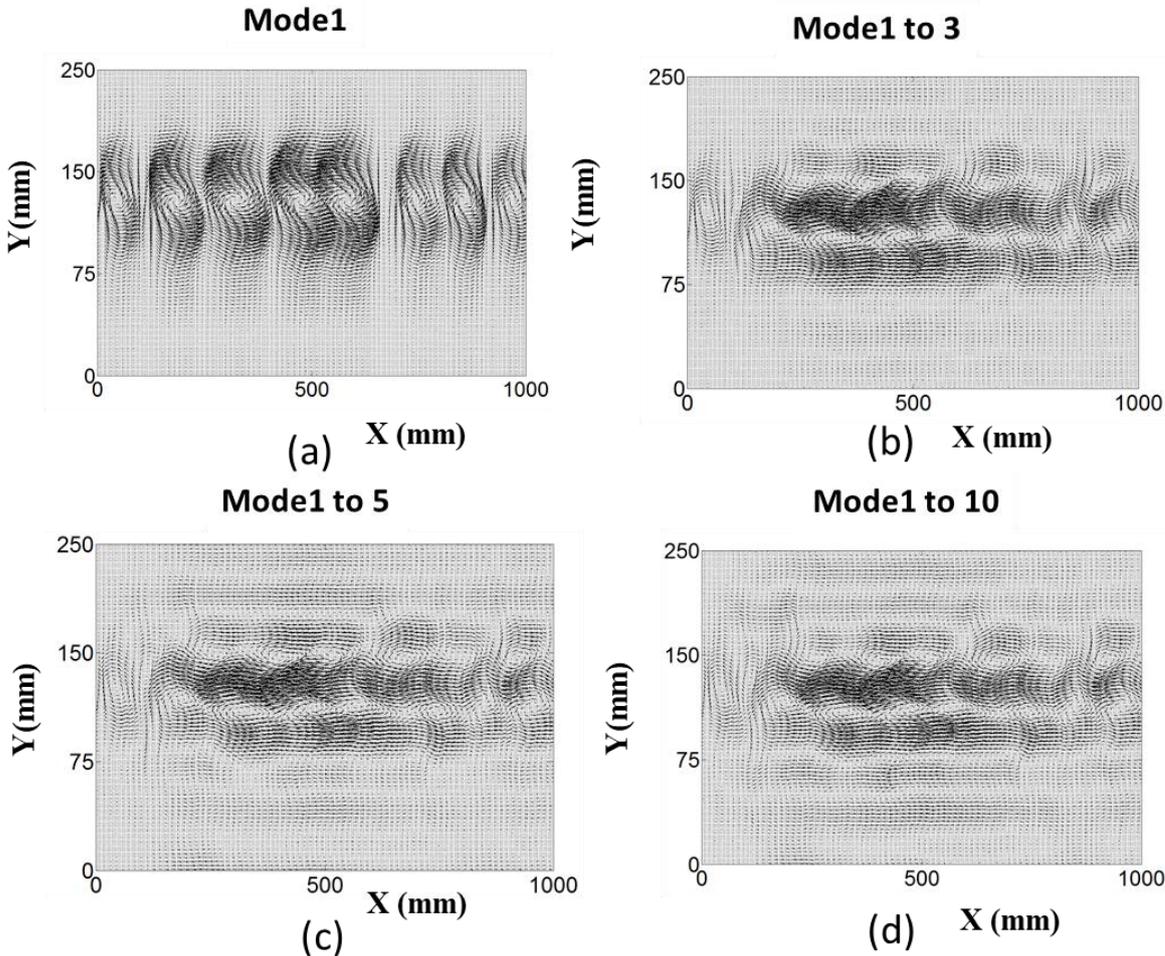
Fig. 3.19 Velocity distribution in milk considering POD mode 1, mode 1 to 3, mode 1 to 5 and mode 1to 10.
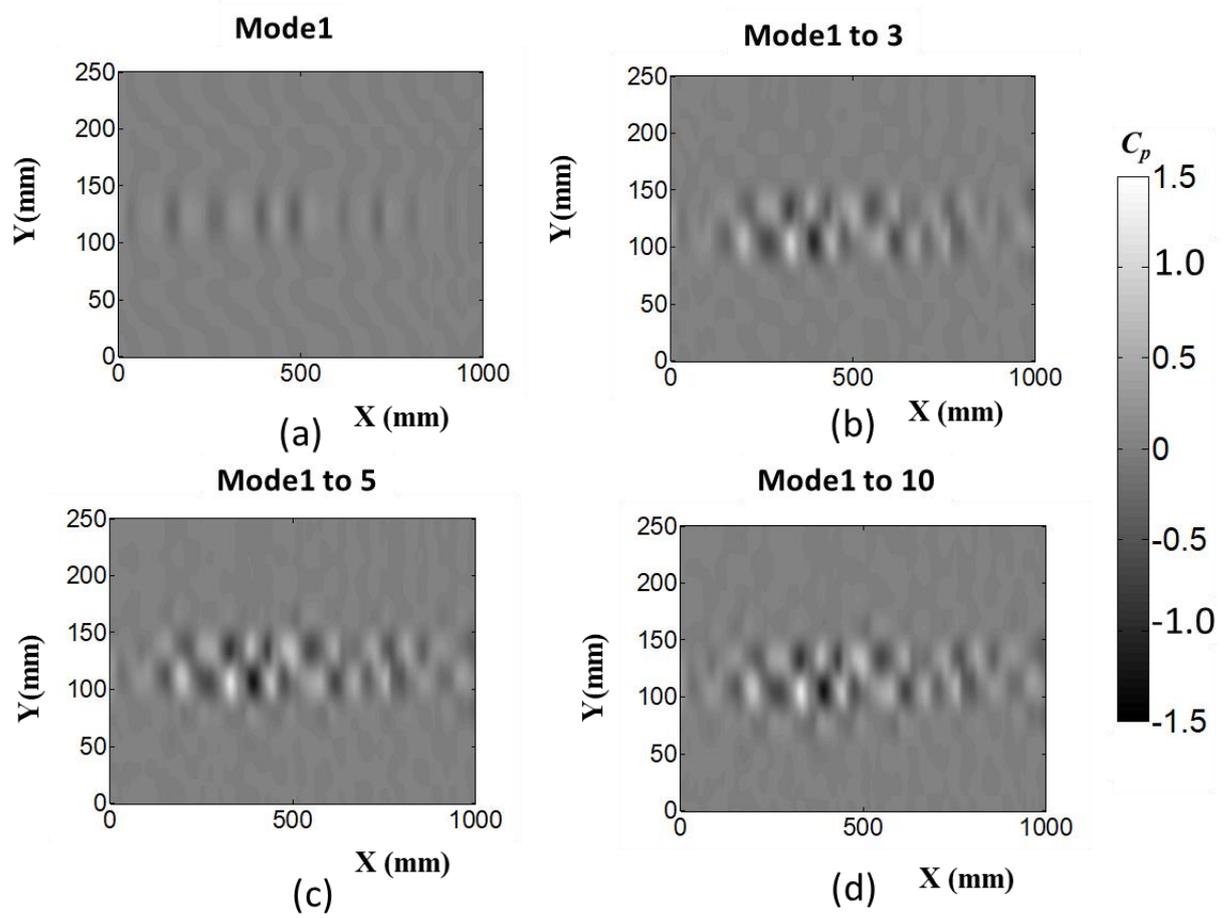
Fig. 3.20 Pressure distribution in milk considering POD mode 1, mode 1 to 3, mode 1 to 5 and mode 1to 10.

Chapter 4

PIV based pressure estimation in transparent shear-thinning fluid

4.1 Introduction

Non-Newtonian fluids are ubiquitous in industrial and biological processes. The rheological properties of these fluids are generally evaluated by 'flow curve' produced by rheometers (Cross 1968). Based on these measurements' rheological models such as power law, Carreau-Yasuda (Carreau 1972), Herschel-Berkley (Tang and Kalyon 2004), Oldroyd-B (1950) etc. are introduced to the analysis of flow. With numerical simulations, these models are useful to improve understanding of complex fluid behavior in many practical flows such as blood flow (Rabby et al. 2013), pipe flows (Yoo et al. 1996), channel flows (Mirzaei Nejad and Javaherdeh 2014), cylinder flow. However, it is still a challenge for computational rheologists to predict the material behavior during fluid structure interaction in complex flow geometries (Walters and Webster 2003)(Trias et al. 2014). In particular, non-Newtonian flow behaviors coupled with vortex dynamics cannot be predicted by simple rheological models. The difficulty originates from potential interaction between pressure and viscosity fields.

Flow of non-Newtonian fluids are also studied by velocity measurement devices, like Laser Doppler Velocimeter (LDV) (Tamano et al. 2010), Ultrasonic Velocity Profiler (UVP) (Tasaka et al. 2015) and Particle Image Velocimetry (PIV) (Tamano et al. 2007). These techniques are helpful to visualize non-Newtonian fluid flow structures quantitatively to assess the influence of fluid rheology. For pressure driven flows, UVP-PD (Ultrasonic Velocity Profiler combined with pressure drop measurement) (Wiklund et al. 2012) (Wiklund and Stading 2008) is an effective tool for in-line rheometry suitable for pipe flows. The pressure measurements at two points and velocity profile measurement are enough for viscosity calculation. For external flow problems, in contrast, two-dimensional (2-D) pressure distribution needs to be introduced along with velocity measurements for coupling with rheological study.

Pressure estimation for Newtonian fluid using PIV is very well studied in last decades and these details were surveyed in van Oudheusden (2013). Navier-Stokes (Eq. 1) or pressure Poisson (Eq. 2) are generally adopted for pressure estimation. For non-Newtonian fluids, Eq. 1 must be replaced with a generalized form of momentum conservation equation to which specific rheological model needs to be introduced. Consequently, Eq. 2 becomes invalid for non-Newtonian fluids.

Details of experimental set up and conditions are discussed in chapter 2. In this chapter, only pressure estimation procedure is discussed.

4.2. Governing equations

PIV data are utilized in governing equations of non-Newtonian flow. In description of governing equations, the following scaling variable are used for providing dimensionless terms: D, diameter of cylinder, for length variables, U for velocity terms, D/U for time and ρU^2 for pressure. Here ρ is density. The dimensionless governing equations in the cartesian coordinates can be written as below:

4.2.1 Momentum conservation equation in *x* and *y* directions

$$\frac{\partial p}{\partial x} = -\left(u \frac{\partial u}{\partial x} + v \frac{\partial u}{\partial y} \right) + \frac{1}{\text{Re}} \left(\frac{\partial \tau_{xx}}{\partial x} + \frac{\partial \tau_{yx}}{\partial y} \right) \tag{4.1}$$

$$\frac{\partial p}{\partial y} = -\left(u \frac{\partial v}{\partial x} + v \frac{\partial v}{\partial y} \right) + \frac{1}{\text{Re}} \left(\frac{\partial \tau_{yx}}{\partial x} + \frac{\partial \tau_{yy}}{\partial y} \right) \tag{4.2}$$

Here *Re* stands for Reynolds number for non-Newtonian fluid.

Relation between shear stress and strain rate is given by

$$\tau_{i,j} = \eta \gamma_{i,j} \quad \rightarrow \quad \begin{pmatrix} \tau_{xx} & \tau_{xy} \\ \tau_{yx} & \tau_{yy} \end{pmatrix} = \eta \begin{pmatrix} \gamma_{xx} & \gamma_{xy} \\ \gamma_{yx} & \gamma_{yy} \end{pmatrix} \tag{4.3}$$

where, i, j are indices in x, y direction. η is non-dimensional viscosity and $\gamma_{i,j}$ is non-dimensional strain rate tensor, which is computed by measured velocity field as:

$$\gamma_{i,j} = \begin{pmatrix} \gamma_{xx} & \gamma_{xy} \\ \gamma_{yx} & \gamma_{yy} \end{pmatrix} = \frac{1}{2} \begin{pmatrix} 2\dfrac{\partial u}{\partial x} & \dfrac{\partial v}{\partial x} + \dfrac{\partial u}{\partial y} \\ \dfrac{\partial v}{\partial x} + \dfrac{\partial u}{\partial y} & 2\dfrac{\partial v}{\partial y} \end{pmatrix} \tag{4.4}$$

By substitution of Eqs. 4.3 and (4.4) into Eqs. 4.1 and 4.2, we can get

$$\frac{\partial p}{\partial x} = -\frac{\partial u}{\partial t} - \left(u\frac{\partial u}{\partial x} + v\frac{\partial u}{\partial y} \right) + \frac{\eta}{\text{Re}}\left(\frac{\partial^2 u}{\partial x^2} + \frac{\partial^2 u}{\partial y^2} \right) + \frac{2}{\text{Re}}\left(\gamma_{xx}\frac{\partial \eta}{\partial x} + \gamma_{yx}\frac{\partial \eta}{\partial y} \right), \tag{4.5}$$

$$\frac{\partial p}{\partial y} = -\frac{\partial v}{\partial t} - \left(u\frac{\partial v}{\partial x} + v\frac{\partial v}{\partial y} \right) + \frac{\eta}{\text{Re}}\left(\frac{\partial^2 v}{\partial x^2} + \frac{\partial^2 v}{\partial y^2} \right) + \frac{2}{\text{Re}}\left(\gamma_{xy}\frac{\partial \eta}{\partial x} + \gamma_{yy}\frac{\partial \eta}{\partial y} \right). \tag{4.6}$$

In Eq.4.5 and 4.6, velocity and strain rate in the r.h.s. of Eqs. 4.5 and 4.6 can be provided by PIV measurement but for pressure gradient estimation it is not sufficient. The information of viscosity distribution needs to be introduced by rheological model.

4.2.2   Rheological models

Many rheological models are available in literature (Herschel-Bulkley, Casson, Carreau-Yasuda, Power law, Cross model) to study shear thinning fluids. Two kinds of shear-thinning models were chosen for present study, power law model and Carreau-Yasuda model. Power law model has been extensively used in numerical simulation in literature to study vortex flow of cylinder (Bharti et al. 2007) (Dhiman et al. 2006). Carreau- Yasuda model is more accurate than power law model for flow with wide range of strain rate (Rao 2014).

4.2.2.1 Power law model:

The viscosity of power law fluids can be written as:

$$\mu_p = k\gamma^{n-1} \tag{4.7}$$

Here μ_p is dimensional viscosity, k is consistency index and n is power law index. The viscosity of power law fluids is non-dimensionalized as:

$$\eta = \frac{\mu}{\mu_p} \tag{4.8}$$

Then, non-dimensional viscosity can be derived as

$$\eta = \left(\frac{II_{2D}}{2}\right)^{(n-1)/2} \tag{4.9}$$

where II_{2D} is the second invariant of strain rate tensor (Bird et al. 2007) can be written as:

$$II_{2D} = \sum_i \sum_j \gamma_{ij} \cdot \gamma_{ji} = \gamma_{xx}^2 + \gamma_{xy}^2 + \gamma_{yx}^2 + \gamma_{yy}^2 \tag{4.10}$$

Re for power law fluid flows can be defined as:

$$Re_P = \frac{\rho D U}{\mu} = \frac{\rho D^n U^{2-n}}{k} \tag{4.11}$$

4.2.2.2 Carreau-Yasuda model

In Carreau-Yasuda model the non-dimensional viscosity varies with II_{2D} as

$$\eta = \frac{\mu_\infty}{\mu_0} + \left(1 - \frac{\mu_\infty}{\mu_0}\right)\left[1 + \left(\lambda^a II_{2D}\right)^{m-1/a}\right], \tag{4.12}$$

Here λ, a and m are the Carreau-Yasuda parameters, μ_0 and μ_∞ represent the viscosity at zero and infinite shear rate, respectively. For fluid flows obeying Carreau-Yasuda model, Re can be defined as

$$Re = \frac{\rho D U}{\mu_0}$$

(4.13)

The parameters obtained from rheometer experiments performed at $\varepsilon_{yx} = 1$ to 4000 s^{-1} are given in Table 1 and Table 2 (Coelho and Pinho 2004) for Carreau-Yasuda and power law model respectively.

Table 4. 1 Rheological parameters for Carreau-Yasuda model

Solution	μ_0 [Pas]	μ_∞ [Pas]	λ	a	m
0.1% CMC	0.01367	0.0008	0.01317	0.6671	0.5864

Table 4.2 Rheological parameters for power-law model

Solution	N	k
0.1% CMC	0.724	0.032

4.3 Pressure estimation algorithm

The present algorithm couples the PIV measurements, momentum conservation equations, and rheological models. The procedure can be summarized in the following four steps:

i) Perform experiments to measure the velocity data by PIV and apply suitable filtering to remove noise in the experimental data.

ii) Substitute the measured velocity data into rheological models: power law model (Eq. 4.8) and Carreau-Yasuda model (Eq. 4.12) to evaluate viscosity.

iii)The viscosity and velocity data obtained by step i) and ii), are further substituted to

38

momentum equations (Eqs. 4.5 and 4.6) to calculate the instantaneous pressure gradients in x and y direction.

iv) Integrate the pressure gradients in space in iterative manner to obtain the pressure at an arbitrary point by satisfying following equations:

$$p_{i,j} = p_{i\pm1,j} \mp \left(\frac{\partial p}{\partial x}\right)_{i\pm\frac{1}{2},j} \Delta x, \quad p_{i,j} = p_{i,j\pm1} \mp \left(\frac{\partial p}{\partial y}\right)_{i,j\pm\frac{1}{2}} \Delta y$$

(4.14)

The maximum square error (MSE) of pressure discrepancy was calculated for Eq. 4.14 at each iteration step to monitor numerical convergence. As MSE falls below 10^{-4} (dimensionless), the pressure is accepted as final solution. The flow chart of algorithm is shown in Fig. 4.1.
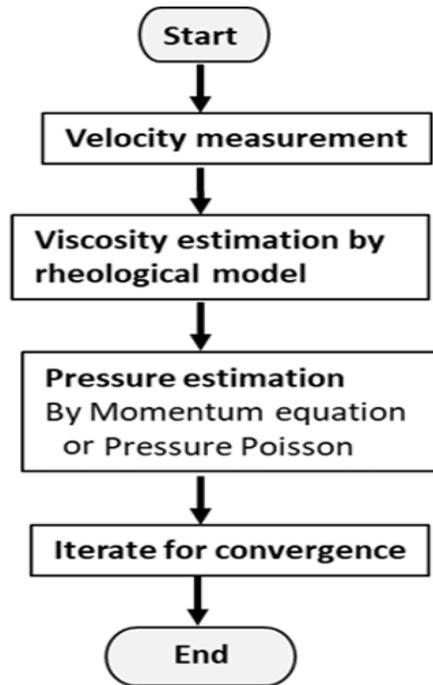
Fig. 4.1. Algorithm for pressure estimation in shear thinning fluid based on PIV

4.4 Algorithm implementation in steady flow

The algorithm was applied to PIV measurement performed at U=0.01 m/s, Re=30 in towing tank filled with aqueous solution of CMC. At t=12 s from start of towing at t=0 s, twin vortices attained the maximum size and became steady (Tang and Aubry 1997) as shown in Fig. 4.2 (a). The kinetic energy distribution clearly separated the boundaries between free stream region and

separation region Fig. 4.2 (b). In the vorticity plot (Fig. 4.2 (c)), shear layer region and vortex cores can be easily distinguished. In reverse flow region, blue region indicates the anticlockwise rotating vortex and yellow region represent clockwise rotation of vortex. In Fig. 4.2 (d) the high shear rate region appeared in shear layer and decreased downward in vortex region. In the free stream region, it reduces to almost zero.
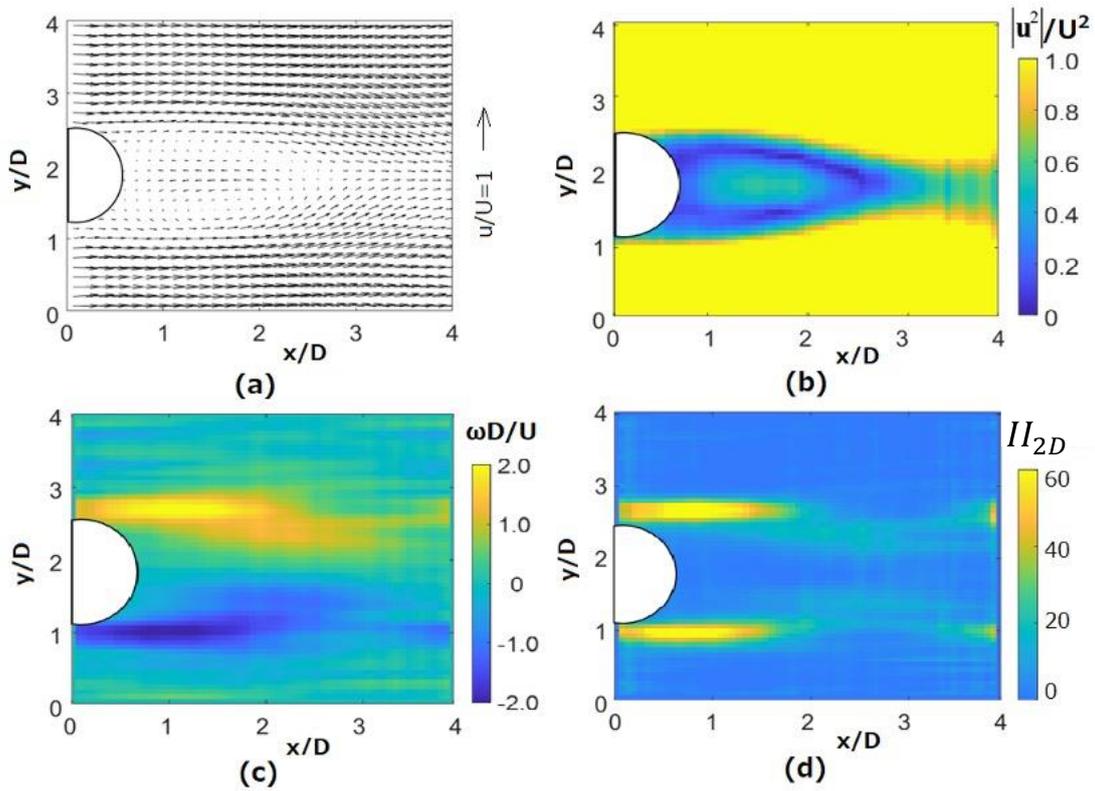
Fig. 4.2 Distribution of velocity vectors on measurement plane at *Re* = 30, *t* =12 s (a) PIV velocity vectors, (b) kinetic energy, (c) vorticity, and (d) strain rate

4.4.1 Viscosity distribution

The velocity data are substituted in Eq. 4.10 to evaluate II_{2D}. This procedure is described in step ii) described in section 4.3. The viscosity distributions at t=12 sec were evaluated using Carreau-Yasuda Fig. 4.3(a, b) and power law model Fig. 4.3 (c, d). The viscosity distribution by power law model is qualitatively similar to that by Carreau-Yasuda model. The viscosity was lower in wake region due to higher strain rate in that region. This result demonstrates shear

thinning property of the CMC aqueous solution. However, for free stream region where strain rates were comparatively smaller, the power law model overpredicted the viscosity with large fluctuations in space, this also proves that power law model is not suitable for viscosity estimation in region with low strain rate.
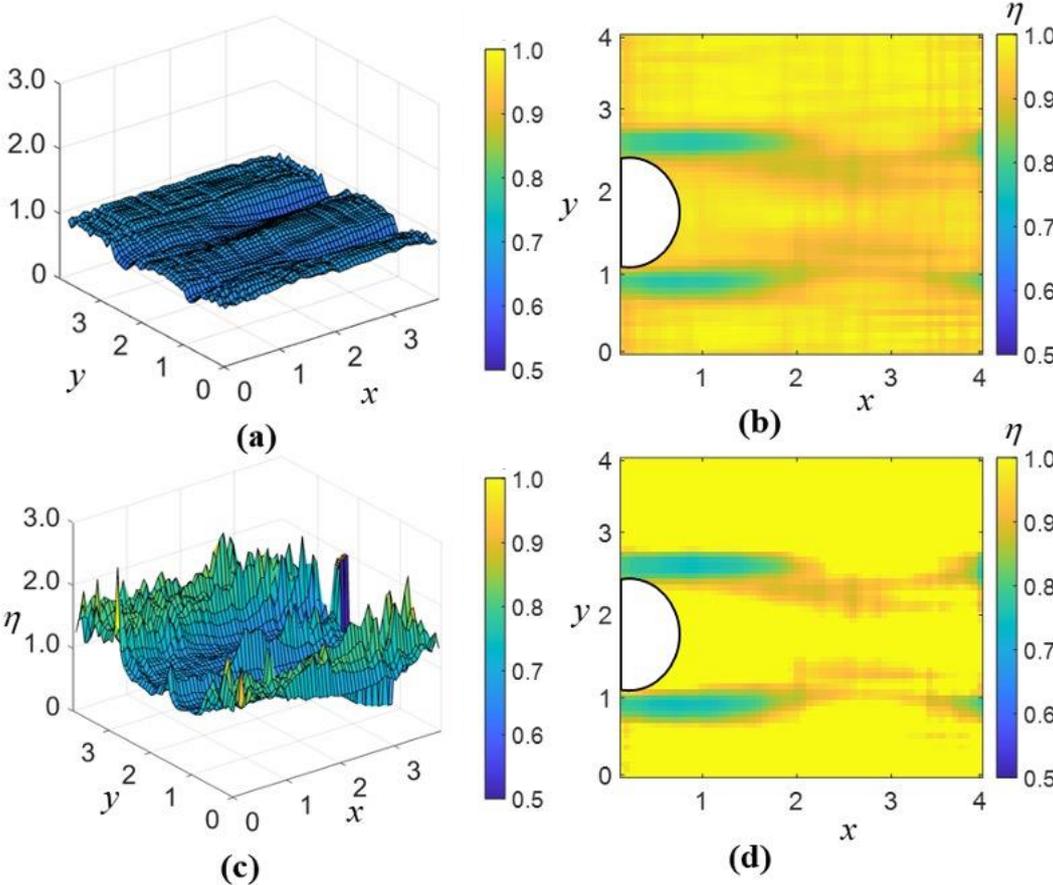
Fig. 4.3 Viscosity distribution in entire computational domain at *Re* = 30, *t* =12 s, estimated by (a, b) Carreau-Yasuda model and (c, d) power law model

4.4.2   Pressure distribution

For *Re* in the range 5<*Re*<40 the flow of fluid is two-dimensional and steady (Williamson 1996). The pressure distributions were evaluated by substituting velocity and viscosity using Power law (Fig. 4.4 (a)) and Carreau-Yasuda model Fig. 4.4 (b) in momentum equations. Both the pressure plots were smooth and accurately reproduced the low-pressure region in cores of vortices. Both the models work effectively well in reconstructing the pressure field. In Fig. 4.4

(c) and (d) momentum equation was solved by assuming $\eta=0$ and $\eta=1$ respectively. The pressure distributions were almost same as the pressure evaluated by Carreau-Yasuda and Power law model. This indicates that the contribution of diffusion term in the momentum equation is very small. However as η is increased from 5 to 10 the effect of error in pressure increases due to incorrect rheological information.
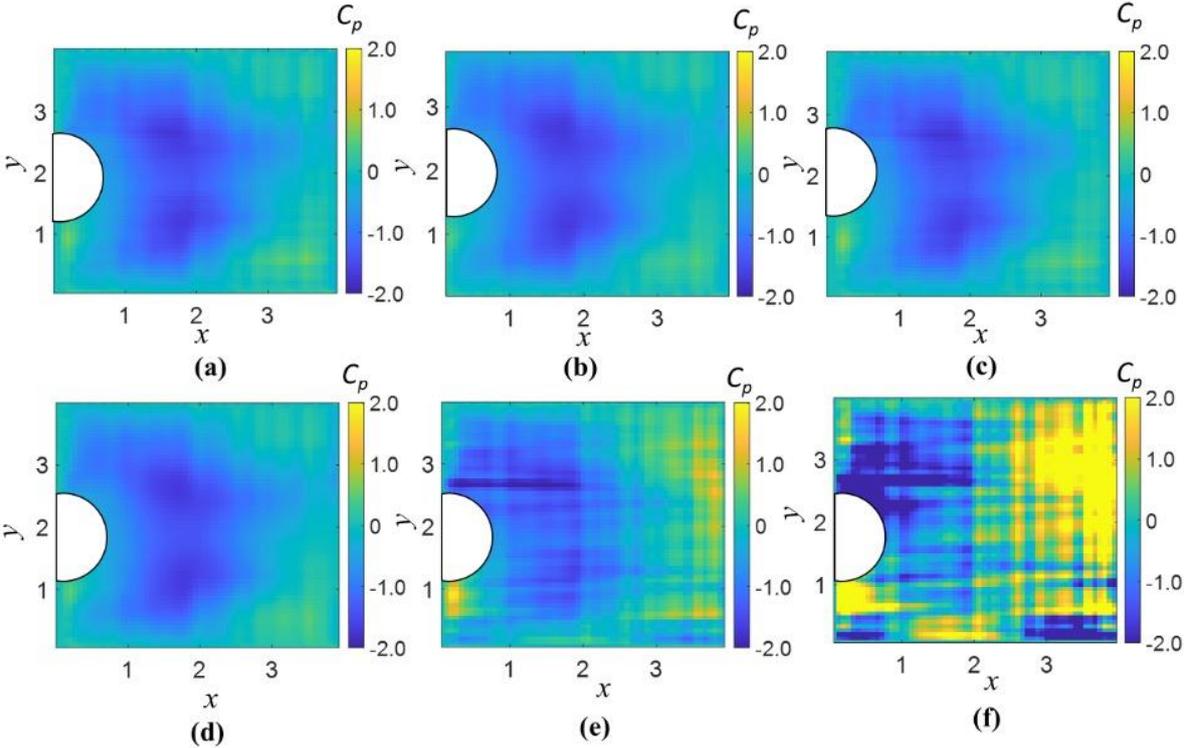
Fig. 4.4 Pressure distribution plots at $Re = 30, t =12$ s, using (a) Power law model (b) Carreau Yasuda model (c) $\eta=0$ (d) $\eta=1$ (e) $\eta=5$ (f) $\eta=10$

4.4.3   Relation between material property to pressure and viscosity

Even though vortex flow over cylinder is a widely researched topic, the relation between viscosity and pressure in von-Kármán vortex street is rarely mentioned in literature because, in incompressible flows of Newtonian fluids, viscosity is invariant with pressure. Moreover, there is no existing technique to measure 2D pressure fields of non-Newtonian fluids. Thus, it is not possible to introduce a counter technique to validate the results directly. In Figs. 4.3 and 4.4 (a)

the obtained viscosity and the pressure range were physically valid. A quantitative assessment of relationship between viscosity and other relevant flow variables was performed by with cross-correlation analysis. Two scalar flow variables were chosen for this purpose, one is pressure which represents the dynamic property of flow and the other is enstrophy ($|\omega|^2$) which depends on kinematic variable vorticity. Here, an attempt is made to understand the relationship of viscosity with pressure. The viscosity variation with pressure and enstrophy in scatter plots are shown in Fig. 4.5 (a), (b). The corresponding correlation coefficients (*Cc*) are presented at the bottom of respective figures.

$$Cc = \frac{1}{N-1} \sum_{i=1}^{N} \left(\frac{\overline{A_i - \zeta_a}}{\sigma_a} \right) \left(\frac{B_i - \zeta_b}{\sigma_b} \right)$$

(4.15)

Here *Cc* represents the linear dependence of two variable *A* and *B*, having *N* observations. ζ_a and σ_a are mean and standard deviation corresponding to variable *A* and ζ_b and σ_b are mean and standard deviation corresponding to variable *B*.

It was found that η is negatively correlated with enstrophy and positively correlated with pressure. Negative correlation of enstrophy with viscosity indicated that as vorticity increases in the flow the viscosity decreases so for shear thinning fluid vorticity is sustained for longer time which indicates the shear thinning property works against the momentum diffusion. On the other hand, *Cp* does not depend on η directly, but still has weak positive correlation
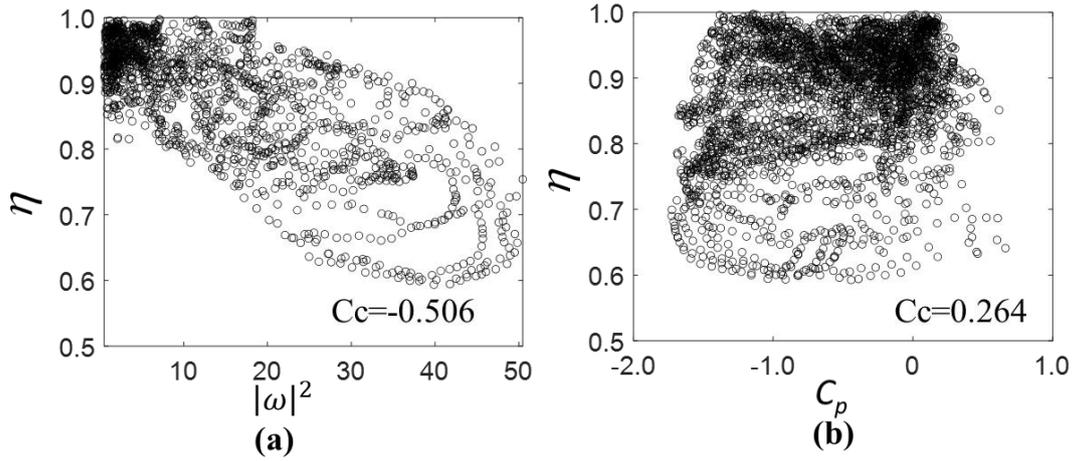
Fig.

4.5 Correlation plots at time t=12, between (a) viscosity (η) vs enstrophy (b)viscosity (η) and pressure (C_p)

4.5 Algorithm implementation in unsteady flow

The algorithm shown in Fig. 4.1 is applied for *Re*=87 to estimate pressure distribution.

4.5.1 Filtering: POD-based noise reduction of measured velocity data

Snapshot proper orthogonal decomposition (POD) method for the noise reduction was employed in two consecutive images (Sirovich 1987b) (Meyer et al. 2007). The measurements were performed at *U*=0.03m/s in aqueous solution of CMC of concentration of wt % of 0.1, in experimental facility shown in Fig. 2.2. The PIV post processing was performed by PIVLAB as described in section 2.2. The velocity vectors with streamlines of data collected at t=12 sec from the start of towing (t = 0 s) is shown in Fig. 4.6. At this instance, a symmetric pair of vortices was observed downstream. For present experimental data (Fig. 4.6(a)), the first 20 POD modes contain the 99.9% of total kinetic energy as shown in Fig. 4.6(b). Here, first mode already contains the 95.9% of the total kinetic energy and substantial drop can be seen in successive higher modes.
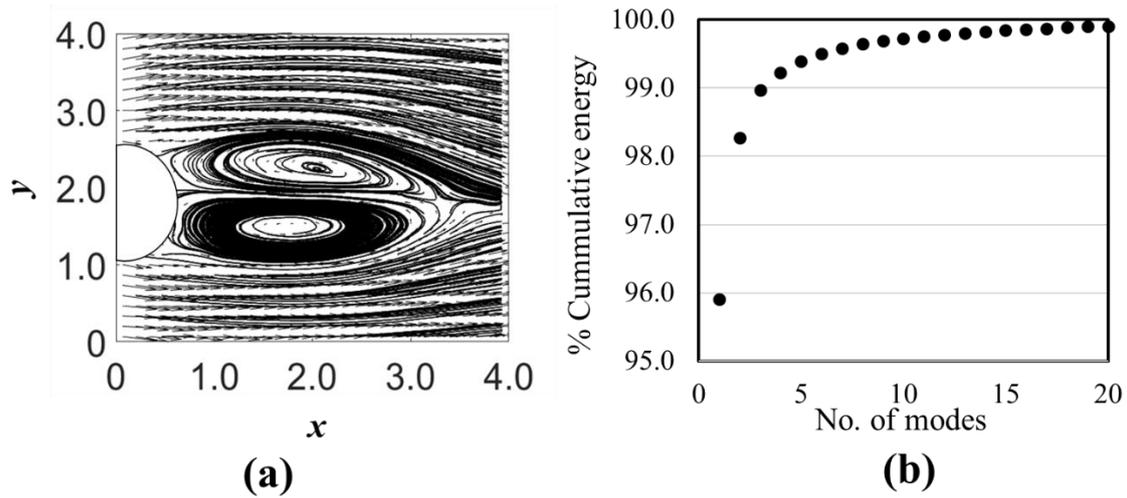
Fig. 4.6 (a) Distribution of instantaneous velocity and streamlines on measurement plane at $U = 0.03$m/s, $t =12$ sec (b) energy content in first 10 POD modes

At t=12 sec, unfiltered x and y components of velocity along with filtered data by POD, considering POD mode 1, POD mode 1 to 3 and POD mode 1 to 20 are shown in Fig. 4.7 (a) and (b). Along with that, distribution of shear strain rate, (Eq. 4.10) is shown in Fig. 4.7(c). As higher number of POD modes are considered smaller eddies also appeared with dominant structures in the velocity data and strain rate. The propagation of error could be severe as higher POD modes are considered. The numerical procedure and the experimental noise both need to be handled carefully. Generally, in CFD problems the derivative terms are discretized with higher order accurate differencing schemes to reduce truncation error. However, derivative calculation with experimental data with the higher order accurate scheme could bring much more severe errors due to experimental noise. This makes the present problem very challenging because it is required to consider noises combined from experimental and numerical procedures in solving non-linear and higher order derivative terms involved in non-Newtonian momentum conservation equations (Eqs. 4.5 and 4.6).
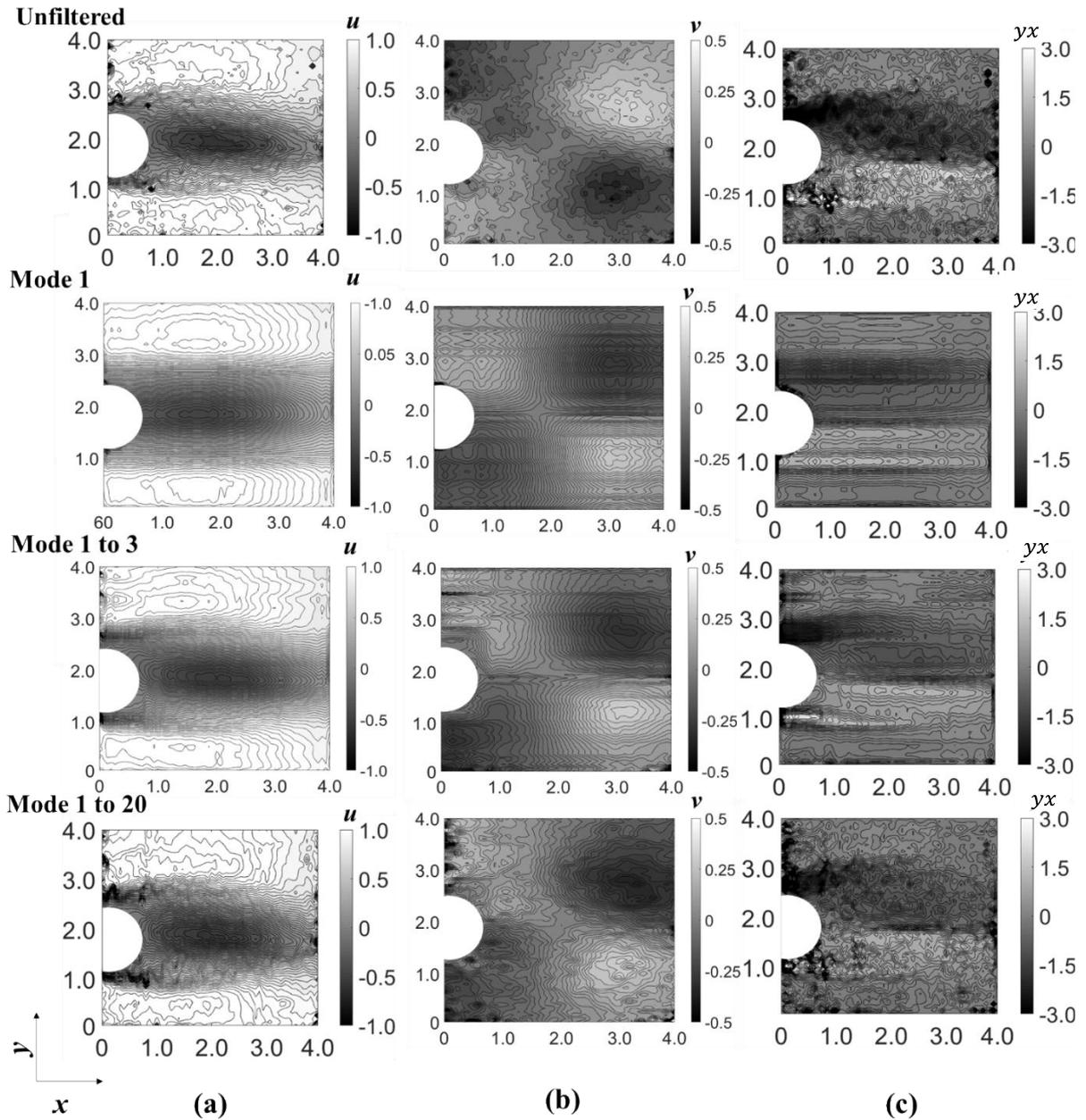
Fig. 4.7 Distributions of instantaneous velocity components at *t*=12 s, (a) *u* (b) *v*, and (c) strain rate, both unfiltered and filtered data (after applying POD considering only mode 1, mode 1 to 3 and mode 1 to 20).

4.5.2 Viscosity and pressure distributions

The velocity data is reconstructed by considering POD modes 1 to 3 and used in the calculation of II_{2D} (Eq. (4.10)). The viscosity distribution at *t*=12 sec was calculated using (a) Carreau-Yasuda and (b) power law model and shown in Fig. 4.8. The viscosity distribution by power

law model was qualitatively similar to that by Carreau-Yasuda model. The viscosity is lower in wake region due to higher strain rate in that region. This result demonstrates shear thinning property of the CMC aqueous solution. However, for free stream region where strain rates are comparatively smaller, the power law model predicted higher viscosity. This behavior of Power law model is consistent with the steady case.
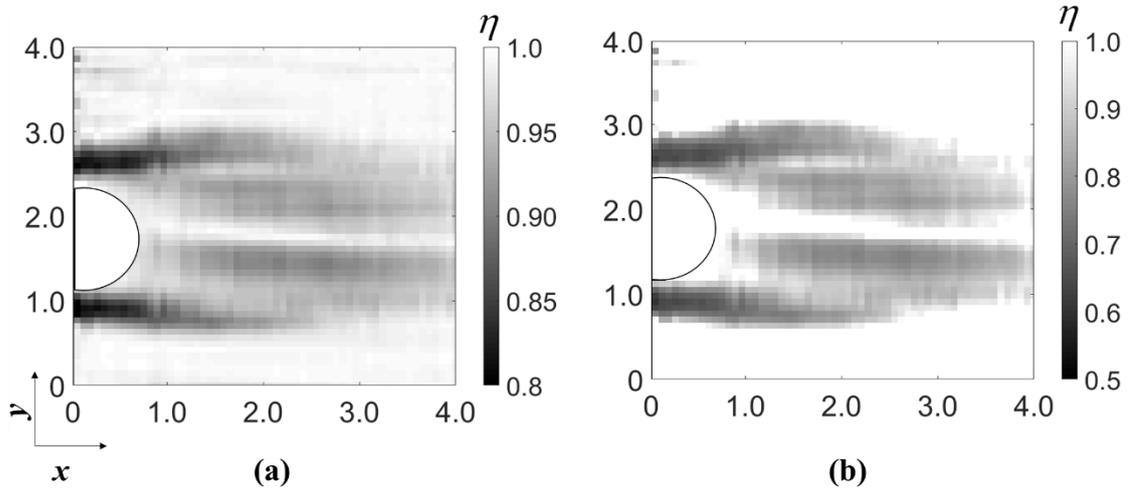
Fig. 4.8 Viscosity distribution in entire computational domain at $U = 0.03$m/s, $t = 12$ s, estimated by (a) Carreau-Yasuda model and (b) power law model

The pressure ($C_p = p/\rho U^2$) distributions are obtained by utilizing filtered and unfiltered velocity and corresponding viscosity (using Carreau-Yasuda model) in momentum equations and are shown in Fig. 4.9. Figure 4.9(a) shows the pressure distribution evaluated by unfiltered velocity data. The pressure in wake region is higher than other regions which is unrealistic. Using median filtered velocity data in momentum equation, the pressure distribution is shown in Fig. 4.9(b). With this approach, low-pressure region in the wake was observed although the presence of vortices is still not clear. On the other hand, in Fig. 4.9(c) pressure distributions by POD filtered data (mode 1 to 3) and POD mode 1 to 20 (Fig. 4.9(d)) are more realistic. The low-pressure region is formed in the wake, clearly indicating the presence of a pair of vortices behind the cylinder. Another concern is the three-dimensionality close to cylinder. Although, error due to 2D assumption of 3D flow is limited to 5% for pressure in wake of a cylinder up to Re=1600

(McClure and Yarusevych 2017b). This is attributed to the understanding that the energy containing dynamic part of vortex shedding flow is mostly 2D while vortex filaments are distributed in 3D. In addition, POD analysis included the lower modes containing high energy content of flow.
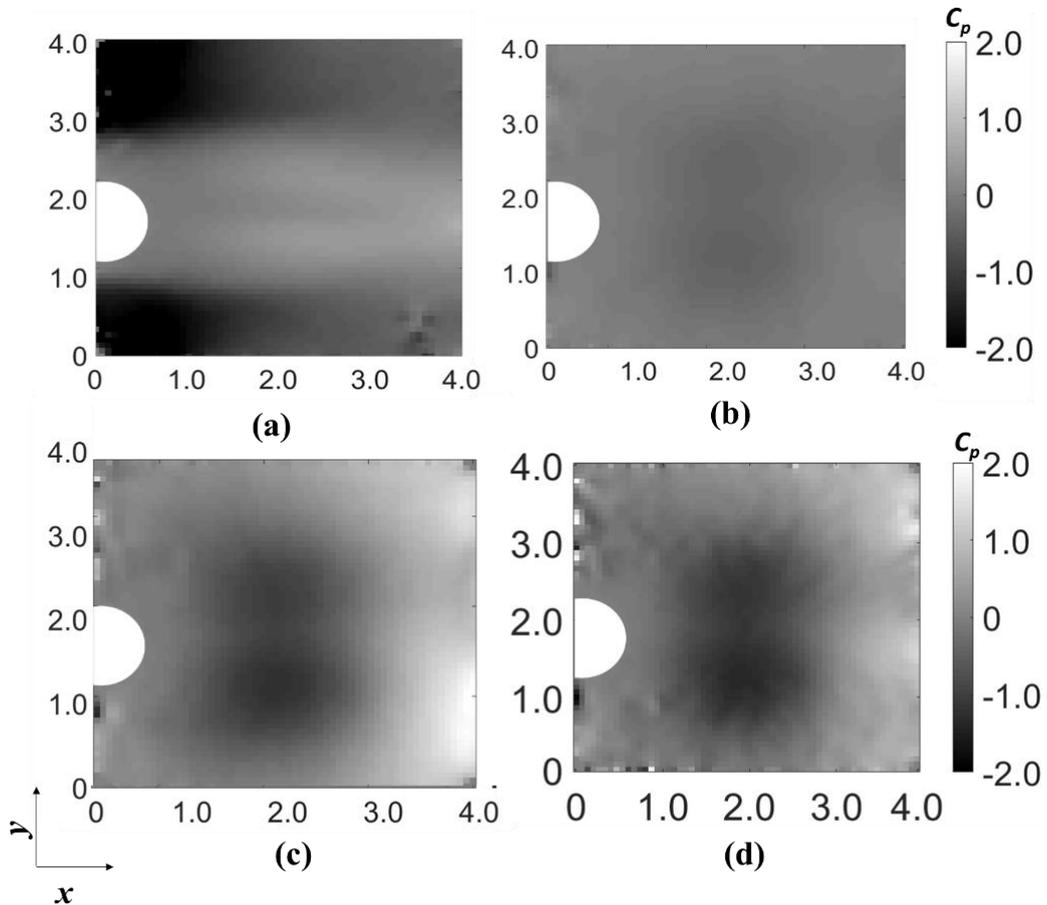
Fig. 4.9 Pressure ($C_p = p/\rho U^2$) distribution plots using (a) unfiltered (b) Median filtered (c) POD mode 1 to 3 (d) POD mode 1 to 20 filtered velocity data at $U = 0.03$ m/s, $t = 12$ sec

4.5.3 Performance of Algorithm in Unsteady Process

To evaluate the performance of pressure estimation algorithm, the measured data were analyzed at various time instances. The distribution of pressure and viscosity at these time instances are shown in Fig. 4.10. The velocity data is extracted at three stages of vortices development. At $t=0.06$ s, in wake, the shear layer vortices were developing and are exactly symmetrical with

respect to the center of cylinder. Symmetric viscosity and low-pressure regions were obtained downstream in the wake Fig. 4.10 (a). At t=10 s, the vortices are developed but still attached with shear layers. The corresponding viscosity and low-pressure region formed accordingly in wake, Fig. 4.10 (b). At t=22 s, vortices were separated from shear layer. The viscosity distribution was formed as expected, but the low-pressure region was not reconstructed accurately which might be due to unsteady term omission in pressure calculation Fig. 4.10 (c). For pressure estimation, temporal terms in Eq. 4.5 and 4.6 can be omitted if advection terms dominate over temporal term. At t=3.3 sec, the temporal term and advection terms are calculated for PIV measured data considering POD mode 1 to 20 as shown in Fig. 4.11. It is found that the magnitude of temporal term is at least 10 times smaller than the advection term. It was observed that the distribution of temporal term is not smooth. Thus, inclusion of temporal term makes the solution unrealistic due to large error propagation during integration procedure. The time derivative terms were also omitted in the study by (Imaichi and Ohmi 1983). They mentioned that during development of twin vortices the error in neglecting temporal term is very less because flow develops very slowly in time. However, as it was found that at t=22 sec the vortices separated and migrated downstream and flow changes much faster. The present algorithm could not reconstruct the pressure field after vortices detached from shear layer and migrated downstream, so the omission of temporal term can be justified until vortices are attached to the shear layer which clearly indicates the requirement of much more robust technique to estimate pressure fields.
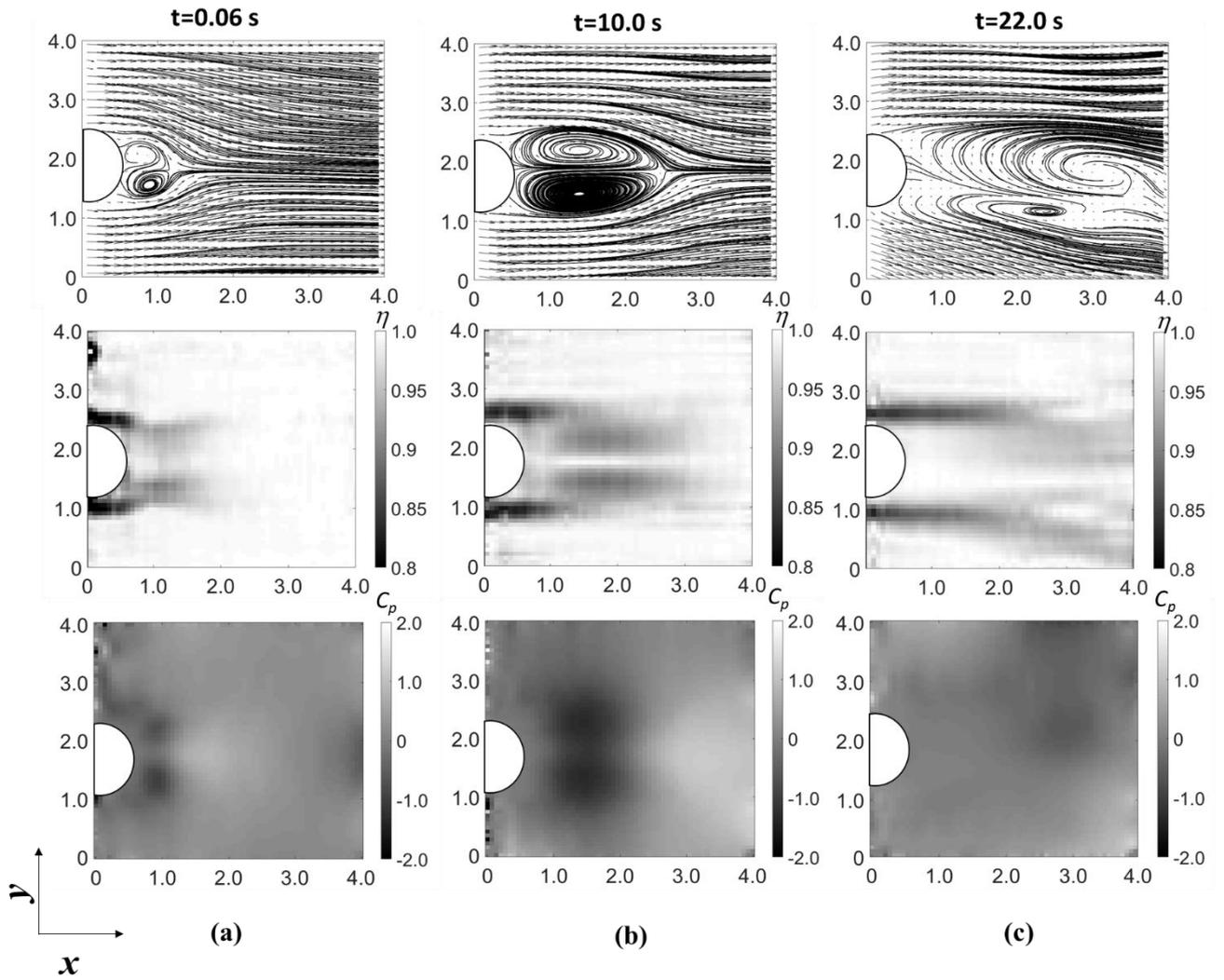
Fig.4.10. Velocity, viscosity and pressure (C_p) distribution for various time instances

(a) t=0.06 s, (b) t=10.0 s and (c) t=22.0 s at U=30mm/s
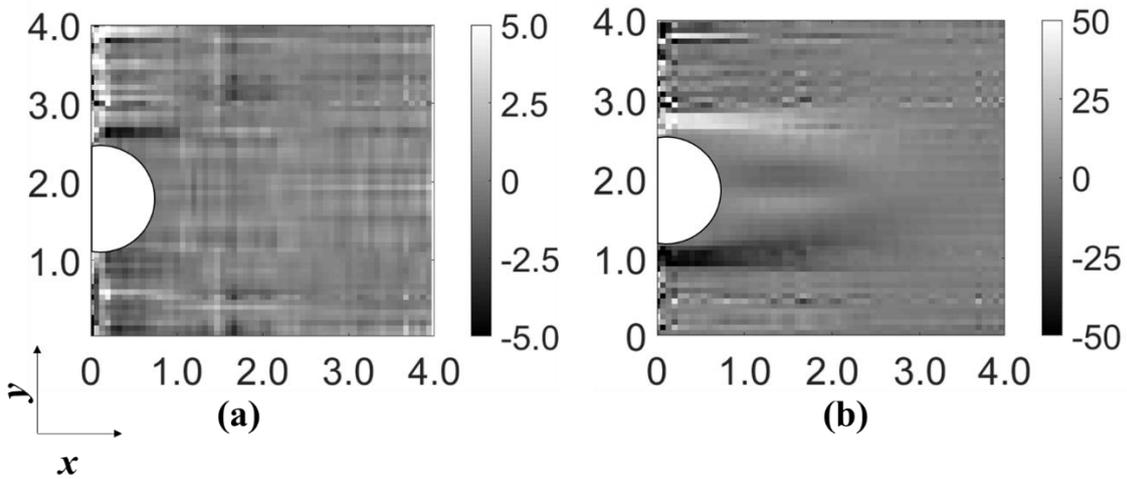
Fig. 4.11 At time t=3.3 sec (a) distribution of temporal term ($\partial u / \partial t$) (b) Sum of advection

and diffusion terms in Eq.8.

4.5.4 Relation Between Material Property to Pressure and Vorticity

An attempt is made to understand the relation between viscosity, pressure and enstrophy in unsteady flow. For several instances, the line integral convolution plots are shown in Fig. 4.12 (a). These plots clearly show the various stages of vortices development. In Fig. 4.12(b, c), the correlation plots are drawn between η and enstrophy ($|\omega|^2$) and η and Cp. The correlation coefficients are given in Fig. 4.12(d). In the present results, η is negatively correlated with enstrophy ($|\omega|^2$) and positively correlated with pressure. Quantitatively, η is more correlated with $|\omega|^2$ than the pressure which confirms that the viscosity is clearly a function of kinematics. At several stages of vortex development, separation and after separation, Cc of η Vs $|\omega|^2$ increases progressively with time. Here, $|\omega|^2$ represents the energy dissipation in the flow (Zhu and Gao 2017). Vortices are strongest in the vicinity of cylinder and dissipate energy as they migrate in the wake so as vortices migrate with time, turbulent kinetic energy dissipation increases (Cottet and Poncet 2002). Negative correlation of $|\omega|^2$ with viscosity indicated successive decrement in η with time. In other words, the wake stabilization increases with time as viscosity drops due to shear thinning property. This means that in the wake, vorticity will increase comparatively higher than Newtonian fluid due to shear thinning property of fluid. On the other hand, positive correlation of η with Cp shows that as time increases the pressure also decreases which signifies that the pressure lowering at vortex core is intensified during vortex development due to shear thinning property of fluid. These physically valid arguments indicate that the results obtained in current work is promising.
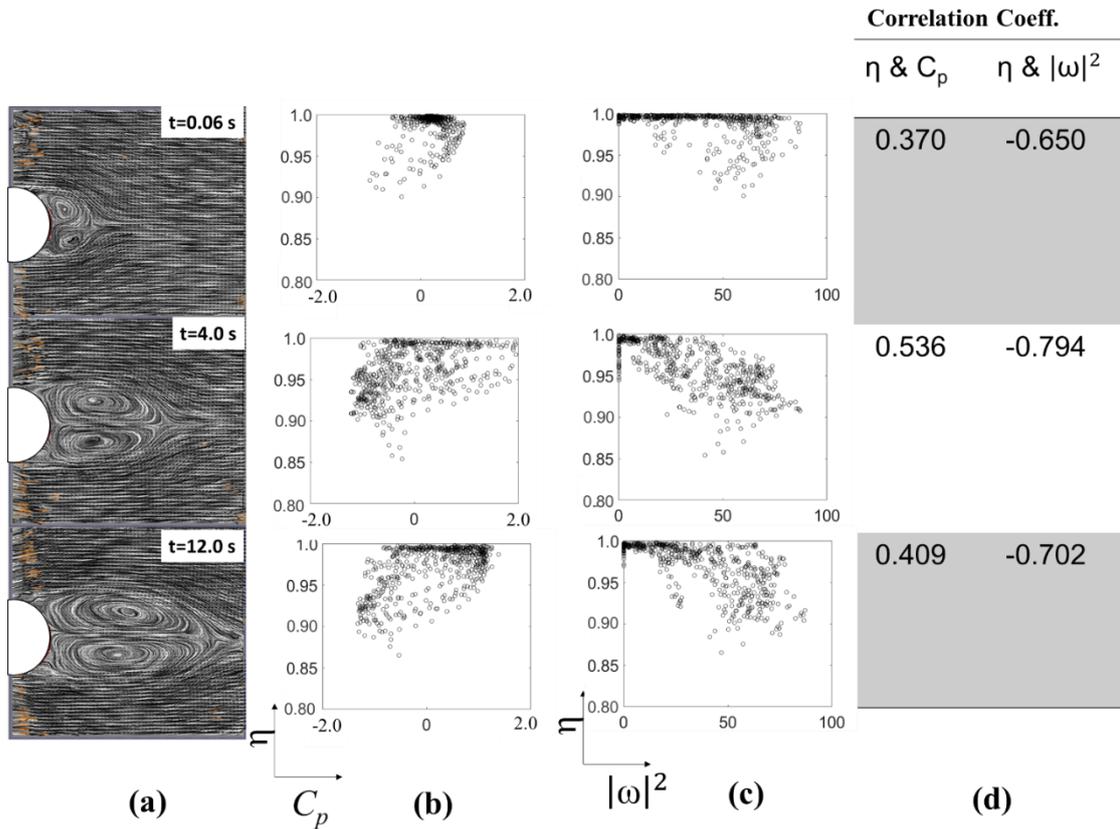
Fig. 4.12 (a) Line integral convolution plots at time t=0.06 s to 20 s, with correlation plots between (b) viscosity (η) and pressure (C_p) and (c) viscosity (η) vs enstrophy (d) corresponding correlation coefficients given at right.

4.6 Error propagation analysis

Several error propagation studies are reported in literature for Newtonian fluids (Sciacchitano and Wieneke 2016). Mostly the error propagation is affected by type of flow, spatial resolution and filtering method (Charonko et al. 2010b). Additionally, dimension of flow domain and boundary conditions are also important factors (Pan et al. 2016). It is worth to discuss the error propagation in this study because the governing equations and rheological models in non-Newtonian fluid are different from Newtonian fluids. In the pressure estimation procedure from experimental data, truncation error and precision errors are commonly encountered (van Oudheusden 2013). The numerical discretization of several derivative terms is the source of

truncation errors whereas uncertainty in measured velocity data propagates to pressure and produces precision errors. In this study the precision error propagation analysis is carried out for Eq.4.5 and 4.6. The precision error in all derivative terms are estimated from central difference scheme due to propagation of uncertainty in u and v i.e. ε_u and ε_v. Precision error associated with $\varepsilon_{\frac{\partial p}{\partial x}}$ and $\varepsilon_{\frac{\partial p}{\partial y}}$ terms can be written as:

$$\varepsilon_{\frac{\partial p}{\partial x}} = \sqrt{\left(\varepsilon_{u\frac{\partial u}{\partial x}}\right)^2 + \left(\varepsilon_{v\frac{\partial u}{\partial y}}\right)^2 + \left(\varepsilon_{\eta\frac{\partial^2 u}{\partial x^2}}\right)^2 + \left(\varepsilon_{\eta\frac{\partial^2 u}{\partial y^2}}\right)^2 + \left(\varepsilon_{\gamma_{xx}\frac{\partial u}{\partial x}}\right)^2 + \left(\varepsilon_{\gamma_{yx}\frac{\partial u}{\partial x}}\right)^2} \quad (4.16)$$

$$\varepsilon_{\frac{\partial p}{\partial y}} = \sqrt{\left(\varepsilon_{u\frac{\partial v}{\partial x}}\right)^2 + \left(\varepsilon_{v\frac{\partial v}{\partial y}}\right)^2 + \left(\varepsilon_{\eta\frac{\partial^2 v}{\partial x^2}}\right)^2 + \left(\varepsilon_{\eta\frac{\partial^2 v}{\partial y^2}}\right)^2 + \left(\varepsilon_{\gamma_{xy}\frac{\partial u}{\partial x}}\right)^2 + \left(\varepsilon_{\gamma_{yy}\frac{\partial u}{\partial x}}\right)^2} \quad (4.17)$$

The error propagation in convection terms is the same as in Newtonian fluid. The additional four terms are extra in non-Newtonian fluids. The precision error corresponding to each term is given below:

Error in convection terms:

$$\varepsilon^2_{\left[u\frac{\partial u}{\partial x}\right]} = \varepsilon_u^2\left[\left(\frac{\partial u}{\partial x}\right)^2 + \frac{u^2}{2\Delta x^2}\right], \quad \varepsilon^2_{\left[v\frac{\partial u}{\partial y}\right]} = \varepsilon_u^2\left[\left(\frac{\partial u}{\partial y}\right)^2 + \frac{v^2}{2\Delta y^2}\right] \quad (4.18)$$

Error in diffusion terms:

$$\varepsilon^2_{\left[\eta\frac{\partial^2 u}{\partial x^2}\right]} = \left\{\varepsilon_\eta^2\left(\frac{\partial^2 u}{\partial x^2}\right)^2 + \eta^2\left(\frac{\varepsilon_u}{\Delta x}\right)^2\right\}, \quad \varepsilon^2_{\left[\eta\frac{\partial^2 u}{\partial y^2}\right]} = \left\{\varepsilon_\eta^2\left(\frac{\partial^2 u}{\partial y^2}\right)^2 + \eta^2\left(\frac{\varepsilon_u}{\Delta y}\right)^2\right\} \quad (4.19)$$

$$\varepsilon^2_{\gamma_{xx}\left(\frac{\partial \eta}{\partial x}\right)} = \left\{ \left(\frac{\partial \eta}{\partial x}\right)^2 \left(\frac{2\varepsilon_u}{\sqrt{2}\Delta x}\right)^2 + \gamma_{xx}^{\,2}\left(\frac{\varepsilon_\eta}{\Delta x}\right)^2 \right\},$$

$$\varepsilon^2_{\gamma_{yx}\left(\frac{\partial \eta}{\partial y}\right)} = \left\{ \left(\frac{\partial \eta}{\partial y}\right)^2 \left(\frac{\varepsilon_v}{\sqrt{2}\Delta x} + \frac{\varepsilon_u}{\sqrt{2}\Delta y}\right)^2 + \gamma_{yx}^{\,2}\left(\frac{\varepsilon_\eta}{\Delta y}\right)^2 \right\} \qquad (4.20)$$

Eq. 4.19 and 4.20 shows that the error in diffusion term increases with ε_η. Eq. 4.19 shows that

the error in diffusion term is function of viscosity, which indicates that shear thinning property

could help in reducing error in shear layer and reverse flow region. However, the viscosity

gradient serves the opposite. If spatial resolution of measurement is higher, the error in diffusion

term will be suppressed but error amplifies in velocity derivative terms due to its inverse

relationship:

$$\varepsilon_{\left(\frac{\partial u}{\partial x}\right)} = \frac{\varepsilon_u}{\sqrt{2}\Delta x}, \quad \varepsilon_{\left(\frac{\partial^2 u}{\partial x^2}\right)} = \frac{2(\varepsilon_u)}{\Delta x} \qquad (4.21)$$

On the other hand, for Newtonian fluid flows the precision error propagated from uncertainty

of velocity (ε_v) in N-S equation can be written as

$$\varepsilon_{\frac{\partial p}{\partial x}} = \varepsilon_u \sqrt{\frac{1}{2\Delta t^2} + \frac{1}{2}\frac{u^2}{\Delta x^2} + \Delta u^2} \qquad (4.22)$$

$$\varepsilon_{\frac{\partial p}{\partial y}} = \varepsilon_u \sqrt{\frac{1}{2\Delta t^2} + \frac{1}{2}\frac{v^2}{\Delta y^2} + \Delta v^2} \qquad (4.23)$$

Compared with the Newtonian fluid, the expression of precision error in Non-Newtonian fluid

is a very complex function of flow velocity, grid space, and uncertainty of velocity. In addition

to these factors precise estimation rheological parameters is very important. In addition, error

propagation also depends on material and selection of rheological model.

Chapter 5

UVP based pressure estimation in shear-thinning fluid

5.1   Introduction

Most of industrial non-Newtonian fluids are opaque such as toothpaste, ketchup, shampoo etc. Unfortunately, PIV cannot be used to measure flow variable in those fluids. UVP (Tasaka et al. 2012) is an alternative option for pressure estimation in opaque non Newtonian fluid flows because it is based on ultrasound principle. In previous chapter, PIV measurements-based pressure estimation algorithm for slowly developing vortices attached to cylinder in steady flows and unsteady flows was introduced. For separated vortices migrated in the wake region the former algorithm is not applicable so a novel pressure estimation technique is developed based on UVP measurement which is applicable in unsteady flows in both transparent and opaque fluids.

5.2   Algorithm Development

The algorithm has five steps; velocity measurement, data filtering, 2D velocity field reconstruction, rheological modeling and pressure estimation. Individual steps of the organized algorithm are shown in Fig. 5.1

5.2.1 Velocity measurement

The velocity measurement was performed at Re=55 to 293, in wake of circular cylinder at three times diameter downstream of cylinder in CMC of wt. conc of 0.1%, with one UVP transducer set in vertical position in the experimental facility shown in Fig. 2.2. Measured *y* component of velocity in spatio-temporal domain the wake of cylinder is shown in Fig. 5.2(a). Here wake region can be identified by observing alternating positive and negative field of velocity. The

pixelized noise in measurement data can be clearly seen. Before using this data in CFD equations adequate filtering is required.
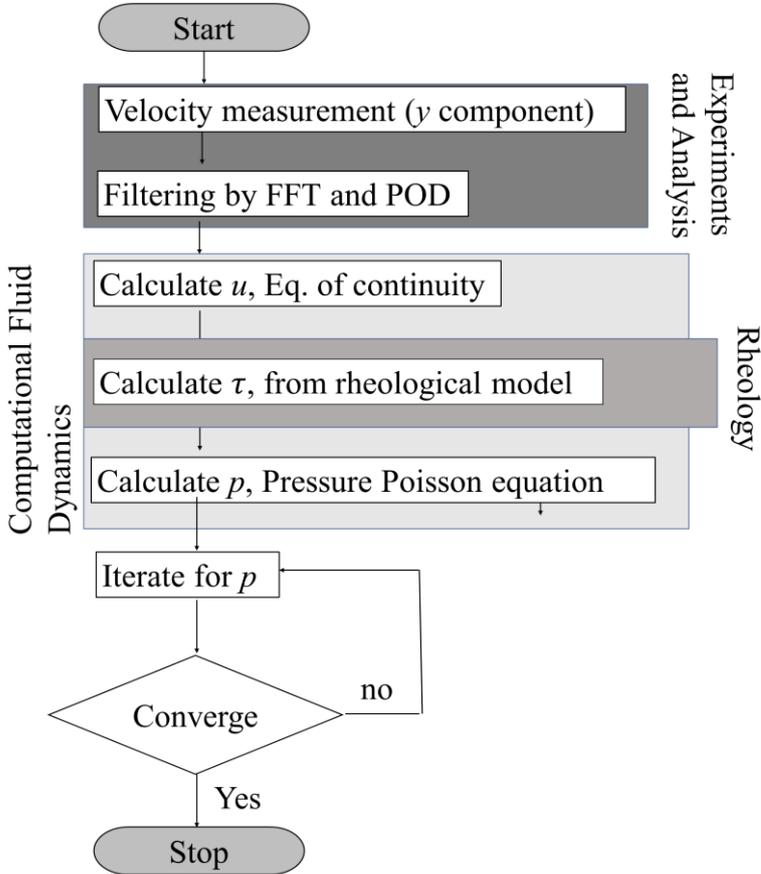
Fig. 5.1 Algorithm of pressure estimation based on UVP measurements
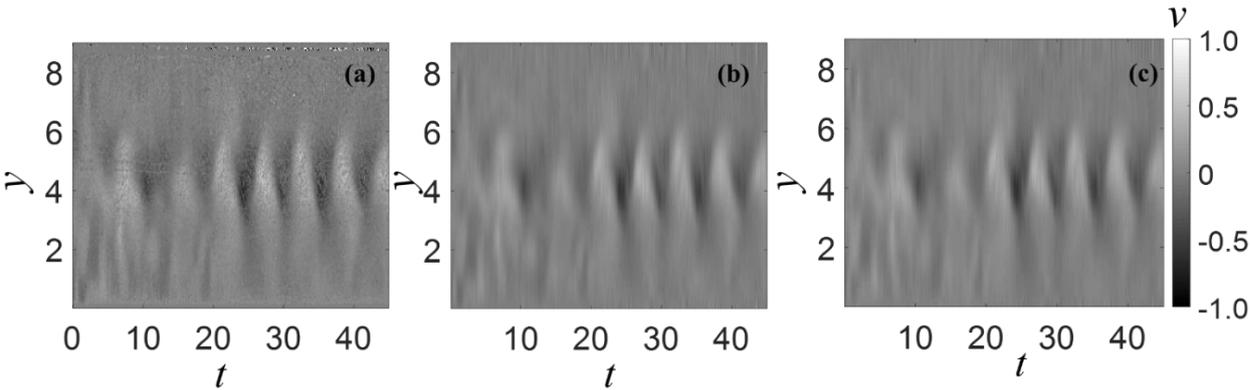
Fig. 5.2. Distribution of *y* component of measured velocity by UVP (a) raw velocity (b) velocity after FFT filtering (c) Velocity after FFT and POD filtering considering mode 1 to 10, *y* and *t* are non-dimensionalized respectively by diameter of cylinder (*d*) and *d/U*.

5.2.2 Data Filtering

Like PIV, velocity measurements by UVP also suffer from various noises. If proper attention in not rendered, these noises can magnify in calculation of velocity, viscosity and pressure. Combination of temporal (FFT, Fast Fourier Transform) and spatial (POD, Proper Orthogonal Decomposition) filtering in UVP data had been proved very efficient and is explained in chapter 3 and (Tiwari et al. 2019) . Same filtering technique was adopted here. After application of low pass filtering the experimental data is reconstructed in Fig. 5.2(b). Here high frequency noises are filtered, and this data is further analyzed with POD. POD (Sirovich 1987a) (Sirovich 1987b) decomposes the experimental data in orthonormal basis functions and resolves the kinetic energy into POD modes. First mode acquired the highest kinetic energy, 76% of total energy, which includes dominant structures of flow and mode 1 to 10 contains 99.5% of energy. In Fig. 5.2 (c), the reconstructed data after POD filtering is shown.

In the further sections, all governing equations are given in non-dimensional form. Following scaling variables, rendered dimensionless terms: D for length variables, U for velocity terms, ρU^2 for pressure. These equations are solved by finite difference method and all the equations are discretized by central difference scheme.

5.2.3   Reconstruction of 2D velocity field

Velocity information in t-y plane can be converted to x-y plane based on Taylor frozen hypothesis. This approach is discussed in section 3.2 along with equation of continuity to estimate the unknown component of velocity. The reconstructed 2D velocity vector field are shown in Fig. 5.3. Here dominant vortex structures are reconstructed when only mode 1 is considered for velocity reconstruction. When mode 1 to 3 are considered, very clear presence of staggered arrangement of vortices can be identified. Similarly, as more higher modes are considered, smaller vortices appear in a staggered pattern.
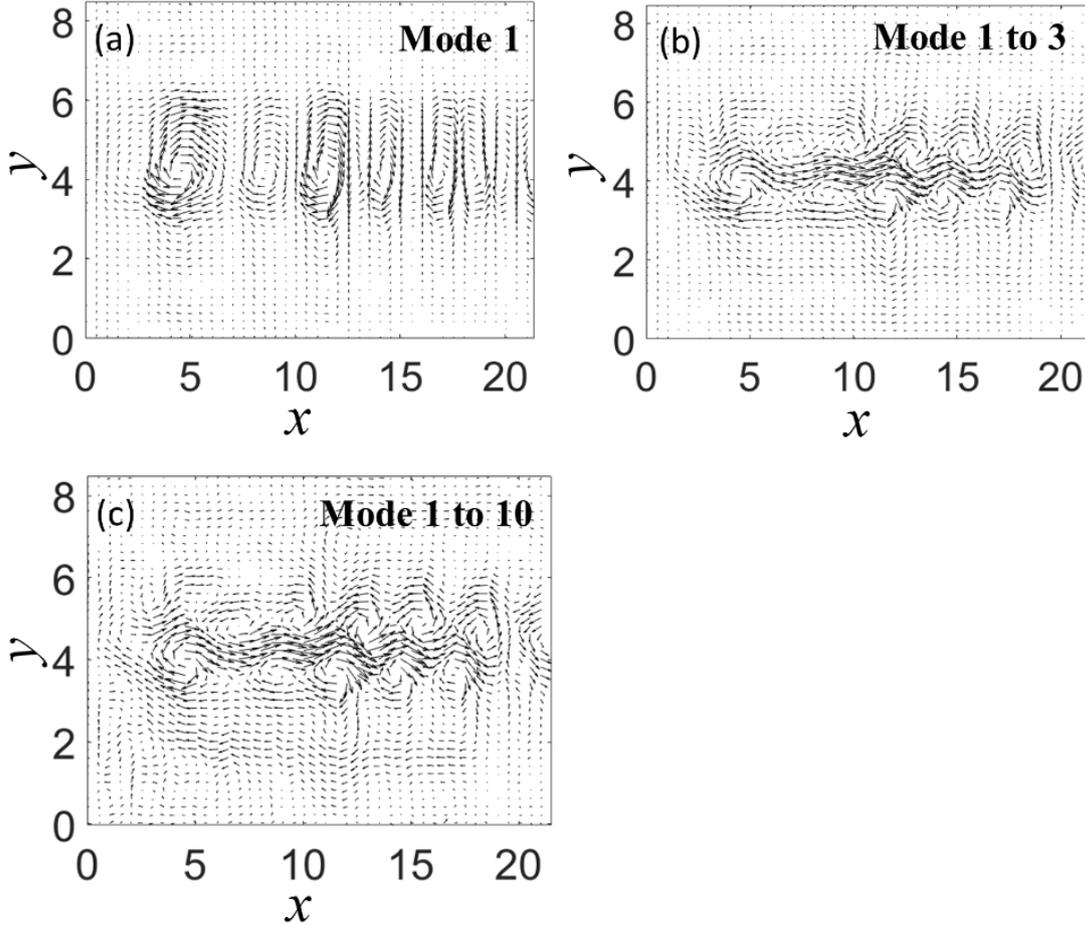
Fig. 5.3. Reconstructed velocity vector field considering POD (a) mode 1, (b) mode 1 to 3 and (c) mode 1to 10

5.3 Pressure Poisson equation for shear thinning fluid

The momentum conservation equations and rheological models are already discussed in section 4.2.1. Derivation of pressure Poisson equation for shear-thinning fluid is described here. After taking divergence of Eqs. 4.5 and 4.6 the pressure Poisson equation for two-dimensional flow can be written as

$$\nabla^2 p = \frac{\partial^2 p}{\partial x^2} + \frac{\partial^2 p}{\partial y^2} = \frac{\partial}{\partial x} term1 + \frac{\partial}{\partial y} term2 \qquad (5.1)$$

Here term1 and term 2 are as follows:

$$term1 = \left\{ -\left(u\frac{\partial u}{\partial x} + v\frac{\partial u}{\partial y} \right) + \frac{\eta}{\text{Re}}\left(\frac{\partial^2 u}{\partial x^2} + \frac{\partial^2 u}{\partial y^2} \right) + \frac{2}{\text{Re}}\left(\gamma_{xx}\frac{\partial \eta}{\partial x} + \gamma_{yx}\frac{\partial \eta}{\partial y} \right) \right\} \qquad (5.2)$$

58

$$term2 = \left\{ -\left(u\frac{\partial v}{\partial x} + v\frac{\partial v}{\partial y} \right) + \frac{\eta}{Re}\left(\frac{\partial^2 v}{\partial x^2} + \frac{\partial^2 v}{\partial y^2} \right) + \frac{2}{Re}\left(\gamma_{xy}\frac{\partial \eta}{\partial x} + \gamma_{yy}\frac{\partial \eta}{\partial y} \right) \right\}$$

Further differentiation of term 1 and term 2 with respect to x and y produces higher order and mixed derivatives.

$$\frac{\partial^2 p}{\partial x^2} + \frac{\partial^2 p}{\partial y^2} = -2\left(\frac{\partial u}{\partial x}\frac{\partial v}{\partial y} - \frac{\partial u}{\partial y}\frac{\partial v}{\partial x} \right) \tag{5.3}$$

$$+ \frac{1}{Re}\frac{\partial \eta}{\partial y}\frac{\partial}{\partial x}\left(\frac{\partial v}{\partial x} + \frac{\partial u}{\partial y} \right) + \frac{1}{Re}\frac{\partial \eta}{\partial x}\frac{\partial}{\partial y}\left(\frac{\partial v}{\partial x} + \frac{\partial u}{\partial y} \right)$$

$$+ \frac{2}{Re}\left(\frac{\partial^2 \eta}{\partial x^2}\frac{\partial u}{\partial x} + \frac{\partial \eta}{\partial x}\frac{\partial^2 u}{\partial x^2} \right) + \frac{2}{Re}\left(\frac{\partial^2 \eta}{\partial y^2}\frac{\partial v}{\partial y} + \frac{\partial \eta}{\partial y}\frac{\partial^2 v}{\partial y^2} \right) + \frac{2}{Re}\frac{\partial^2 \eta}{\partial x \partial y}\left(\frac{\partial v}{\partial x} + \frac{\partial u}{\partial y} \right).$$

In case of Newtonian fluid, the pressure Poisson equation is

$$\frac{\partial^2 p}{\partial x^2} + \frac{\partial^2 p}{\partial y^2} = -2\rho\left(\frac{\partial u}{\partial x}\frac{\partial v}{\partial y} - \frac{\partial u}{\partial y}\frac{\partial v}{\partial x} \right) \tag{5.4}$$

Unlike Newtonian fluid flows, the source term of pressure Poisson eq. in Non-Newtonian fluids is a function of viscosity so even after application of continuity equation, various terms do not cancel out and five additional terms appear as shown in Eq.5.3. Here, Poisson equation, contains two terms of the first order spatial derivative of viscosity and three terms of the second order and mixed derivatives of viscosity, thus, five terms in total. Here accurate computation of the second order spatial derivatives of viscosity is difficult since discretized approximation of the strain rate by Eq. 4.10 provides only the first order derivative of viscosity. Furthermore, cross spatial derivative in the last term of Eq. 5.3 needs 2-D third-order derivative of viscosity measurement. Considering these mathematical constraints in solving Poisson equation, for pressure calculation, Eq.5.1 was used in the current form i.e. first term1 and term 2 are calculated at all grid points and then their derivatives are calculated using finite difference method instead of directly computing higher order derivatives of velocity and viscosity at each grid points. All derivatives are calculated by second order finite difference scheme. Pressure

was obtained in an iterative manner in order to minimize the least square error (LSE). If spatial resolution of velocity is poor, such as PIV measurement even Eq. 5.1 cannot provide a converged solution of pressure. This limitation of PIV restricted its application in pressure estimation of unsteady fast developing flows.

After applying Taylor frozen hypothesis and equation of continuity, the 2D domain was treated as computational domain for pressure estimation. The spatial resolutions in x and y directions are 0.13 are 0.07mm. The boundary conditions of pressure are as follows:

At the left and right boundaries, Neumann boundary condition of pressure is applied and at bottom left corner Dirichlet condition of pressure is applied to control the absolute error. Zero pressure gradient conditions are applied along the top and bottom boundaries.

5.4   Results and discussions

5.4.1   Viscosity distribution

In Fig. 5.4, viscosity distribution in wake of cylinder by Carreau-Yasuda model is shown for three different cases corresponding to data considering, POD mode 1, mode 1 to 3 and POD mode 1 to 10. In reconstructed viscosity field corresponding to POD mode 1, low viscosity distribution appears in wake due to dominant vortex structures. The low viscosity due to presence of high strain rate represents the shear thinning property of aqueous solution of CMC. As higher modes are considered, due to the large number of vortices, low viscosity distribution became dense in the wake region. Interestingly, the arrangement of low viscosity regions is the same as vortices in wake.
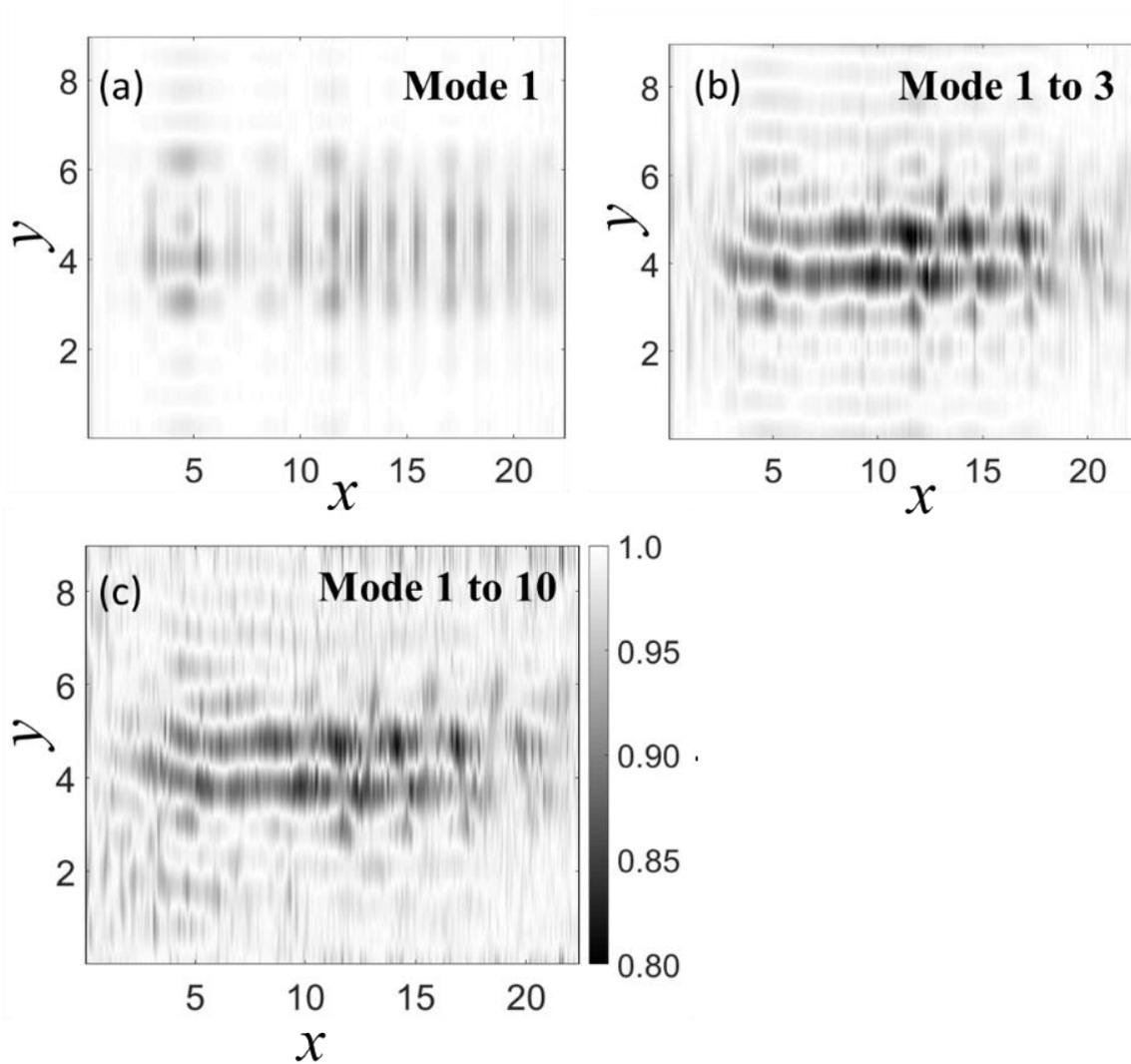
Fig. 5.4 Viscosity variation in computational domain for data corresponding to POD (a) mode 1 (b) mode 1 to 3 and (c) mode 1 to 10 respectively.

5.4.2 Pressure distribution

Pressure distribution obtained after solving Eq. 5.1, is shown in Fig. 5.5. Similar to viscosity determination, pressure distributions are obtained by considering POD mode 1, mode 1 to 3 and mode 1 to 10. The alternating low-pressure regions are observed in the wake region due to staggered arrangement of vortices. The presence of vortices can be easily distinguished by observing low pressure region.
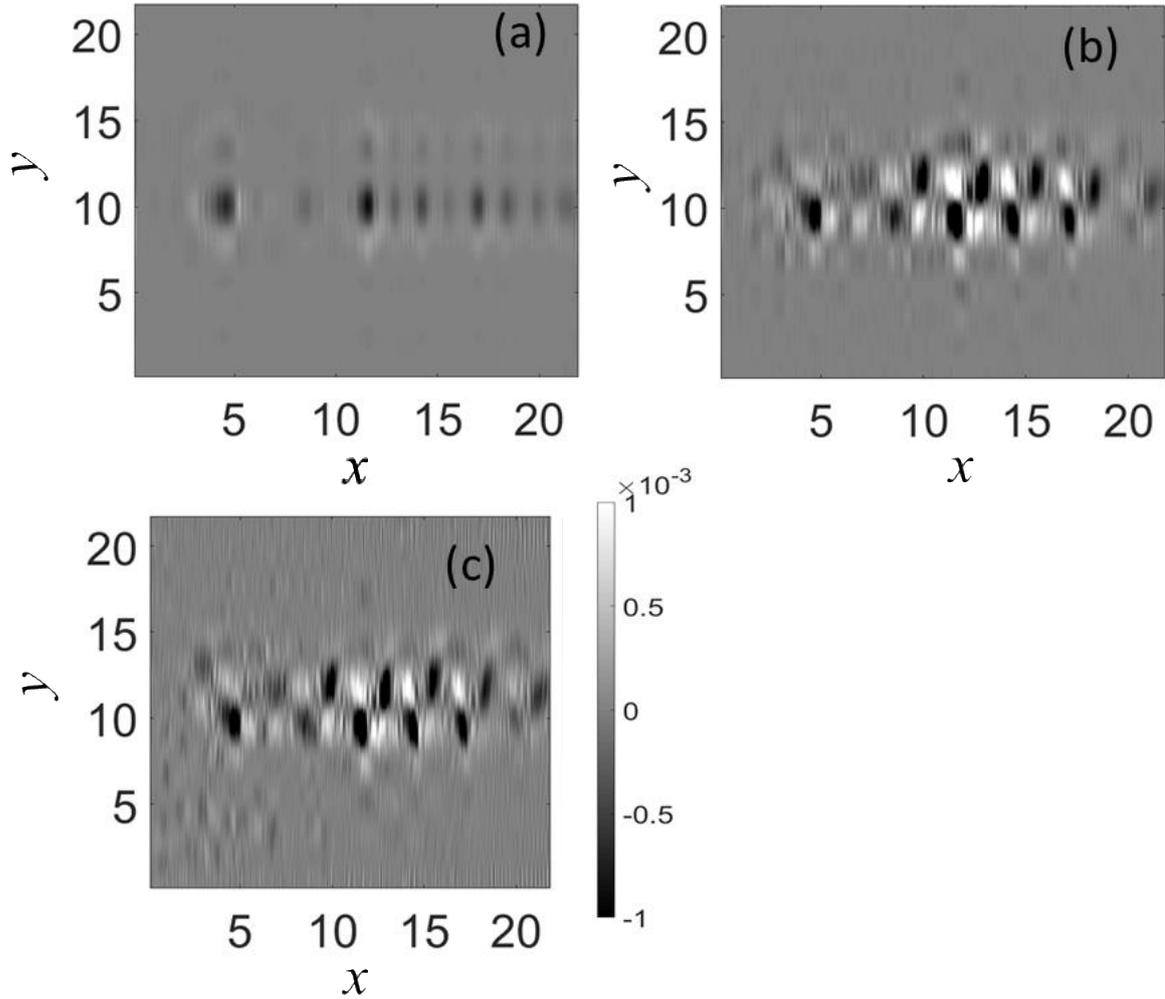
Fig. 5.5 Pressure distribution in computational domain considering velocity data of POD

(a) mode 1, (b) mode 1 to 3 and (c) mode 1 to 10.

5.4.3 Correlation of viscosity to enstrophy and pressure

Phase averaging was performed in range $7.5 \leq x \leq 17.5$ for pressure, viscosity and enstrophy ($|\omega|^2$) in wake, where $\omega = \nabla \times \mathbf{u}$. In Fig. 5.6, distribution of phase averaged pressure, viscosity and enstrophy distributions were plotted in ($7 \leq y \leq 16$) excluding free stream region. The low-pressure regions and corresponding to high viscosity regions are indicated in squares in Fig. 5.6 (a, b) which represents the inverse relation between pressure and viscosity. In Fig. 5.6(c) high enstrophy indicates high energy dissipation which is responsible for low viscosity in wake. These relations can be also confirmed by performing a quantitative assessment with cross-

correlation analysis. The correlations between pressure, enstrophy and viscosity were investigated for wake region $7.5 \leq x \leq 17.5$.
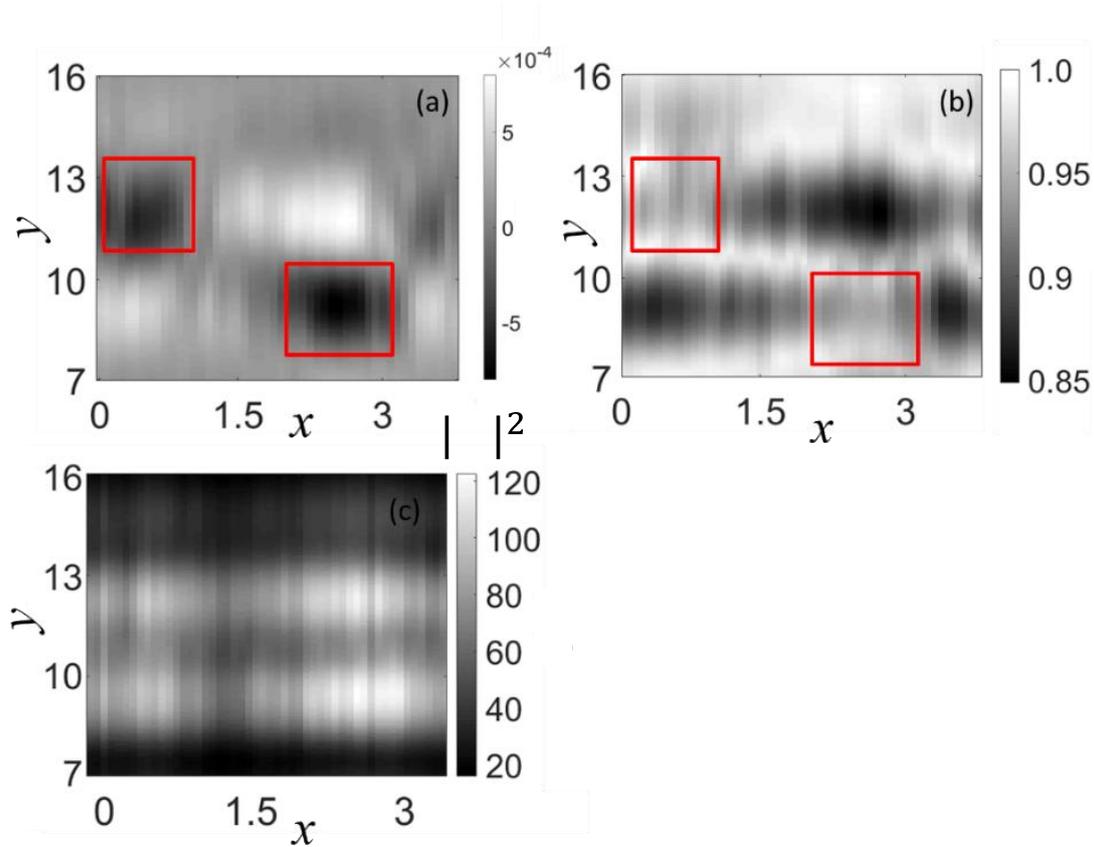
Fig. 5.6 Phase averaged (a) pressure (b) viscosity and (c) enstrophy distributions in wake

region

In Fig. 5.7, the viscosity variations with enstrophy and pressure are presented with correlation coefficient (Cc). The scatter plot of η vs $|\omega|^2$ and η vs Cp shows that, they have inverse relation which was confirmed by negative sign of Cc. This is also in the support of visual inspection of their characteristics shown in Fig. 5.6 (a, b). Quantitatively viscosity is more correlated with enstrophy than pressure which means that the shear thinning characteristic of fluid is more dependent on kinematics than the dynamics of fluid. In Fig 5.7 (b) the negative pressure region represents the region correspond to center of vortices and high-pressure region represent the shear layer between vortices. It was noted that, correlation coefficient is negative in wake which is opposite of our finding in the stage of slowly developing vortices. This can be also understood by observing the source term of pressure Poisson equation in Eq. 5.3, Q value and additional

opposite sign containing five terms of viscosity, due to shear thinning property these terms become lower thus pressure increases. On the other hand, negative correlation between viscosity and enstrophy supports the finding of vortex sustainability in developing vortices due to shear thinning property.
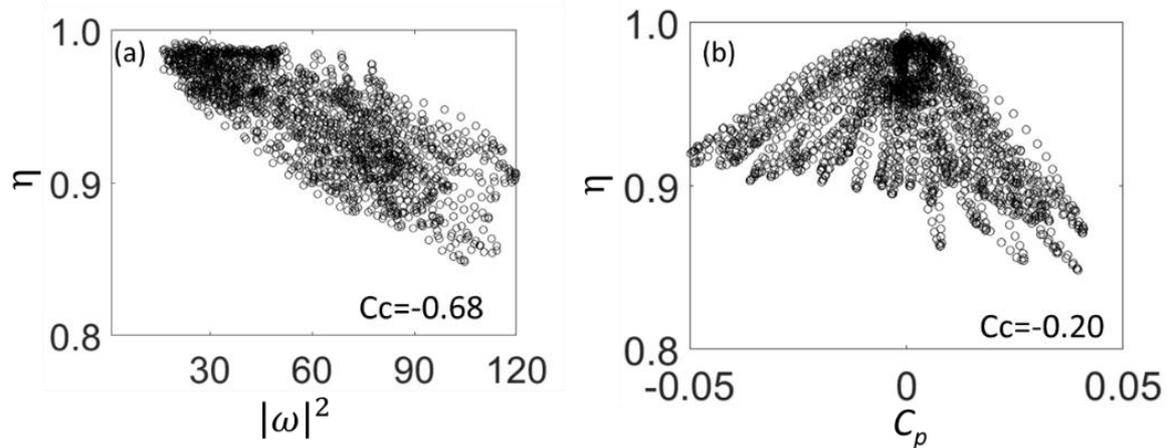
Fig. 5.7 Viscosity variation with (a) vorticity and (b) pressure in computational domain

5.5 Parametric study with Re

To analysis the effect of shear thinning in kinematics and dynamics of flow, a parametric study is conducted for flows at Re=58, 88, 146, 293 and pressure data are estimated by present algorithm. The reconstructed 2D velocity vectors are shown for several Re in Fig. 5.8. The number of vortices increases in the wake region for the same time duration in Fig. 5.7(a, b, c) respectively so the frequency of vortex shedding increases with Re which raises our expectation that Strouhal number (St) will also increase which is the typical Newtonian fluid behavior (Williamson 1996). However, in shear thinning fluid flows the Strouhal number decreases with Re even when vortex shedding frequency increases as shown in Fig. 5.9(a). As frequency of vortex shedding increases the low viscosity region became denser with *Re* in the wake region, as shown in Fig. 5.8. Due to lower viscosity in the wake the sustainability of vortex structures increases i.e. the vortices stay for the longer period so the vortex shedding frequency does not increase as much it increases in Newtonian fluid.
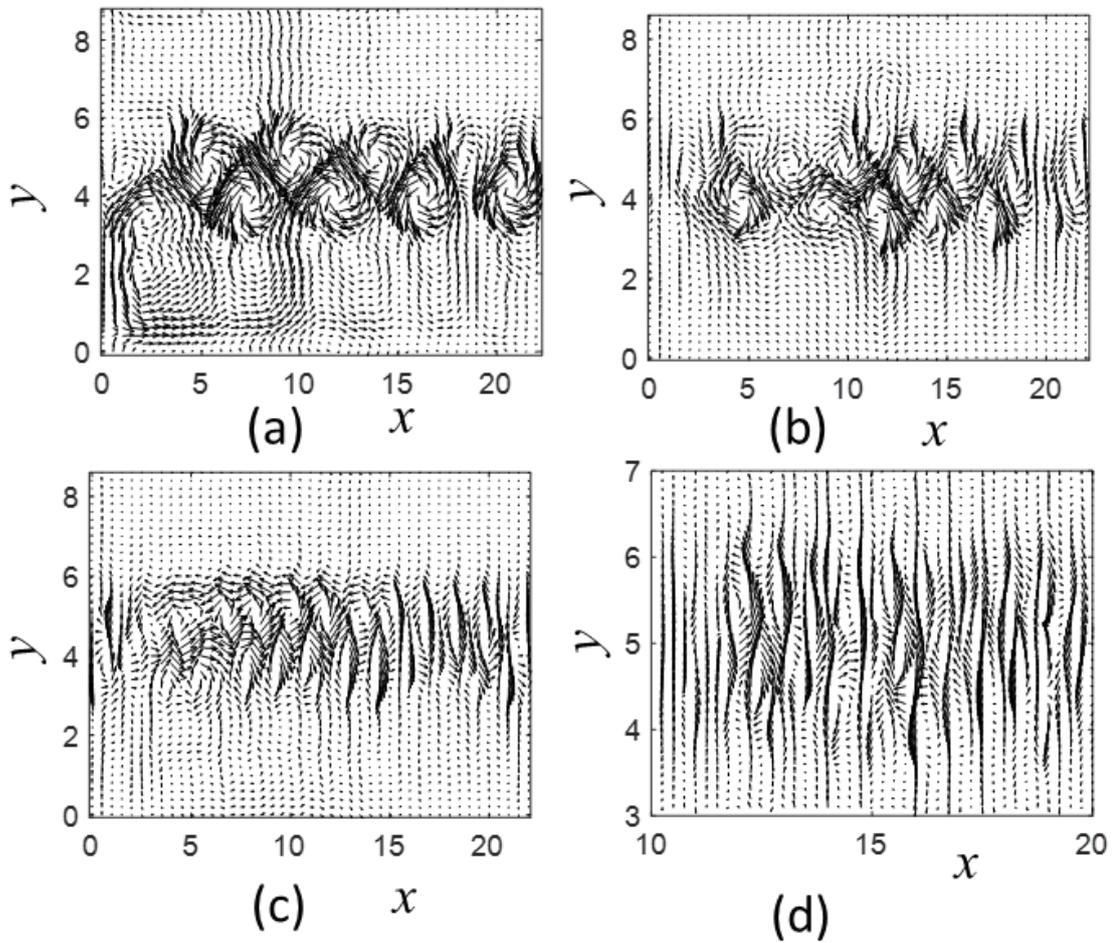
Fig. 5.8 Velocity vector plots obtained by UVP measurements filtered by FFT and POD at Re (a)58, (b)88, (c)146 (d) 293
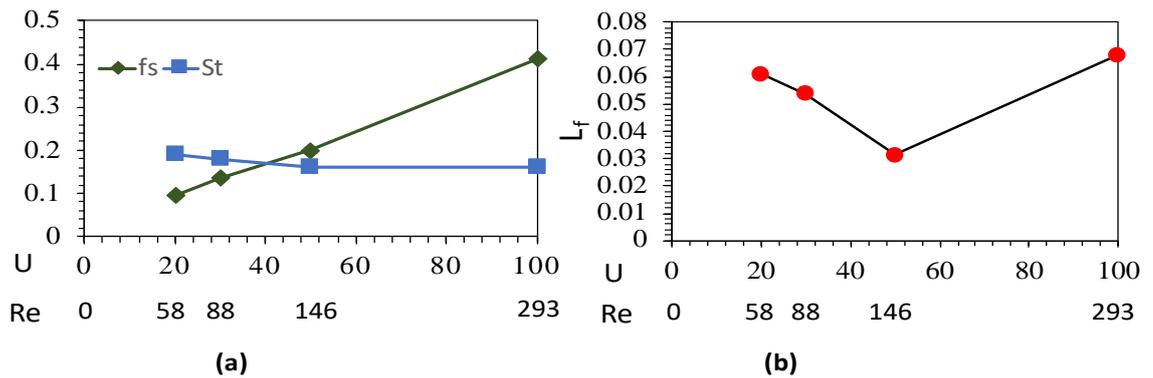
Fig. 5.9 variation with Re of (a) vortex shedding frequency and Strouhal number (b) vortex formation length
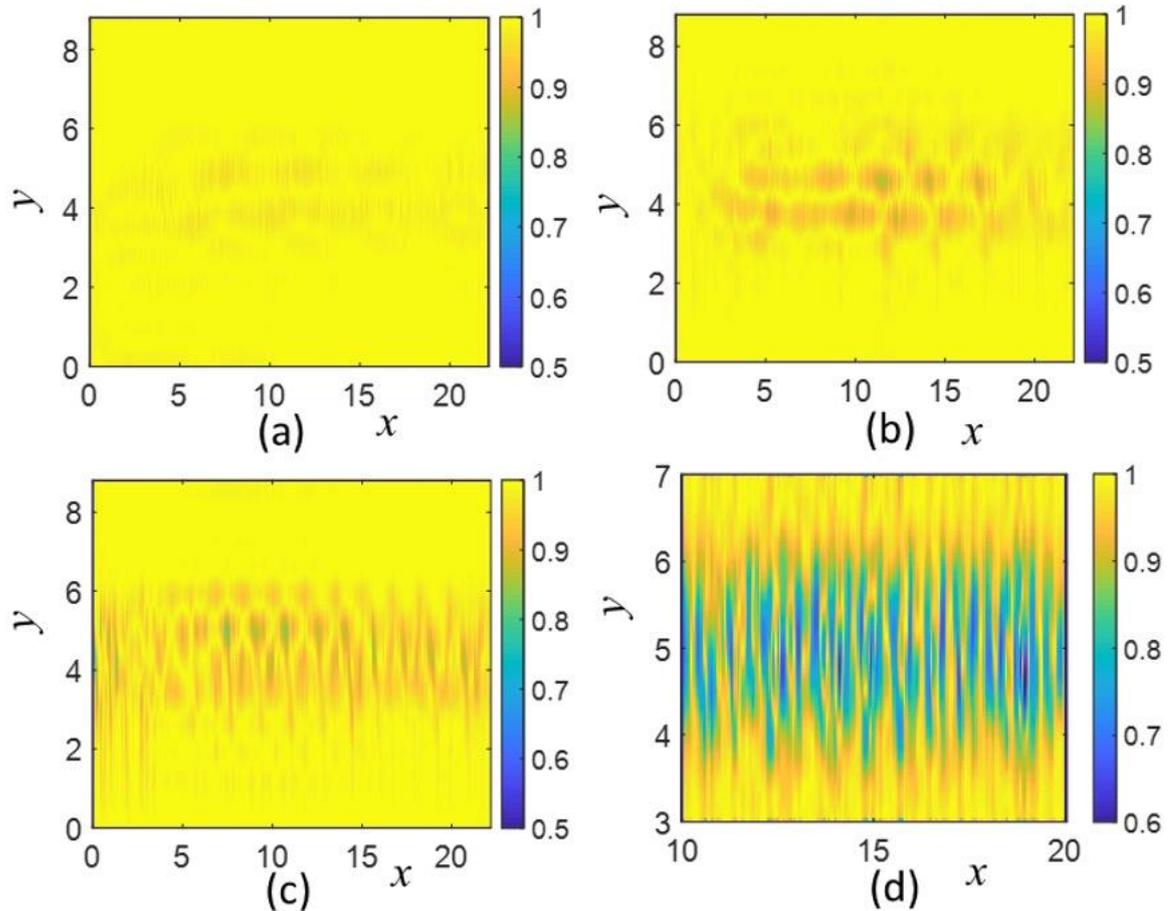
Fig. 5.10 Distribution of viscosity obtained by substitution of velocity data in Carreau- Yasuda model at Re (a)58, (b)88, (c)146 (d) 293

Vortex formation length in the cylinder flow is generally defined as the distance from center of cylinder to the point where time averaged streamlines cross itself. To determine the vortex formation length another analysis is conducted at same *Re* range with PIV data measured in experimental setup described in section 2.2. The vortex formation length decreases from 0.06 to 0.02 (Fig. 5.8(b)) as shown in Fig. 5.10 (a), (b), (c). This is in agreement with finding by (Bailoor et al. 2019) that vortex formation length decreases with increasing shear thinning. From Re=146 to 293 vortex formation increases (Fig. 5.10(d)). In Newtonian fluids the decrement in vortex formation length with Re up to 180 and increment at higher Re was also observed (Norberg 1987) (Chopra and Mittal 2019).
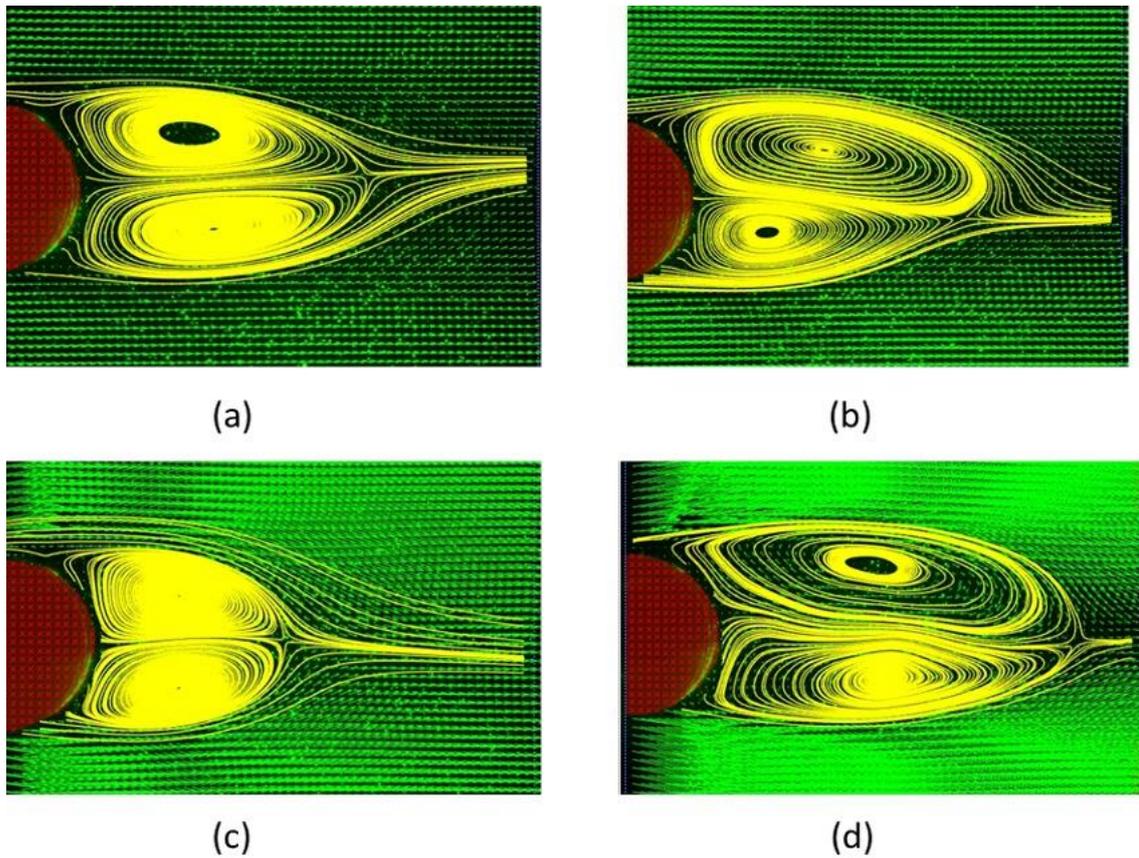
Fig. 5.11. Time averaged streamline plot obtained by PIV measurement performed at Re (a)58, (b)88, (c)146 (d) 293

Velocity and viscosity data corresponding to Fig. 5.8 and Fig. 5.10 are substituted in Eq.5.1 to determine the pressure distribution. Pressure plots are shown in Fig. 5.11. The alternating positive and negative pressure field was accurately reconstructed in wake region and lower pressure regions became denser due to presence of higher number of vortices in wake with increasing Re. To determine the relation of pressure and viscosity with increasing Re the phase averaging are performed in range $7.5 \leq x \leq 17.5$ viscosity and pressure field are plotted in Fig. 5.13. The inverse relation of viscosity with enstrophy and pressure is confirmed in flow if Re increases.

To understand the relation between viscosity with pressure and enstrophy with increasing Re, scattered plots are analyzed in Fig. 5.14. Here enstrophy increases with increasing Re and due to inverse relation viscosity decreases. This indicated that the vortex sustainability increases with increasing Re. However, from Re=146 the scattering started increasing until Re=293. On

the other hand, pressure is very weakly related to viscosity which also shows scattered pattern. Scattering indicates the dependency of viscosity on other parameters such as stresses and strains increases with Re.

To determine the dependency of viscosity on the normal and shear strains, scatter plots are analyzed and shown in Fig. 15.15. At Re=58 and 88, viscosity is clearly stronger function of shear strain than normal strains but at Re=146 the scattering in viscosity vs shear stresses plot starts increasing. The magnitude of normal strains also increases. Consequently, as Re increases to 293 the dependency of viscosity on shear strain is almost similar to normal strains as shown in Fig. 5.15(d1), (d2), (d3). This suggests that as Re increases the viscosity becomes strong function of normal strains along with shear strain so the viscosity estimation based on shear strain tests is not valid for high Re flows.
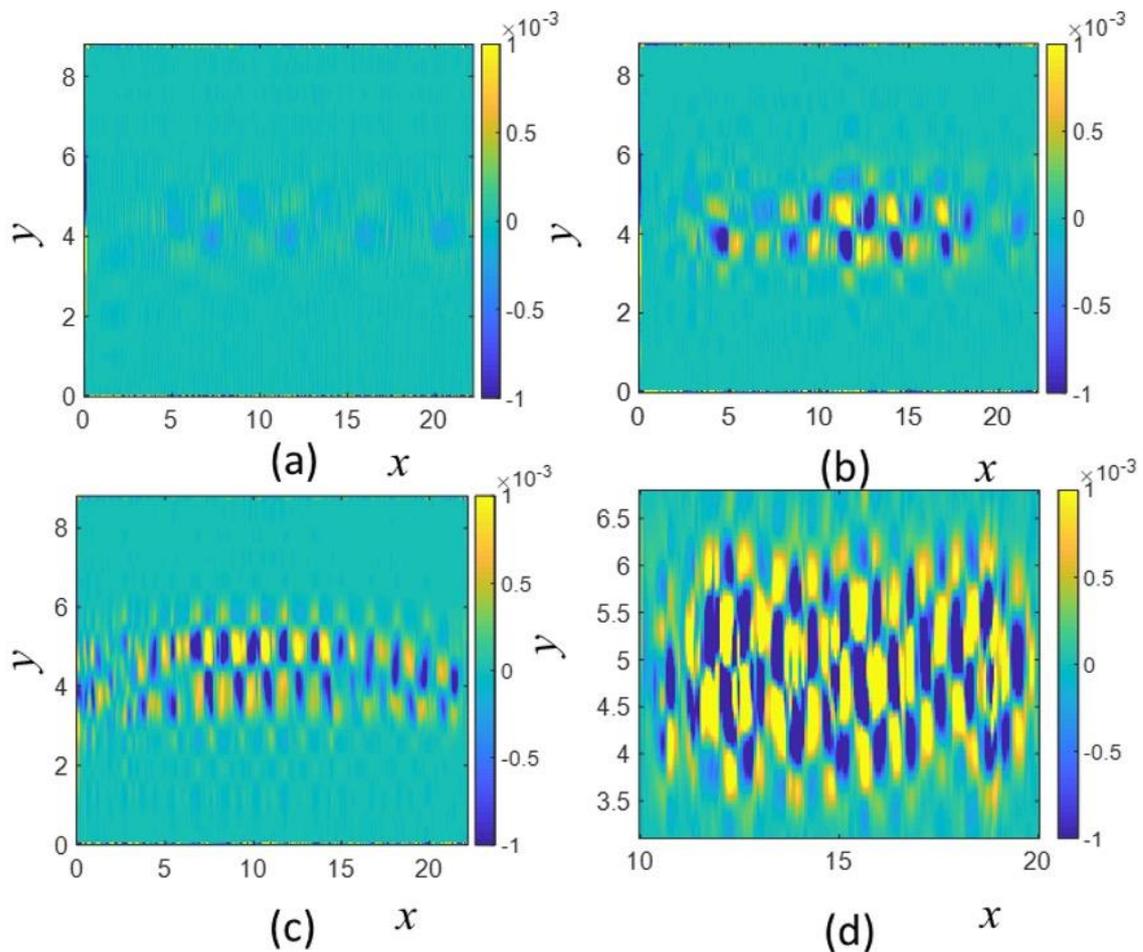
Fig. 5.12. Distribution of pressure for Re, (a) 55 (b) 88 (c) 146 (d) 293
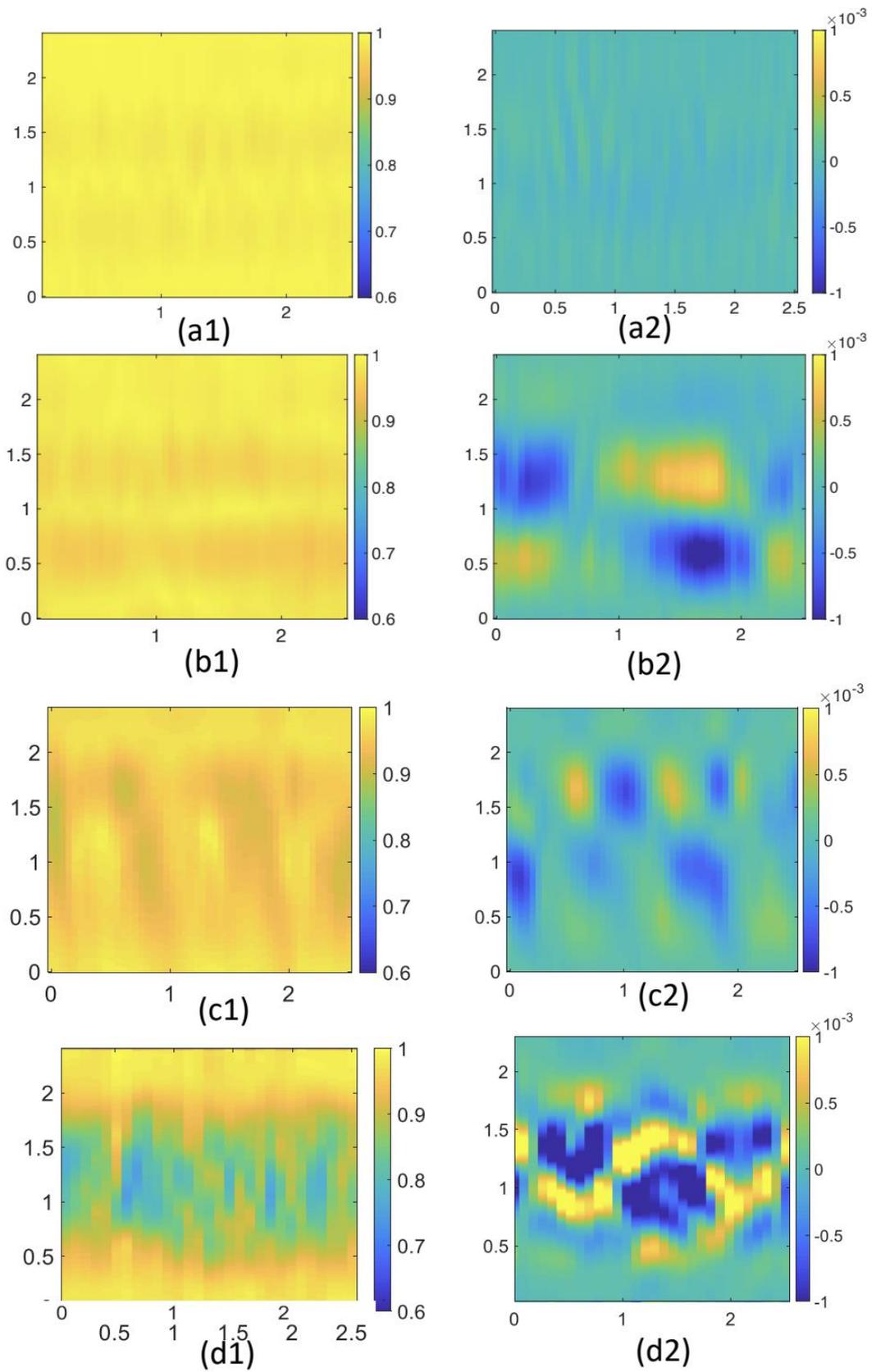
Fig. 5.13 Phase averaged viscosity and pressure plots for Re, (a1, a2) 55 (b1, b2) 88 (c1, c2) 146 (d1, d2) 293
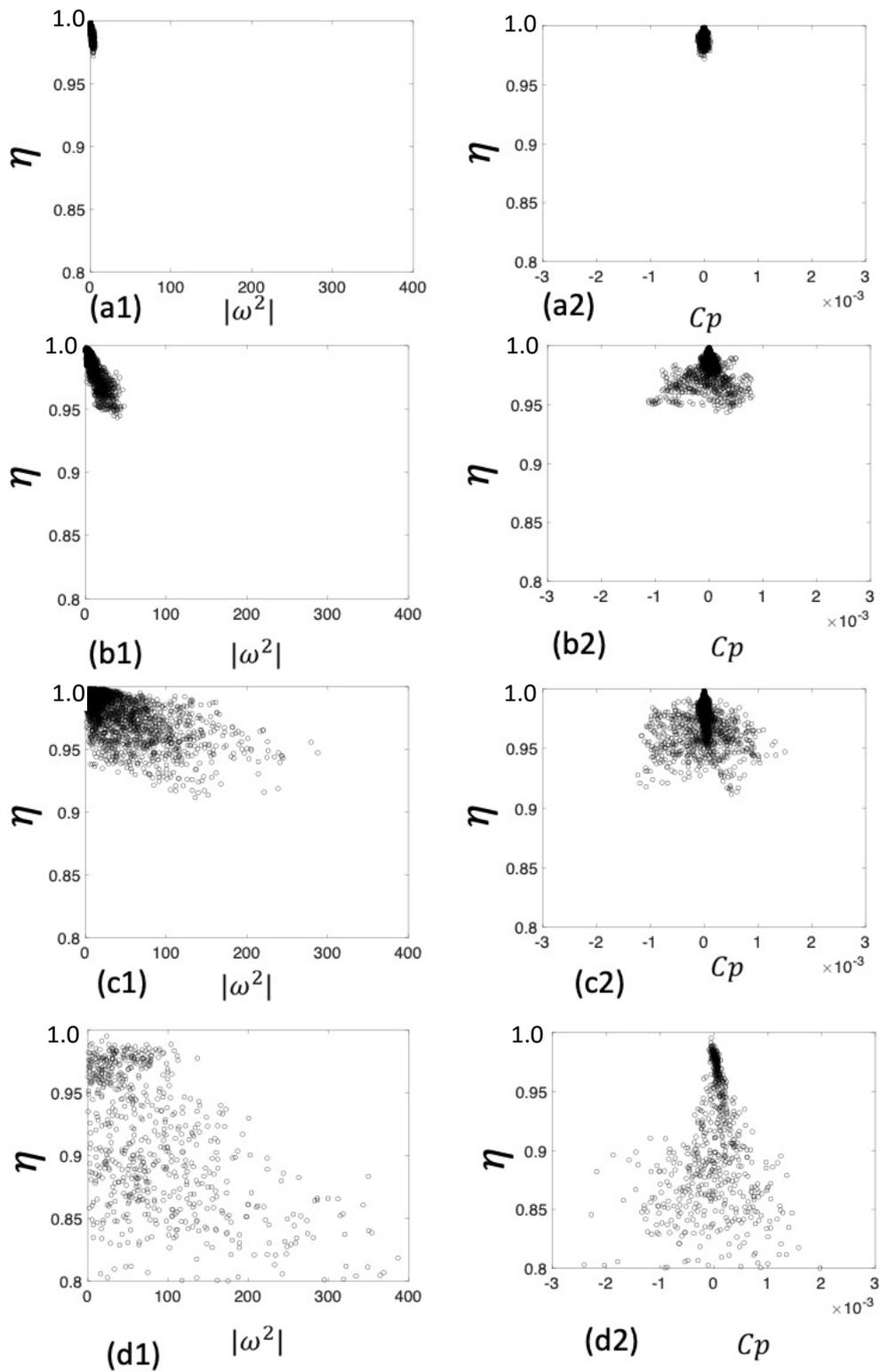
Fig. 5.14 Viscosity variation with vorticity and pressure for Re, (a) 55 (b) 88 (c) 146 (d) 293 in computational domain
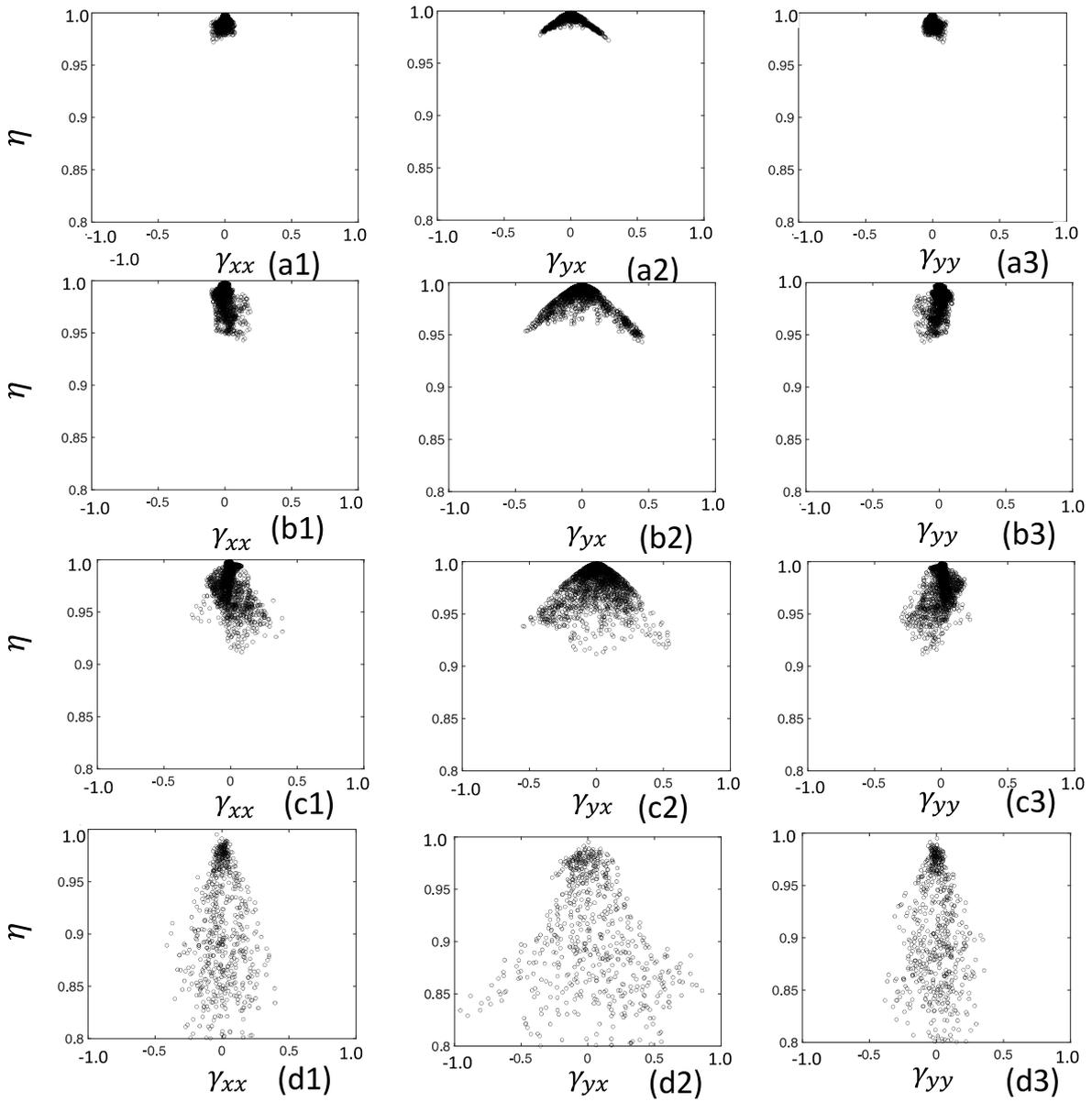
Fig. 5.15 Strains variation with vorticity and pressure for Re, (a) 55 (b) 88 (c) 146 (d) 293 in computational domain

Chapter 6

Irrotational correction of pressure gradient estimated from Pressure Poisson equation

6.1 Introduction

Pressure estimated from measured velocity data using PIV/PTV often suffers from noise propagating from uncertainty even after achieving convergence by an iterative approach. In ideal case, the error should be zero after convergence but with experimental data errors exist even after convergence is attained. A general error converging iterative procedure can be seen in Fig. 6.1. The residual error remains due to measurement noise. These residual errors can cause error up to 30% in instantaneous pressure (Ghaemi et al. 2012) (Azijli and Dwight 2015). Instantaneous pressure estimations from velocity data is even more sensitive to measurement noises (Azijli and Dwight 2015) (Azijli et al. 2016) (Charonko et al. 2010). Error analysis-based studies often use synthetic flow field for which analytical solutions are known: such as Taylor vortex, Lamb-Oseen vortex (McClure and Yarusevych 2017b), solid body rotation (Wang et al. 2016b) and direct numerical simulations data (Sciacchitano and Wieneke 2016) (Wang et al. 2016a). Error propagation in estimated pressure field depends on various factors such as spatial and temporal resolution of velocity data, boundary conditions of computational domain, size of domain, type of flow. For instantaneous pressure field even high spatial resolution of velocity data does not guarantee an accurate instantaneous pressure estimation (McClure and Yarusevych 2017a) (McClure and Yarusevych 2017b).

To improve the accuracy of pressure estimation several correction techniques have been tested by researchers such as average smoothening, moving average filtering, low pass filtering, proper orthogonal decomposition (POD) for filtering of velocity data. Among them POD, a physics based filter is more suitable for PIV/PTV data (Charonko et al. 2010a). Other methods are proposed based on divergence correction scheme using continuity equation (De Silva et al.

2013) and Helmholtz representation based filtering (Song et al. 1993). Firstly, a linear propagation analysis was introduced by (De Kat and Van Oudheusden) to understand the error propagation from uncertainty in measurement data to pressure data. Later Bayesian estimation framework have been proposed by (Azijli et al. 2016). Another framework of error analysis is proposed by (McClure and Yarusevych 2017a) based on divergence and curl of error. For curl correction in the pressure field, (Wang et al. 2016) proposed a minimal two norm criteria based irrotational correction method. They suggested that their IC correction method is not better than average smoothing in reducing curl. But it has global error correction characteristic which works well in correcting directional error propagation during integration of pressure gradients. Former two methods are suitable for pressure estimation from Navier-Stokes equation. The major source of error propagation i.e. integration of pressure gradients to evaluate pressure still exist. In addition, these techniques are not applicable to correct pressure field estimated by pressure Poisson equation.
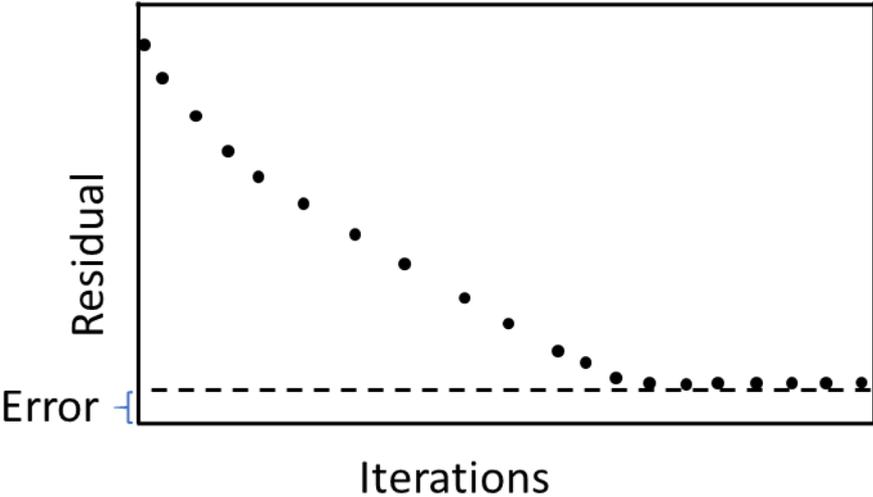
Fig. 6.1. Procedure of convergence during pressure estimation

6.2 Theoretical background

6.2.1 Pressure gradient error

The measured velocity can be seen as the sum of exact velocity data and error in velocity data. Similarly, pressure gradient is also sum of exact pressure and error, these can be represented in mathematical form as:

$$\mathbf{u} = \mathbf{u}_{ex} + \varepsilon_u \qquad (6.1)$$

$$\nabla P = \nabla P_{ex} + \varepsilon_{\nabla P} \qquad (6.2)$$

Here ε_u and $\varepsilon_{\nabla P}$ are error in velocity and pressure gradient data.

The analysis of error propagation characteristics in synthetic fields requires the addition of artificial noise in the analytical solution (Schneiders et al. 2016) (Lynch and Scarano 2014) (Azijli et al. 2016) (Charonko et al. 2010a). Some of the study used gaussian distributed noise (Liu and Katz 2006) (Pan et al. 2016) and (Wang et al. 2016) in velocity field and pressure field. Random error can be generated assuming gaussian distribution of random numbers with mean of zero and standard deviation of 1.

$$f\left(\varepsilon_{u\ or\ p}\right) = \frac{1}{\sqrt{2\pi\sigma}} \exp\left(\frac{-\left(x - \mu_m\right)^2}{2\sigma^2}\right) \qquad (6.3)$$

Here μ is mathematical expectation and σ is variance. A more suitable assumption of artificial error in PIV experiments is the combination of random error and correlated error due to overlap of interrogation windows (McClure and Yarusevych 2017a). In spatially correlated Gaussian noise, the covariance can be represented as

$$S^{ij} = \sigma^i \xi^{ij} \sigma^j \qquad (6.4)$$

Here σ^i is standard deviation of random error specified as below:

$$\sigma^i = \alpha \|u\|_2 + u_{peak} \qquad (6.5)$$

Here α is random error component Then correlated random error can be generated by

$\varepsilon_u^i = l^{ij}\lambda^j$, l can be obtained by using Cholesky decomposition of $S = ll'$.

6.3 Present IC correction method

Helmholtz representation theorem suggests that any finite, twice differentiable vector field can be expressed as sum of solenoidal vector field and irrotational vector field so gradient of pressure (∇P) which is a vector field can be written as

$$\nabla P = \nabla P_{sol} + \nabla P_{irrotational} = \nabla \times F + \nabla\Psi \qquad (6.6)$$

Here F is scalar potential and ψ is vector potential. Divergence on both side of Eq. 6.6 gives

$$\nabla.\nabla P = \nabla.\nabla \times F + \nabla^2\Psi \qquad (6.7)$$

A new form of Poisson equation can be obtained by applying the condition of divergence of a curl is zero in Eq. 6.7.

$$\nabla^2\Psi = \nabla^2 P \qquad (6.8)$$

Equation 6.8 can provide distribution of irrotational pressure. $\nabla^2 P$ which itself is a Laplacian is the source term in Eq. 6.6 which increases the curl correction significantly as compared with usual pressure Poisson equation. Laplacian operator already has curl correction characteristics (Wang et al. 2016). Moreover, it is also applicable for curl correction in Navier-Stokes estimated pressure field.

$$\nabla^2\Psi = \frac{\partial}{\partial x}\left(\frac{\partial P}{\partial x}\right) + \frac{\partial}{\partial y}\left(\frac{\partial P}{\partial y}\right) \qquad (6.9)$$

The solution of Poisson equation is very sensitive to boundary conditions. So, for more realistic pressure in boundaries, estimated pressure field from pressure Poisson equation or Navier-Stokes equation can be used. The discretized form is given below:

$$\psi_{i,j} = \frac{1}{2}\left(\frac{1}{\Delta x^2} + \frac{1}{\Delta y^2}\right)^{-1} \left[\begin{array}{l} \left\{\dfrac{\psi_{i+1,j}+\psi_{i-1,j}}{\Delta x^2} + \dfrac{\psi_{i,j+1}+\psi_{i,j-1}}{\Delta y^2}\right\} - \\[2ex] \left[\left(\dfrac{-P_{i-2,j}-16P_{i-1,j}-30P_{i,j}+16P_{i+1,j}+P_{i+2,j}}{12\Delta x^2}\right) + \right. \\[2ex] \left.\left(\dfrac{-P_{i,j-2}-16P_{i,j-1}-30P_{i,j}+16P_{i,j+1}+P_{i,j+2}}{12\Delta y^2}\right)\right] \end{array}\right] \tag{6.10}$$

Here $\nabla^2\psi = \nabla^2 P$ is discretized with three-point central difference scheme and $\nabla^2 P$ is discretized with five-point central difference scheme. The computational cost will be almost double, if pressure Poisson equation is used for pressure estimation with present IC method. On the other hand, if pressure is estimated from Navier-Stokes equation the discretized form of Eq. 6.9 can be used to obtain the curl free pressure distribution.

$$\psi_{i,j} = \frac{1}{2}\left(\frac{1}{\Delta x^2} + \frac{1}{\Delta y^2}\right)^{-1} \left[\begin{array}{l} \left\{\dfrac{\psi_{i+1,j}+\psi_{i-1,j}}{\Delta x^2} + \dfrac{\psi_{i,j+1}+\psi_{i,j-1}}{\Delta y^2}\right\} - \\[2ex] \left\{\left(\dfrac{\left.\dfrac{\partial P}{\partial x}\right|_{i+1,j} - \left.\dfrac{\partial P}{\partial x}\right|_{i-1,j}}{2\Delta x}\right) + \left(\dfrac{\left.\dfrac{\partial P}{\partial y}\right|_{i,j+1} - \left.\dfrac{\partial P}{\partial y}\right|_{i,j+1}}{2\Delta y}\right)\right\} \end{array}\right] \tag{6.11}$$

6.4 Results and discussion

The synthetic velocity data is extracted from analytical velocity field for Taylor vortex given by following equation in to a regular grid

$$u_\theta = \frac{H}{8\pi}\frac{r}{vt^2}\exp\left(\frac{-r^2}{4vt}\right) \tag{6.12}$$

where r, t, and v are the radial position from the vortex center, time elapse, and kinematic viscosity of fluid. For generating the synthetic PIV data with noise, we set $H= 7.5\times10^{-5}$ m, $v=1\times10^{-6}$ m^2 s^{-1}, $\rho=1000$ kg m^{-3}, and $t=0.5$ s. In the present study, correlated random artificial

noise with α=0.01, 0.05 and 0.1 are added to velocity data of Taylor vortex (Eq. 6.12). The interrogation window size is assumed to 16×16 px and overlap is 50%. As described by (Sciacchitano and Wieneke 2016) ξ^{ij} in Eq.6.4 can be constructed by triangular function

$$\left(1-\frac{|x|}{n_{px}}\right) \text{ for } |x|\le n_{px} \text{ otherwise } 0.$$

6.4.1   Pressure estimation by pressure Poisson Equation with correlated noise

Pressure is estimated by solving pressure Poisson Eq. 1.6 for velocity field corresponding to α=0.01, 0.05 and 0.1. All the terms in pressure Poisson equations are discretized with three point central difference scheme and reconstructed pressure fields are shown in Fig. 6.2 (a, b, c). Here error in pressure increases with increasing α.
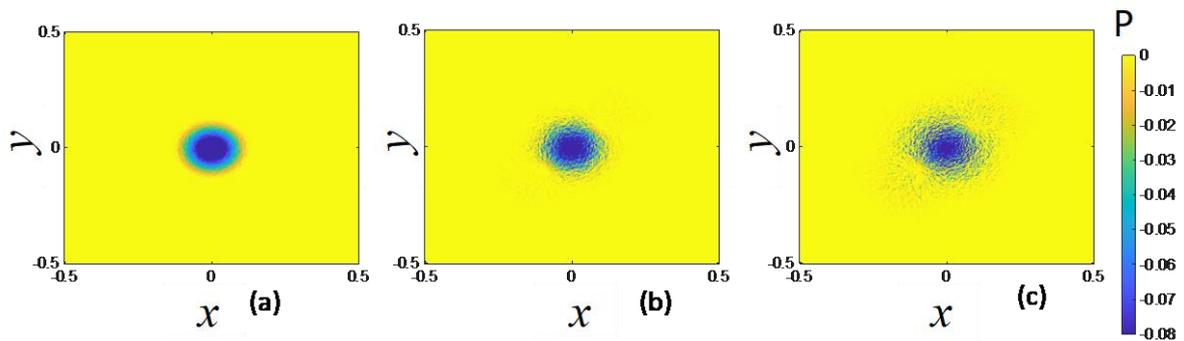
Fig. 6.2 Distribution of pressure determined by pressure Poisson Eq. for α1 (a1, a2), α2 (b1, b2), α3 (c1, c2)

For the correction of pressure field Eq. 6.8 is applied in each case to obtain the irrotational pressure field. The reconstructed pressure fields are shown in Fig. 6.3. Here the reconstructed pressure fields are idential to exact pressure field.
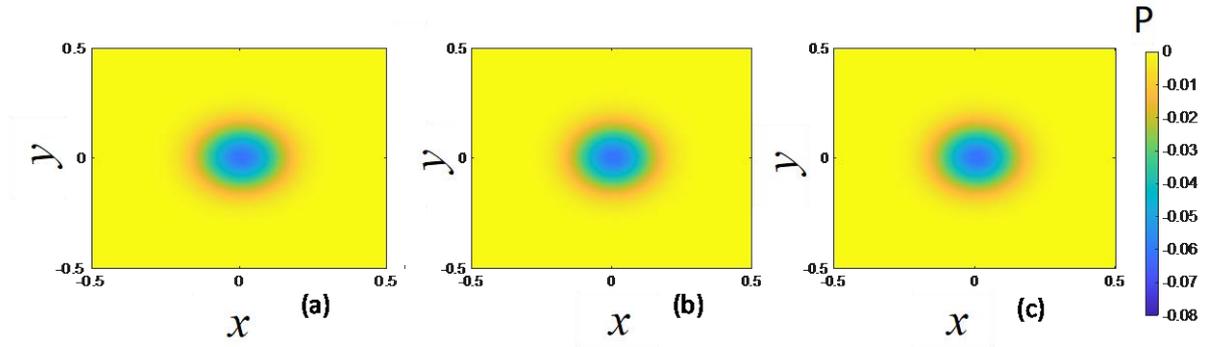
Fig. 6.3 Distribution of pressure reconstructed by applying present correction for

$\alpha 1$ (a1, a2), $\alpha 2$ (b1, b2), $\alpha 3$ (c1, c2)

To quantify the error in corrected pressure field compared with pressure Poisson equation, Monte Carlo simulation is performed for 3000 evaluations from present method in a horizontal line along the center of the domain. Bias ($\overline{\varepsilon_p}$) and random (ε_p') errors are evaluated for pressure and pressure gradient and shown in Fig. 6.4. Here both bias and random error in pressure Poisson estimated pressure field are higher compared to present corrected reconstructed pressure field.
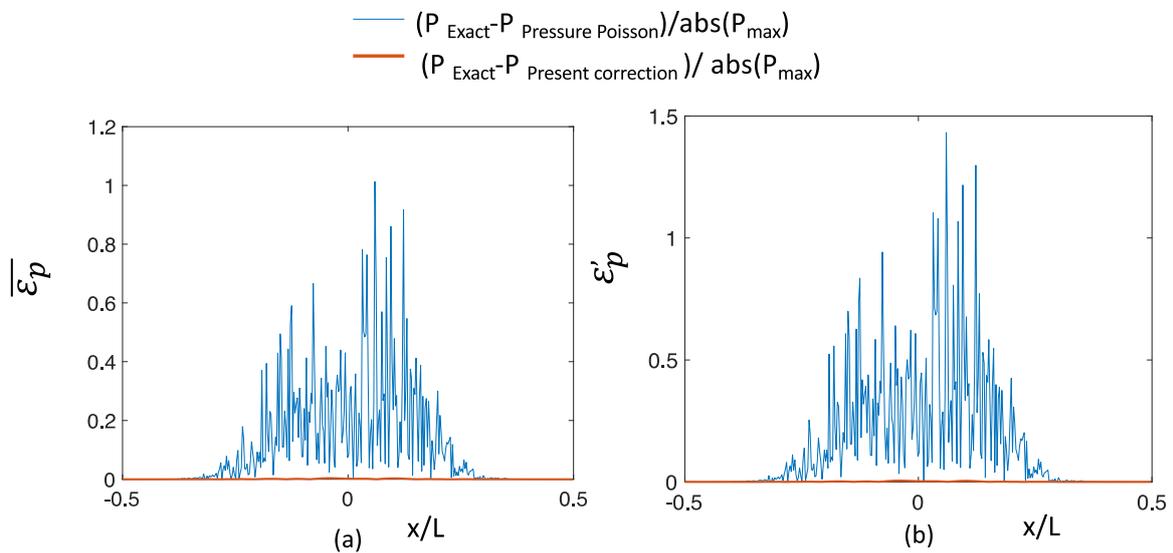
Fig. 6.4 (a) Mean and (b) standard deviation of error statistics calculated over 3000 realizations of pressure by present method

6.4.2 Pressure estimation from Navier-Stokes by irrotational correction

Pressure gradients estimated by Navier-Stokes needs to be integrated over multiple paths to obtain pressure field. An efficient pressure integration approach reduces the multiple paths to just two path by irrotational correction which is known as orthogonal path integration (OPI) as proposed by (Wang et al. 2016). This indicated that the curl correction can reduce the number of paths required for integration to obtain the accurate pressure field. In this study, we applied the present curl correction method to pressure gradient obtained by Navier-Stokes equation. The Taylor vortex velocity data are extracted in regular grid and correlated and random errors are added with α=0.01, 0.05 and 0.1. Then pressure gradients are estimated by solving Navier-Stokes Eq. 1 for each case. Each term of Navier-Stokes equation is discretized with three point central difference scheme. The PDF of curl of pressure gradients are plotted in Fig. 6.5 (a1, b1, c1). Reconstructed pressure field is shown in Fig. 6.5 (a2, b2, c2). Here curl free pressure field is determined without integrating pressure gradient field. To quantify the error in pressure field the PDF of curl of pressure gradients are plotted for corrected pressure field in Fig. 6.5 (a3, b3, c3). The curl is of order 10^1 which is almost as accurate as pressure corrected from pressure Poisson equation. In addition present method can potentially reduce the steps of finding the error in pressure gradients compared to many published researches (McClure and Yarusevych 2017b) (Wang et al. 2016). (Pan et al. 2016).
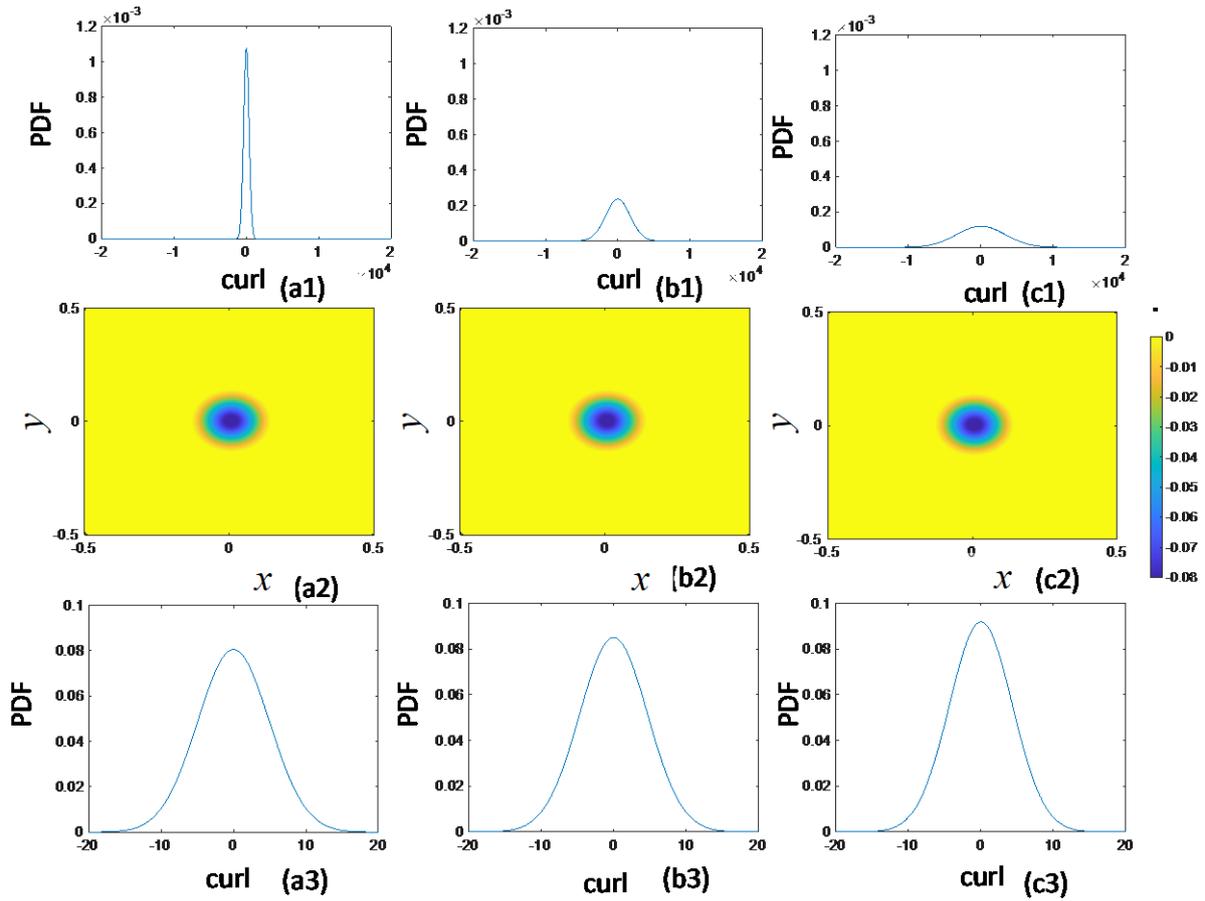
Fig. 6.5 PDF of curl of pressure gradients before and after curl correction and reconstructed pressure field for $\alpha 1$ (a1, a2, a3), $\alpha 2$ (b1, b2, b3), $\alpha 3$ (c1, c2, c3)

6.4.3 Present correction in PIV data

From flow visualized image Fig 6.6 (a), the measurement domain by PIV is treated as computational domain and for that suitable boundary conditions are applied as shown in Fig. 6.6 (b). At the left and right boundaries Neumann boundary condition is applied and in corners Dirichlet Condition of pressure is applied to control the absolute error. The top and bottom boundaries are defined as zero pressure gradients. The pressure distribution is obtained by solving pressure Poisson equation. Successive over relaxation (SOR) scheme was adopted to solve iteratively. Maximum square error (MSE) of pressure discrepancy is calculated at each iteration step to monitor numerical convergence. When MSE falls below 10-4 (dimensionless), the pressure is accepted as final solution. The overall algorithm of this process is shown in Fig. 6.6 (c).
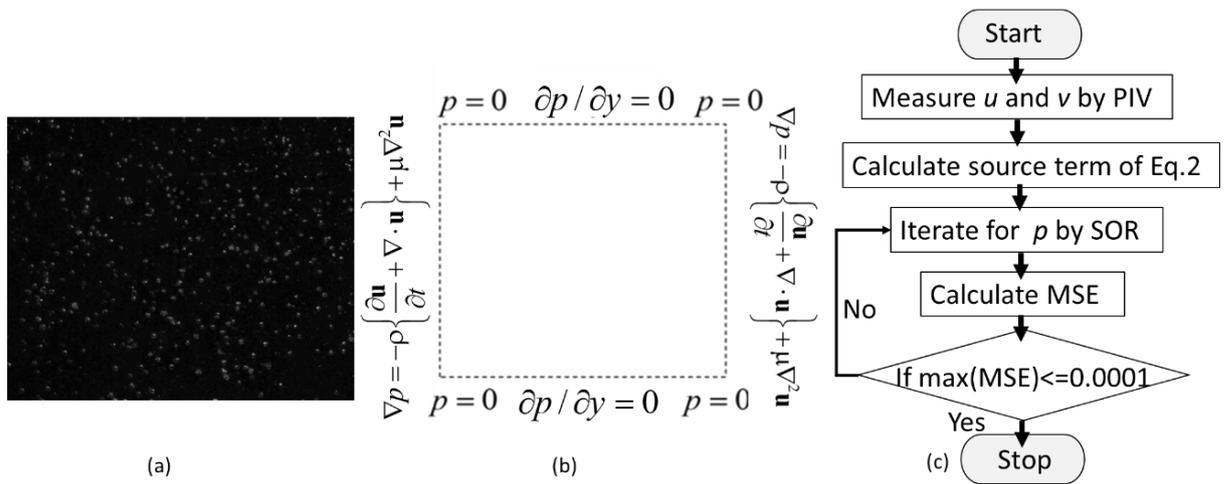
Fig. 6.6 (a) Visualized image (b) Computational domain and boundary condition (c) algorithm

6.4.3.1 Comparison of IC with other filtering techniques

In this section three different PIV, unfiltered and filtered velocity are used for assessment of IC method. For filtering, low pass FFT (Fast Fourier Transform) and POD (Proper Orthogonal decomposition) are opted. Pressure obtained by unfiltered velocity data before and after correction are shown in Fig. 6.7 (a1, a2). Here reconstructed pressure field after applying IC method is noise free. Similarly, FFT and POD filtered velocity data evaluated pressure fields are shown in Fig. 6.7(b1, b2), (c1, c2) respectively. Pressure data evaluated from velocity dataset with FFT and POD filtering have filtered the true velocity data and magnitude of pressure reduced. The present correction method could reconstruct the pressure field however the lost information of true data could not be recovered.
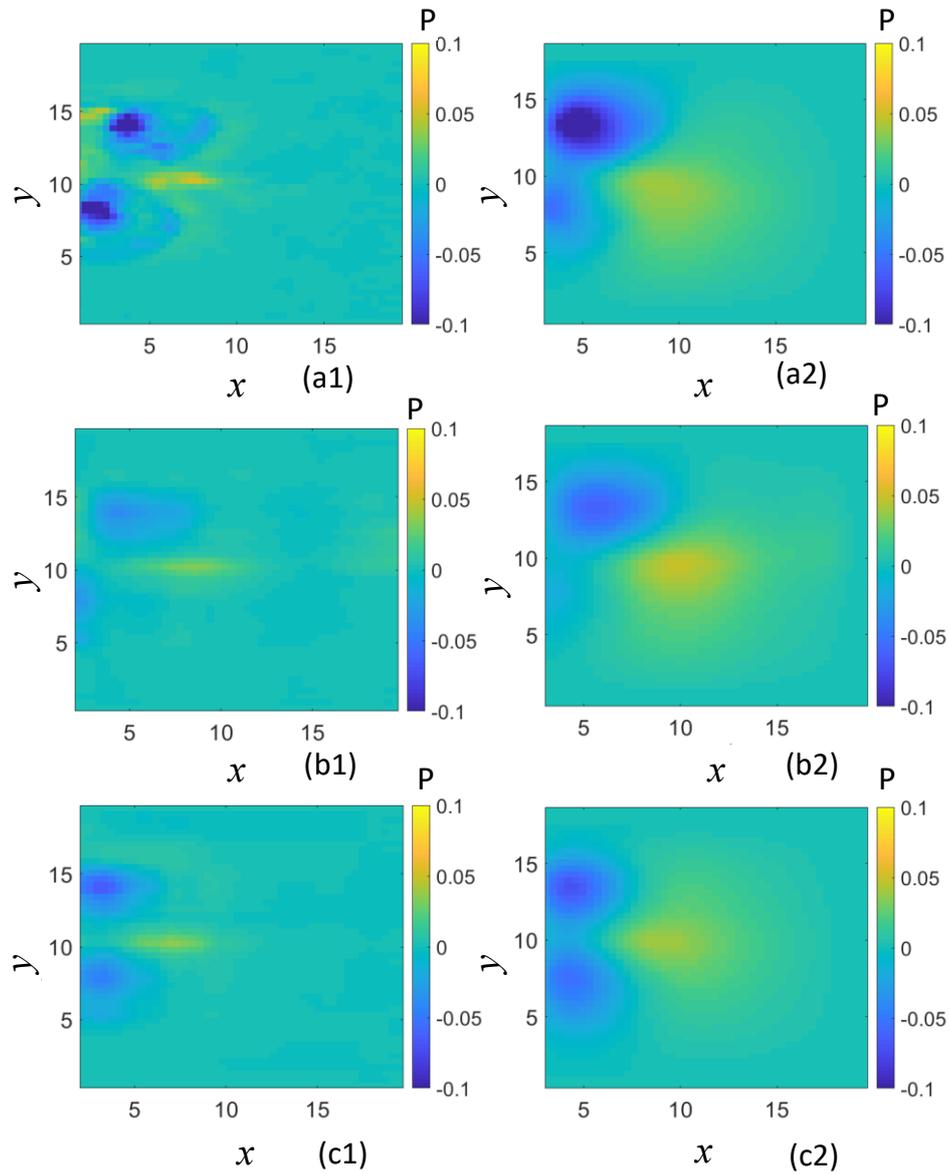
Fig. 6.7. Pressure distribution in cylinder flow, reconstructed pressure (a1) without applying filtering (a2) after applying present correction method (b1) after applying FFT low pass filtering (b2) after applying present method, (c1) after applying POD based filtering (c2) after applying present method

Chapter 7

Conclusions and future directions

7.1 Conclusions

Experimental tool development for pressure profile measurements has current industrial demand. This study offers new techniques of measurement of pressure distribution by fusion of experiments and CFD in incompressible flows. Three algorithms are developed for opaque Newtonian fluids, transparent shear-thinning fluid and opaque shear thinning fluids. By using PIV and UVP, spatio-temporal velocity data were obtained in transparent and opaque fluids respectively. For pressure estimation Navier-Stokes, pressure Poisson and momentum equations were utilized for Newtonian and non-Newtonian fluids.

UVP measurement is limited to one dimensional one component (1D-1C) along measurement line which is not sufficient to estimate pressure field from N-S or Pressure Poisson equation. This requires additional use of equation of continuity. On the other hand, PIV can provide the velocity vector field in two-dimensional two component (2D-2C). So, pressure estimation by PIV data for Newtonian fluids is easier than with UVP. However, PIV cannot be applied to study opaque flows which are more commonly found in food and material industries for which UVP is the possible solution.

Experimental data always suffers from measurement noise which cannot be directly used in CFD equations so filtering is very essential step in fusion methods. For PIV data either median filtering, FFT and POD filtering can be opted but UVP data requires unique combination of FFT and POD filtering before using it in continuity equation.

In chapter 3, a UVP based novel pressure estimation algorithm was developed for opaque fluid. After applying suitable filtering UVP data was used in continuity equation to estimate the second unknown component of velocity. Then to estimate pressure, 2D velocity data was substituted in Navier-Stokes equation. This algorithm was demonstrated for vortex flow in water and milk. In wake region alternating low and high-pressure regions were obtained as per

staggered arrangement of von-Karman vortices. It was found that UVP measurement with Taylor Frozen hypothesis is suitable for accurate pressure estimation in wake of cylinder. Pressure distribution algorithm in non-Newtonian fluids was never reported before so a unique pressure and stress estimation algorithm is developed for steady flow of shear-thinning fluid. This is described in chapter 4. This algorithm couples the PIV, CFD and rheometry. For shear thinning fluid two rheological models: Power law and Carreau Yasuda were used. Viscosity and stress distributions were reported for the first time. For pressure estimation velocity and viscosity data are substituted in momentum equation (with omitted temporal term). Low pressure region at vortex cores were accurately obtained which corroborates the accuracy of algorithm. In addition, the quantitative assessment of relation between material and dynamic property of fluid were performed with cross-correlation analysis. It was found that during development of vortices viscosity is negatively correlated with enstrophy and the pressure lowering intensified at vortex cores with time due to shear thinning property of fluid. Wake stabilization also increases with time. This algorithm is also tested for unsteady instantaneous data. During vortex development the temporal term in momentum equation is 10 times smaller than the advection term due to slow development of flow so the omission of temporal term from momentum equation can be justified. However, when the vortices separated from cylinder and migrated in the wake, due to highly unsteady wake flows, the algorithm fails. One other possible option in unsteady flows at higher Re is pressure Poisson equation. For non-Newtonian fluid flows the source term of pressure Poisson equation is more complex due to spatial gradient of viscosity and cannot be solved with low resolution PIV data. An uncertainty quantification is included to explain how experimental uncertainties in velocity will propagate in calculation of pressure. It was found that the error propagation is directly proportional to error in viscosity. Although the shear thinning property can reduce the error propagation. Another factor is spatial resolution of data, high spatial resolution could reduce the error in diffusion terms but increases the error in convection term.

For unsteady separated vortex flow in shear thinning fluid UVP based pressure and stress estimation algorithm is developed and discussed in chapter 5. The FFT and POD filtering were also found suitable for shear-thinning fluid flows. This algorithm couples UVP, equation of continuity, rheometry and pressure Poisson equation. Due to capability of UVP this algorithm can also be applied in opaque non-Newtonian fluid flows. An alternating staggered arrangement of low-pressure region are obtained in core of vortices in wake of cylinder. This signifies that for pressure estimation in unsteady flow in shear thinning flows, UVP is a suitable substitute of PIV.

Error in velocity field often propagates and produces curl in pressure gradient field. However as per mathematical definition the gradient of a scalar quantity should not have curl. Hence, an irrotational correction (IC) method is developed to filter estimated pressure. The pressure gradient field is decomposed into rotational and irrotational parts using Helmholtz decomposition theorem. Then rotational part should be neglected, and filtered pressure is calculated from irrotational part. This method was tested in PIV data collected at t=12 sec in water flow over cylinder. Four set of pressure data are obtained by solving pressure Poisson equation for unfiltered, FFT and POD filtered velocity data. The present method can entirely eliminate the need of velocity filtering before estimating pressure field. Also, present correction method offers the curl free pressure estimation without performing any integration of pressure gradients if Navier-Stokes equation is employed.

7.2 Future directions

Based on findings of present work several research directions can be envisioned, some of them are listed here.

1. Reconstruction of two-dimensional velocity field in milk flow by UVP pointed out that the vortex shedding frequency becomes lower in milk flow which is very useful

information for vortex flow meters which are generally used in industries for maintaining good quality of product. The frequency of vortex shedding can also be determined for other opaque fluids which has either Newtonian or non-Newtonian nature.

2. The present study demonstrated the pressure profile estimation in shear thinning flows. In future, pressure estimation profiler can be developed for other non-Newtonian fluids such as viscoelastic, shear thickening fluids etc.

3. Pressure drop in pipes bends and complex pipes is still unsolved problem of industries and these are responsible for product quality degradation. Hence, the pressure estimation algorithm can be implemented to study fluid flows in such complex geometries.

4. Pressure estimation in opaque fluid flows by UVP also made possible its application in experimental study of sediment transport during Tsunami propagation.

5. As noted in this thesis the resolution of PIV is insufficient for reconstruction of pressure in unsteady non-Newtonian fluid flows. Artificial intelligence-based resolution improvement could be an effective solution for this purpose.

6. AI with pressure estimation methodology could be a counterpart of direct numerical simulations. Even smallest turbulent structure can be resolved and properly studied which has many practical relevance such as designing airplanes, high speed trains, mixing of different fluids in food industries, vortex induce vibrations in civil and marine engineering, effect of bottom boundary layers during Tsunami run up etc.

References

Adrian RJ (2005) Twenty years of particle image velocimetry. In: Experiments in Fluids. pp 159–169

Adrian RJ (1991) Particle-Imaging Techniques for Experimental Fluid Mechanics. Annu Rev Fluid Mech 23:261–304. https://doi.org/10.1146/annurev.fl.23.010191.001401

Aritomi M, Zhou S, Nakajima M, et al (1996) Measurement System of Bubbly Flow Using Ultrasonic Velocity Profile Monitor and Video Data Processing Unit. J Nucl Sci Technol 33:915–923. https://doi.org/10.1080/18811248.1996.9732033

Azijli I, Dwight RP (2015) Solenoidal filtering of volumetric velocity measurements using Gaussian process regression. Exp Fluids 56:198. https://doi.org/10.1007/s00348-015-2067-7

Azijli I, Sciacchitano A, Ragni D, et al (2016) A posteriori uncertainty quantification of PIV-based pressure data. Exp Fluids 57:1–15. https://doi.org/10.1007/s00348-016-2159-z

Azmi AM, Zhou T (2018) Effect of screen geometry on the vortex formation behind a circular cylinder. J Adv Res Fluid Mech Therm Sci 44:

Bailoor S, Seo J-H, Mittal R (2019) Vortex Shedding from a Circular Cylinder in shear-thinning Carreau Fluids. Phys Fluids 31:11703. https://doi.org/10.1063/1.5086032

Baur T KJ (1999) PIV with high temporal resolution for the determination of local ... In: 3rd Int. Work. Part. Image Velocim. (Santa Barbar. https://www.yumpu.com/en/document/view/3642130/piv-with-high-temporal-resolution-for-the-determination-of-local-. Accessed 21 Apr 2020

Bharti RP, Chhabra RP, Eswaran V (2007) Steady forced convection heat transfer from a heated circular cylinder to power-law fluids. Int J Heat Mass Transf 50:977–990. https://doi.org/10.1016/J.IJHEATMASSTRANSFER.2006.08.008

Bird RB (Robert B, Stewart WE, Lightfoot EN (2007) Transport phenomena. J. Wiley

Cai S, Liang J, Gao Q, et al (2019) Particle Image Velocimetry Based on a Deep Learning

Motion Estimator. IEEE Trans Instrum Meas 1–1. https://doi.org/10.1109/tim.2019.2932649

Carreau PJ (1972) Rheological Equations from Molecular Network Theories. Cit Trans Soc Rheol 16:99. https://doi.org/10.1122/1.549276

Charonko JJ, King C V., Smith BL, Vlachos PP (2010a) Assessment of pressure field calculations from particle image velocimetry measurements. Meas Sci Technol 21:. https://doi.org/10.1088/0957-0233/21/10/105401

Charonko JJ, King C V., Smith BL, Vlachos PP (2010b) Assessment of pressure field calculations from particle image velocimetry measurements. Meas Sci Technol 21:. https://doi.org/10.1088/0957-0233/21/10/105401

Chopra G, Mittal S (2019) Drag coefficient and formation length at the onset of vortex shedding. Phys Fluids 31:013601. https://doi.org/10.1063/1.5075610

Christensen KT, Adrian RJ (2002) Measurement of instantaneous Eulerian acceleration fields by particle image accelerometry: Method and accuracy. Exp Fluids 33:759–769. https://doi.org/10.1007/s00348-002-0488-6

Coelho P., Pinho F. (2004) Vortex shedding in cylinder flow of shear-thinning fluids. III: Pressure measurements. J Nonnewton Fluid Mech 121:55–68. https://doi.org/10.1016/J.JNNFM.2004.04.004

Cottet G-H, Poncet P (2002) Particle methods for direct numerical simulations of three-dimensional wakes. J Turbul 3:N38. https://doi.org/10.1088/1468-5248/3/1/038

Cross MM (1968) Rheology of viscoelastic fluids: elasticity determination from tangential stress measurement. J Colloid Interface Sci 27:84–90. https://doi.org/10.1016/0021-9797(68)90012-X

Dabiri D (2009) Digital particle image thermometry/velocimetry: A review. Exp. Fluids 46:191–241

De Kat R, Ganapathisubramani B (2013) Pressure from particle image velocimetry for

convective flows: A Taylor's hypothesis approach. Meas Sci Technol 24:. https://doi.org/10.1088/0957-0233/24/2/024002

De Kat R, Van Oudheusden BW (2012) Instantaneous planar pressure determination from PIV in turbulent flow. Exp Fluids 52:1089–1106. https://doi.org/10.1007/s00348-011-1237-5

De Silva CM, Philip J, Marusic I (2013) Minimization of divergence error in volumetric velocity measurements and implications for turbulence statistics. Exp Fluids 54:. https://doi.org/10.1007/s00348-013-1557-8

Dhiman AK, Chhabra RP, Eswaran V (2006) Steady flow of power-law fluids across a square cylinder. Chem Eng Res Des 84:300–310. https://doi.org/10.1205/cherd05017

Elsinga GE, Scarano F, Wieneke B, van Oudheusden BW (2006) Tomographic particle image velocimetry. Exp Fluids 41:933–947. https://doi.org/10.1007/s00348-006-0212-z

Fey U, König M, Eckelmann H (1998) A new Strouhal-Reynolds-number relationship for the circular cylinder in the range 47<Re<2×105. Phys Fluids 10:1547–1549. https://doi.org/10.1063/1.869675

Ghaemi S, Ragni D, Scarano F (2012) PIV-based pressure fluctuations in the turbulent boundary layer. Exp Fluids 53:1823–1840. https://doi.org/10.1007/s00348-012-1391-4

Grant I (1997) Particle image velocimetry: A review. Proc Inst Mech Eng Part C J Mech Eng Sci 211:55–76. https://doi.org/10.1243/0954406971521665

Gresho PM, Sani RL (1987) On pressure boundary conditions for the incompressible Navier-Stokes equations. Int J Numer Methods Fluids 7:1111–1145. https://doi.org/10.1002/fld.1650071008

Gui LC, Merzkirch W (1996) Method of tracking ensembles of particle images. Exp Fluids 21:465–468. https://doi.org/10.1007/BF00189049

Gurka R, Liberzon' A, Hefet D, et al (1999) Computation of Pressure Distribution Using PIV Velocity Data

Ihara T, Kikura H, Takeda Y (2013) Ultrasonic velocity profiler for very low velocity field.

Flow Meas Instrum 34:127–133. https://doi.org/10.1016/j.flowmeasinst.2013.10.003

Imaichi K, Ohmi K (1983) Numerical processing of flow-visualization pictures — measurement of two-dimensional vortex flow. J Fluid Mech 129:283–311. https://doi.org/10.1017/S0022112083000774

Jakobsen ML, Dewhirst TP, Greated CA (1997) Particle image velocimetry for predictions of acceleration fields and force within fluid flows. Meas Sci Technol 8:1502. https://doi.org/10.1088/0957-0233/8/12/013

Jensen A, Pedersen GK, Wood DJ (2003) An experimental study of wave run-up at a steep beach. J Fluid Mech 486:161–188. https://doi.org/10.1017/S0022112003004543

Jensen JA, Nikolov S, Yu ACH, Garcia D (2016) Ultrasound Vector Flow Imaging: I: Sequential Systems. IEEE Trans Ultrason Ferroelectr Freq Control 1–1. https://doi.org/10.1109/TUFFC.2016.2600763

Jeon YJ, Gomit G, Earl T, et al (2018) Sequential least-square reconstruction of instantaneous pressure field around a body from TR-PIV. Exp Fluids 59:. https://doi.org/10.1007/s00348-018-2489-0

Lin C, Hsieh S-C (2003) Convection Velocity of Vortex Structures in the Near Wake of a Circular Cylinder. J Eng Mech 129:1108–1118. https://doi.org/10.1061/(ASCE)0733-9399(2003)129:10(1108)

Liu X, Katz J (2006) Instantaneous pressure and material acceleration measurements using a four-exposure PIV system. In: Experiments in Fluids. pp 227–240

Lynch KP, Scarano F (2014) Material acceleration estimation by four-pulse tomo-PIV. Meas Sci Technol 25:. https://doi.org/10.1088/0957-0233/25/8/084005

McClure J, Yarusevych S (2017a) Instantaneous PIV/PTV-based pressure gradient estimation: a framework for error analysis and correction. Exp Fluids 58:. https://doi.org/10.1007/s00348-017-2369-z

McClure J, Yarusevych S (2017b) Optimization of planar PIV-based pressure estimates in

laminar and turbulent wakes. Exp Fluids 58:62. https://doi.org/10.1007/s00348-017-2337-7

Meyer KE, Pedersen JM, ̈Ozcan O (2007) A turbulent jet in crossflow analysed with proper orthogonal decomposition. J Fluid Mech 583:199–227. https://doi.org/10.1017/S0022112007006143

Mirzaei Nejad M, Javaherdeh K (2014) Numerical simulation of power-law fluids flow and heat transfer in a parallel-plate channel with transverse rectangular cavities. Case Stud Therm Eng 3:68–78. https://doi.org/10.1016/J.CSITE.2014.03.004

Murai Y, Nakada T, Suzuki T, Yamamoto F (2007) Particle tracking velocimetry applied to estimate the pressure field around a Savonius turbine. Meas Sci Technol 18:2491–2503. https://doi.org/10.1088/0957-0233/18/8/026

Norberg C (1987) Effects of Reynolds number and a low-intensity freestream turbulence on the flow around a circular cylinder. Chalmers Univ Goteborg, Sweden, 1–54

Obayashi H, Tasaka Y, Kon S, Takeda Y (2008) Velocity vector profile measurement using multiple ultrasonic transducers. Flow Meas Instrum 19:189–195. https://doi.org/10.1016/J.FLOWMEASINST.2007.11.007

Oldroyd J.G. (1950) On the formulation of rheological equations of state. Proc R Soc London Ser A Math Phys Sci 200:523–541. https://doi.org/10.1098/rspa.1950.0035

Pan Z, Whitehead J, Thomson S, Truscott T (2016) Error propagation dynamics of PIV-based pressure field calculations: How well does the pressure Poisson solver perform inherently? Meas Sci Technol 27:. https://doi.org/10.1088/0957-0233/27/8/084012

Prasad AK (2000) Stereoscopic particle image velocimetry Review Paper. Springer-Verlag

Pust (2006) PIV: Direct Cross-Correlation compared with FFT-based Cross-Correlation

Rabault J, Kolaas J, Jensen A (2017) Performing particle image velocimetry using artificial neural networks: a proof-of-concept. Meas Sci Technol 28:125301. https://doi.org/10.1088/1361-6501/AA8B87

Rabby MG, Razzak A, Molla MM (2013) Pulsatile Non-Newtonian Blood Flow through a Model of Arterial Stenosis. Procedia Eng 56:225–231. https://doi.org/10.1016/J.PROENG.2013.03.111

Rao MA (2014) Flow and Functional Models for Rheological Properties of Fluid Foods. pp 27–61

Scarano F, Riethmuller ML (1999) Iterative multigrid approach in PIV image processing with discrete window offset. Exp Fluids 26:513–523. https://doi.org/10.1007/s003480050318

Schneiders JFG, Pröbsting S, Dwight RP, et al (2016) Pressure estimation from single-snapshot tomographic PIV in a turbulent boundary layer. Exp Fluids 57:53. https://doi.org/10.1007/s00348-016-2133-9

Schneiders JFG, Scarano F (2016) Dense velocity reconstruction from tomographic PTV with material derivatives. Exp Fluids 57:1–22. https://doi.org/10.1007/s00348-016-2225-6

Schwabe M (1935) Über Druckermittlung in der nichtstationären ebenen Strömung. Ingenieur-Archiv 6:34–50. https://doi.org/10.1007/BF02086409

Sciacchitano A, Dwight RP, Scarano F (2012) Navier-Stokes simulations in gappy PIV data. Exp Fluids. https://doi.org/10.1007/s00348-012-1366-5

Sciacchitano A, Wieneke B (2016) PIV uncertainty propagation. Meas Sci Technol 27:. https://doi.org/10.1088/0957-0233/27/8/084006

Sirovich L (1987a) Turbulence and the dynamics of coherent structures part I: Coherent structures

Sirovich L (1987b) Turbulence and the dynamics of coherent structures PART III: DYNAMICS AND SCALING*

Song SM, Napel S, Glover GH, Pelc NJ (1993) Noise reduction in three-dimensional phase-contrast MR velocity measurements. J Magn Reson Imaging 3:587–96. https://doi.org/10.1002/jmri.1880030407

Suzuki T, Ji H, Yamamoto F (2009) Unsteady PTV velocity field past an airfoil solved with

DNS: Part 1. Algorithm of hybrid simulation and hybrid velocity field at Re ≈ 10 3. Exp Fluids 47:957–976. https://doi.org/10.1007/s00348-009-0691-9

Suzuki T, Yamamoto F (2015) Hierarchy of hybrid unsteady-flow simulations integrating time-resolved PTV with DNS and their data-assimilation capabilities. Fluid Dyn Res 47:. https://doi.org/10.1088/0169-5983/47/5/051407

Takeda Y (1995) Velocity profile measurement by ultrasonic doppler method. Exp Therm Fluid Sci 10:444–453. https://doi.org/10.1016/0894-1777(94)00124-Q

Takeda Y (2012) Ultrasonic Doppler Velocity Profiler for Fluid Flow. Springer Japan, Tokyo

Tamano S, Itoh M, Ide Y, Yokota K (2007) Vortex Shedding in Confined Swirling Flow of Polymer Solutions. Trans Japan Soc Mech Eng Ser B 73:482–489. https://doi.org/10.1299/kikaib.73.482

Tamano S, Itoh M, Kato K, Yokota K (2010) Turbulent drag reduction in nonionic surfactant solutions. Phys Fluids 22:055102. https://doi.org/10.1063/1.3407666

Tang HS, Kalyon DM (2004) Estimation of the parameters of Herschel-Bulkley fluid under wall slip using a combination of capillary and squeeze flow viscometers. Rheol Acta 43:80–88. https://doi.org/10.1007/s00397-003-0322-y

Tang S, Aubry N (1997) On the symmetry breaking instability leading to vortex shedding. Phys Fluids 9:2550–2561. https://doi.org/10.1063/1.869372

Tasaka Y, Birkhofer B, Furuichi N, et al (2012) Practical Applications. pp 107–200

Tasaka Y, Kimura T, Murai Y (2015) Estimating the effective viscosity of bubble suspensions in oscillatory shear flows by means of ultrasonic spinning rheometry. Exp Fluids 56:1867. https://doi.org/10.1007/s00348-014-1867-5

Thielicke W, Stamhuis EJ (2014) PIVlab – Towards User-friendly, Affordable and Accurate Digital Particle Image Velocimetry in MATLAB. J Open Res Softw 2:. https://doi.org/10.5334/jors.bl

Thomas M, Misra S, Kambhamettu C, Kirby JT (2005) A robust motion estimation algorithm

for PIV. Meas Sci Technol 16:865. https://doi.org/10.1088/0957-0233/16/3/031

Tiwari N, Tasaka Y, Murai Y (2019) Pressure field estimation from ultrasound Doppler velocity profiler for vortex-shedding flows. Flow Meas Instrum 67:23–32. https://doi.org/10.1016/J.FLOWMEASINST.2019.03.009

Trias M, Arbona A, Massó J, et al (2014) FDA's nozzle numerical simulation challenge: Non-Newtonian fluid effects and blood damage. PLoS One 9:e92638. https://doi.org/10.1371/journal.pone.0092638

Ueki Y (2016) UVP Measurement of Lead-Lithium Flow and Nuclear Fusion Engineering Research. J Vis Soc Japan 36:16–20. https://doi.org/10.3154/jvs.36.142_16

Van der Kindere JW, Laskari A, Ganapathisubramani B, de Kat R (2019) Pressure from 2D snapshot PIV. Exp Fluids 60:32. https://doi.org/10.1007/s00348-019-2678-5

van Gent PL, Michaelis D, van Oudheusden BW, et al (2017) Comparative assessment of pressure field reconstructions from particle image velocimetry measurements and Lagrangian particle tracking. Exp Fluids 58:1–23. https://doi.org/10.1007/s00348-017-2324-z

van Oudheusden BW (2013) PIV-based pressure measurement. Meas Sci Technol 24:032001. https://doi.org/10.1088/0957-0233/24/3/032001

Van Oudheusden BW, Scarano F, Roosenboom EWM, et al (2007) Evaluation of integral forces and pressure fields from planar velocimetry data for incompressible and compressible flows. Exp Fluids 43:153–162. https://doi.org/10.1007/s00348-007-0261-y

Violato D, Moore P, Scarano F (2011) Lagrangian and Eulerian pressure field evaluation of rod-airfoil flow from time-resolved tomographic PIV. In: Experiments in Fluids. pp 1057–1070

Walters K, Webster MF (2003) The distinctive CFD challenges of computational rheology. Int J Numer Methods Fluids 43:577–596. https://doi.org/10.1002/fld.522

Wang Z, Gao Q, Wang C, et al (2016) An irrotation correction on pressure gradient and

orthogonal-path integration for PIV-based pressure reconstruction. Exp Fluids 57:104. https://doi.org/10.1007/s00348-016-2189-6

Wiklund J, Jeelani SAK, Stading MT, Windhab EJ (2012) In-Line Rheometry of Particulate Suspensions by Pulsed Ultra-sound Velocimetry Combined with Pressure Difference Method. Appl Rheol 22:. https://doi.org/10.3933/ApplRheol-22-42232

Wiklund J, Stading M (2008) Application of in-line ultrasound Doppler-based UVP–PD rheometry method to concentrated model and industrial suspensions. Flow Meas Instrum 19:171–179. https://doi.org/10.1016/J.FLOWMEASINST.2007.11.002

Willert CE, Gharib M (1991) Digital particle image velocimetry. Exp Fluids 10:181–193. https://doi.org/10.1007/BF00190388

Williamson CHK (1996) Vortex Dynamics in the Cylinder Wake. Annu Rev Fluid Mech 28:477–539. https://doi.org/10.1146/annurev.fl.28.010196.002401

Yokoyama K, Kojima S, Ohkubo T, et al (2006) Environmental Flow Measurement Using Ultrasonic Velocity Profiler. Trans Japan Soc Mech Eng Ser B 72:1694–1701. https://doi.org/10.1299/kikaib.72.1694

Yoo S-S, Suh S-H, Roh H-W (1996) Numerical simulation of flows of non-Newtonian fluids in the stenotic and bifurcated tubes. KSME J 10:223–234. https://doi.org/10.1007/bf02953661

Yoshida T, Tasaka Y, Murai Y (2019) Efficacy assessments in ultrasonic spinning rheometry: Linear viscoelastic analysis on non-Newtonian fluids. J Rheol (N Y N Y) 63:503–517. https://doi.org/10.1122/1.5086986

Zhu H, Gao Y (2017) Vortex-induced vibration suppression of a main circular cylinder with two rotating control rods in its near wake: Effect of the rotation direction. J Fluids Struct 74:469–491. https://doi.org/10.1016/J.JFLUIDSTRUCTS.2017.07.004